

# Experimental Investigation of Blade Group Vibrations in an Axial Turbine Cascade

THÈSE N° 6194 (2014)

PRÉSENTÉE LE 4 JUILLET 2014

À LA FACULTÉ DES SCIENCES ET TECHNIQUES DE L'INGÉNIEUR  
LABORATOIRE DE THERMIQUE APPLIQUÉE ET DE TURBOMACHINES  
PROGRAMME DOCTORAL EN ENERGIE

ÉCOLE POLYTECHNIQUE FÉDÉRALE DE LAUSANNE

POUR L'OBTENTION DU GRADE DE DOCTEUR ÈS SCIENCES

PAR

**Achim ZANKER**

acceptée sur proposition du jury:

Dr S.-R. Cherkaoui, président du jury  
Dr P. Ott, directeur de thèse  
Prof. T. Arts, rapporteur  
Dr H. J. Belz, rapporteur  
Prof. D. Favrat, rapporteur



ÉCOLE POLYTECHNIQUE  
FÉDÉRALE DE LAUSANNE

Suisse  
2014



There is nothing like looking, if you want to find something.  
You certainly usually find something, if you look,  
but it is not always quite the something you were after.  
— J. R. R. Tolkien



# Acknowledgements

First of all I would like to dedicate a few lines to the persons who crossed my path through the daily jungle leading to the completion of this PhD work.

I hereby would like to thank Dr. Peter Ott for giving me the opportunity and the support to perform this thesis work at the “Groupe de Turbomachines Thermiques”, formerly known as “Laboratoire de Thermique Appliquée et de Turbomachines” (LTT) at the Ecole Polytechnique Fédérale de Lausanne.

I am grateful to the members of my thesis jury Prof. Dr. Tony Arts and Prof. Dr. Daniel Favrat for their help. I especially appreciated the support and encouragements from Dr. Joachim “Jochen” Belz who accompanied me through the years spent on the FUTURE project. His advice and guidance were always of great value to me. Thank you also to Dr. Rachid Cherkaoui who gently accepted the challenge of being the jury president.

A great thanks to all my colleges I had at LTT. I’m thankful to had you guys at my side. I would like to address special thanks to Dr. Philip Peschke who helped me during troubling times and also for the dozens of stress releasing hiking trips. Many thanks to Dr. Virginie Chenaux for her uncomplicated collaboration and support. I would like to thank Sami Goekce for the good times and the patience teaching me French. Big thanks to Dr. Magnus Jonsson and Dr. Elia Colombo for their technical advice to get started.

In order to accomplish such an ambitious objective as this PhD thesis, a lot of administrative stuff had to be done. Of great help in this matter were the secretaries of the LTT, Annick Despont, Margarita Jotterand-Jimenez and Stina Zufferey and from the doctoral school, Cécile Taverney, to whose I would like to address my sincere gratitude.

Of course, to perform some experimental work professional mechanics are needed. And this is why I would like to thank Christophe Zurmühle, Nicolas Jaunin and Marc Salle for their support and immediate help when I needed it.

As my PhD thesis was part of the European research project “FUTURE”, I would like to thank all the international members involved. It was a great pleasure to discuss and see things through with you. These gave me motivation and a good feeling about my work.

---

Last but not least I would like to sincerely thank Barbara Althaus, Martin Schwitzke, Julia Beyer and Jonathan Habermacher for their patience to read the following lines chapter by chapter and their valuable comments for a better understanding of them.

Work was one part of the daily jungle and spare-time the other. This is to all my friends, old as well as new ones, thank you very much for the incredible fun time we had together. The lake and balcony BBQs were memorable. At this point I would like to especially thank my dear Anne for her incredible patience and her highly motivating words during the last months of completing this work.

Zu guter Letzt möchte ich meinen herzlichsten Dank an meine liebe Eltern aussprechen. Ohne Eure ununterbrochene Unterstützung, in all meinen Lebenssituationen in den vergangenen Jahren und noch weit davor, wäre diese Doktorarbeit niemals möglich gewesen. Daher möchte ich diese Arbeit besonders euch Beiden widmen, denn Ihr habt einen erheblichen Teil zum Gelingen der ganzen Sache beigetragen.

The experimental data used in this thesis was acquired in the research program FUTURE (Flutter-Free Turbomachinery Blades, [www.future-project.eu](http://www.future-project.eu)), co-funded by the European Union's Seventh Framework Programme for research, technological development and demonstration under grant agreement no 213414. The permission to publish is gratefully acknowledged.

# Abstract

An efficient way to increase the aeroelastic stability of a blade-row of low-pressure turbines is to connect the individual blades to clusters of two or more. As the clustered blade-row oscillates during operation, complex vibration mode-shapes occur, whose influences on the aerodynamic stability of the cluster still need detailed investigations and analysis in order to be fully understood.

This work aims to improve the understanding of cluster configurations in low-pressure turbines influencing the aerodynamic stability of the blade-row, and focuses on:

- The experimental validation of a specific procedure which predicts the aerodynamic parameters of the individual cluster-blades by using measured aerodynamic single-blade data as input. The procedure is based on the relationship between the traveling-wave and the influence coefficient formulation. Single-blade data in the traveling-wave formulation is used as input for the procedure, which is transformed to influence coefficients prior to the application of the method. The procedure then applied those single-blade influence coefficients and included the cluster kinematics when converting them to the traveling-wave formulation. Thus, the resulting aerodynamic parameters in the traveling-wave formulation represent those of the cluster-blade.
- The experimental investigation of how different cluster-configurations (grouped blades) affect the aerodynamic stability compared to the corresponding single-blades (non-grouped blades).

Measurements have been performed in the non-rotating annular test facility of the Group of Thermal Turbomachinery (GTT) at the École Polytechnique Fédérale de Lausanne (EPFL). A turbine cascade composed of 20 blades has been used for the aeroelastic measurements. The blade excitation mechanism allowing controlled vibrations of each blade vibration system, enabled the simulation of cluster configurations for traveling-wave mode measurements.

This study presents the measurement results of the aerodynamic response of a cascade oscillating in different cluster configurations. The first cluster investigated was composed of two blades simulating a welded-in-pair blade connection. This cluster was oscillated in a mode-shape at which both cluster-blades were moving in-phase. Successively, three oscillation

## Abstract

---

directions were investigated: torsion, axial- and flap-bending. The second cluster configuration was a four-blade cluster simulating a torsional mode-shape of a cast blade-package. For comparison, single-blade cases were measured with blade vibration conditions corresponding to the cluster cases. All test cases were performed under almost identical subsonic flow conditions.

The measurement results revealed that the aforementioned procedure is valid. This could be confirmed by comparing the predicted results of the procedure with the measured results of the chord-wise aerodynamic work and the global aerodynamic damping.

The comparisons showed a good agreement for all cluster configurations within the limits of the experimental measurement accuracy. Small differences between the measured and predicted results were observed and attributed to small variations in the flow field during the different measurement campaigns.

For some cluster configurations, the analysis of the experimental results showed that connecting blades into clusters minimizes the aerodynamic work within the inner-cluster channels and thus, causes an increase of the minimum aerodynamic damping of the cluster-blade compared to the corresponding single-blade case (two-blade cluster with a torsion oscillation and the four-blade cluster). For the two-blade cluster with bending oscillation the trend was observed but could not be definitely validated with the used flow-conditions. Changing the reference case flow-conditions might yield further conclusions on these cluster cases.

**Keywords:** aeroelasticity, annular turbine cascade, experimental cluster measurements, single-blade, grouped-blades, cluster-blade, aerodynamic stability, traveling-wave mode, influence coefficients, superposition principle, unsteady pressure, time-resolved measurements, aerodynamic damping



# Résumé

Une solution efficace pour accroître la stabilité aéroélastique des aubes dans une grille de turbine basse-pression consiste à assembler les aubes individuelles en groupe d'aubes (cluster). Lors d'éventuelles vibrations, les groupes d'aubes oscillent selon des modes de vibration plus complexes qui peuvent à leur tour influencer la stabilité aérodynamique de l'aube. Cette approche nécessite cependant davantage d'investigations et d'analyses pour permettre d'améliorer la compréhension du phénomène.

En ce but, ce travail vise à étudier le comportement de différentes configurations de cluster en vibration, et leur influence sur la stabilité aérodynamique de l'aube considérée individuellement. L'analyse porte sur deux aspects majeurs :

- La validation par expérimentation d'une procédure spécifique, qui prédit les paramètres aérodynamiques de l'aube individuelle au sein du cluster, en utilisant les paramètres mesurés pour une aube seule (hors cluster, en mode single-blade). La procédure appliquée pour prédire les paramètres de stabilité aérodynamique d'une aube dans un cluster est basée sur la relation entre la formulation en onde progressive et la formulation des coefficients d'influence. Comme données de départ, les mesures effectuées dans la formulation en onde progressive, et pour le cas d'une aube individuelle, ont été converties dans la formulation de coefficients d'influence. Lors de l'intégration de ces coefficients dans la formulation d'onde progressive, les schémas cinématiques du cluster sont ensuite pris en compte. Ceci garantit que les paramètres aérodynamiques représentent effectivement les aubes individuelles considérées dans le groupe d'aubes.
- L'analyse expérimentale de différentes configurations de cluster, et de leur effet sur la stabilité aérodynamique, en comparaison à une configuration correspondant à une aube individuelle.

Les mesures ont été réalisées dans le stand annulaire du Groupe de Turbomachines Thermiques (GTT) à l'Ecole Polytechnique Fédérale de Lausanne (EPFL). Une grille de turbine composée de 20 aubes a été utilisée pour les mesures aéroélastiques. Grâce à un système d'excitation indépendant pour chaque aube, l'oscillation des aubes a pu être contrôlée séparément, permettant ainsi de mesurer des configurations de cluster différents, pour des mesures en mode d'ondes progressives (traveling-wave mode).

## Résumé

---

Cette étude présente les résultats des mesures de la réponse aérodynamique de la grille d'aubes oscillante, pour plusieurs configurations de cluster. Le premier groupe analysé se compose de deux aubes simulant un couplage par soudure. Ce groupe oscille dans un mode propre pour lequel les deux aubes sont en phase. Trois directions d'oscillations ont été étudiées successivement : torsion, flexion axiale, et flexion en plie (flap-bending). La seconde configuration est un groupe de quatre aubes simulant un mode de torsion pour des aubes coulées.

En guise de comparaison, des configurations avec aube individuelle ont été mesurées pour des conditions de vibration identiques. Tous les cas analysés ont été réalisés dans les mêmes conditions d'écoulement subsoniques.

Les résultats ainsi obtenus permettent de valider la méthode. Les prédictions et l'analyse des mesures permettent de déterminer puis de comparer le travail aérodynamique le long de la corde de l'aube et l'amortissement aérodynamique global. Des différences minimales entre les mesures et les prédictions ont été identifiées : elles sont attribuées aux faibles variations de l'écoulement durant les différentes campagnes de mesures. D'une façon générale, les comparaisons entre les deux approches sont en conformité pour toutes les configurations de cluster dans la limite de la précision des mesures.

L'analyse des données montre qu'un assemblage d'aubes judicieux peut s'avérer avantageux : il minimise le travail aérodynamique dans les canaux intérieurs au cluster et augmente l'amortissement aérodynamique minimum comparé au cas de la même aube considérée de manière individuelle. Cet effet a clairement été identifié pour le cluster de deux aubes et pour le cluster de quatre aubes en mode de torsion. Concernant le cluster de deux aubes en mode de flexion, une tendance similaire a été observée, mais due aux conditions d'écoulement, elle n'a pas pu être validée définitivement expérimentalement. En changeant les conditions du cas de référence il serait alors possible de tirer davantage de conclusions pour ce type de cluster.

**Mots-clés :** aéroélasticité, étude expérimentale de cluster, grille annulaire de turbine, groupe d'aubes, cluster, single-blade, stabilité aérodynamique, onde progressive, coefficients d'influence, principe de superposition, pression instationnaire, mesure instationnaire, amortissement aérodynamique

# Zusammenfassung

Eine effiziente Methode die aeroelastische Stabilität von Einzelschaufeln in einer Niederdruckturbinen-Schaufelreihe zu erhöhen, besteht darin sie zu Gruppen von zwei oder mehr Schaufeln zusammen zu schliessen. Die oszillierenden Schaufelgruppierungen (cluster) erzeugen komplexe Schwingungsformen, die wiederum die aerodynamische Stabilität der Schaufelgruppierungen beeinflussen. Dieses Phänomen ist heute noch nicht vollständig verstanden und bedarf detaillierter Untersuchungen.

Diese Arbeit hat zum Ziel das Verständnis von Schaufelgruppierungen in Niederdruckturbinen bezüglich ihrer aerodynamische Stabilität zu erweitern. Der Fokus liegt dabei auf zwei wesentlichen Punkten:

- Die experimentelle Validierung einer Methode, welche die aerodynamischen Stabilitätsparameter der einzelnen Schaufeln in einer Schaufelgruppierung ermittelt, in dem sie gemessene aerodynamische Werte von Einzelschaufeln als Vorgabe verwendet. Die Methode basiert auf der Beziehung zwischen den Formulierungen der umlaufenden Welle (traveling-wave) und den Einflusskoeffizienten (influence coefficient). Die Werte der Einzelschaufeln sind zu Beginn in der Formulierung als umlaufende Welle gegeben. Vor ihrer Verwendung werden diese in Einflusskoeffizienten umgewandelt. Nun werden diese Werte wieder von Einflusskoeffizienten zu Werten in der Formulierung der umlaufenden Welle umgerechnet, dies aber unter der Berücksichtigung der spezifischen kinematischen Bedingungen der Schaufelgruppierungen. Dadurch beschreibt das Endergebnis letztendlich die aerodynamischen Stabilitätsparameter für die Schaufeln der Schaufelgruppierung.
- Die experimentelle Untersuchung von unterschiedlichen Konfigurationen von Schaufelgruppierungen und deren Einfluss auf die aerodynamische Stabilität in Bezug auf die entsprechende Einzelschaufel.

Die aeroelastischen Messungen wurden an dem nicht rotierenden Ringgitterprüfstand der Group of Thermal Turbomachinery (GTT) an der École Polytechnique Fédérale de Lausanne (EPFL) durchgeführt. Hierzu wurde ein Turbinengitter mit 20 Turbinenschaufeln verwendet. Die Simulation der oszillierenden Schaufelgruppierungen als umlaufende Wellen wurde durch ein spezielles Schaufelanregesystem erreicht, welches jede Schaufel individuell zu einer geregelten Oszillation anregen kann.

Diese Studie präsentiert die aerodynamischen Messergebnisse eines Ringgitters, welches mit unterschiedlichen Konfigurationen von Schaufelgruppierungen schwingt. Die erste untersuchte Schaufelgruppierung besteht aus zwei Schaufeln und simuliert eine als Paar verschweisste Schaufelkonfiguration. Diese Schaufelgruppierung oszilliert so, dass beide Schaufeln sich immer in Phase bewegen. Es wurden erfolgreich drei Schwingungsrichtungen untersucht: Rotation, Axial- und Schlagbiegung. Die zweite Schaufelgruppierung bestand aus vier Schaufeln, welche eine Rotation eines gegossenen Schaufelsatz simulierten. Um einen Vergleich zu ermöglichen wurden Einzelschaufelmessungen durchgeführt, welche die gleichen Schwingungsrichtungen hatten wie die Schaufelgruppierungsfälle. Alle Versuche wurden unter nahezu identischen Strömungsbedingungen im Unterschall durchgeführt.

Die Messresultate beweisen die Gültigkeit der zuvor beschriebenen Methode. Dies konnte nachgewiesen werden, indem die gemessenen Ergebnisse mit den berechneten Ergebnissen der Methode verglichen wurden. In dem Vergleich wurden zum einen der aerodynamische Arbeitsaustausch entlang der Schaufelsehne, zum anderen auch die globale aerodynamische Dämpfung verwendet.

Der Vergleich zeigte eine gute Übereinstimmung der Resultate innerhalb der experimentellen Messgenauigkeitsgrenzen für alle eingestellten Schaufelgruppierungsvarianten und alle möglichen umlaufenden Wellen. Minimale Unterschiede waren erkennbar zwischen Mess- und Rechenergebnissen, und wurden auf kleine Strömungsvariationen zwischen den unterschiedlichen Testkampagnen zurückgeführt.

Für einige Schaufelgruppierungsvarianten haben die experimentellen Ergebnisse gezeigt, dass ein Verbinden von Schaufeln zu Schaufelgruppen die aerodynamische Arbeit in den inneren Schaufelgruppenkanälen minimiert, und somit eine Erhöhung der minimalen aerodynamischen Dämpfung im Vergleich zu Einzelschaufeln zur Folge hat (Zweier-Schaukelgruppierung mit Rotationsbewegung und Vierer-Schaukelgruppierung). Für die Zweier-Schaukelgruppierung mit Biegebewegung war ein ähnlicher Trend erkennbar, der jedoch mit den untersuchten Strömungsbedingungen nicht generell nachgewiesen werden konnte. Eine Änderung der Strömungsbedingungen könnte zu weiteren Schlussfolgerungen für diese Schaufelgruppierungen führen.

**Stichwörter:** Aeroelastizität, Turbinenringgitter, experimentelle Schaufelgruppenmessungen, Einzelschaukel, gruppierte Schaufeln, Schaufel einer Schaufelgruppe, aerodynamische Stabilität, umlaufende Welle, Einflusskoeffizienten, Superpositionsprinzip, instationärer Druck, zeit-aufgelöst Messungen, aerodynamische Dämpfung

# Contents

<b>Acknowledgements</b>	<b>v</b>
<b>Abstract</b>	<b>vii</b>
<b>Résumé</b>	<b>ix</b>
<b>Zusammenfassung</b>	<b>xi</b>
<b>Table of Contents</b>	<b>xv</b>
<b>List of Figures</b>	<b>xx</b>
<b>List of Tables</b>	<b>xxi</b>
<b>Nomenclature</b>	<b>xxiii</b>
<b>1 Introduction</b>	<b>1</b>
1.1 Introduction of Aeroelasticity in Turbomachines . . . . .	1
1.2 Vibration of Single-Blades and Clustered Blades . . . . .	2
1.3 State of the Art . . . . .	7
1.4 Objective of the Present Work . . . . .	10
1.5 Scope of the Work . . . . .	11
<b>2 Theoretical Concept</b>	<b>13</b>
2.1 Analysis of Aerodynamic Stability in Turbomachines . . . . .	14
2.2 Traveling-Wave Formulation . . . . .	15
2.3 Aerodynamic Influence Coefficient Formulation . . . . .	17
2.4 Special Cluster Approach of the Aerodynamic Influence Coefficient Formulation . . . . .	23
2.5 Aerodynamic Stability . . . . .	26
<b>3 Experimental Setup</b>	<b>31</b>
3.1 Non-Rotating Annular Test Facility . . . . .	32
3.2 Annular Turbine Cascade . . . . .	35
3.3 Cascade Vibration Control System . . . . .	37
3.4 Overview of Cascade Instrumentation . . . . .	38

## Contents

---

<b>4</b>	<b>Experimental Test Cases</b>	<b>41</b>
4.1	Sign Convention of the Blade Vibration Direction . . . . .	43
4.2	Two-Blade Cluster . . . . .	43
4.3	Four-Blade Cluster Simulating Torsion . . . . .	46
4.4	Single-Blade . . . . .	49
<b>5</b>	<b>Measurement Techniques</b>	<b>51</b>
5.1	Steady-State Measurements . . . . .	52
5.1.1	Up- and Downstream Flow Quantities . . . . .	52
5.1.2	Blade Surface Pressures . . . . .	54
5.1.3	Casing Surface Pressures . . . . .	54
5.2	Time-Resolved Measurements . . . . .	55
5.2.1	Blade Surface Pressures . . . . .	55
5.2.2	Blade Vibration Measurements . . . . .	55
5.2.3	Cluster Specific Procedures . . . . .	56
5.3	Data Acquisition Systems . . . . .	58
5.3.1	Steady-State Measurements . . . . .	58
5.3.2	Unsteady Measurements . . . . .	59
5.4	Unsteady Data-Reduction Technique . . . . .	60
5.4.1	General Procedure . . . . .	61
5.4.2	Cluster Specific Procedures . . . . .	64
5.4.3	Exemplary FFT Spectra of Raw Signals . . . . .	65
<b>6</b>	<b>Steady-State Flow</b>	<b>67</b>
6.1	Definitions . . . . .	67
6.2	Measurement Results . . . . .	68
6.3	Summary on Steady-State Measurement Results . . . . .	73
<b>7</b>	<b>Time-Resolved Results and Aerodynamic Stability Analysis</b>	<b>75</b>
7.1	Single-Blade Reference Test Cases . . . . .	76
7.1.1	Summary of Aerodynamic Stability of Single-Blade Reference Test Cases . . . . .	86
7.2	Cluster Test Cases . . . . .	87
7.2.1	Two-Blade Cluster . . . . .	87
7.2.2	Four-Blade Cluster Simulating Torsion . . . . .	94
7.2.3	Summary of Aerodynamic Stability of Cluster Test Cases . . . . .	102
7.3	Prediction of the Aerodynamic Values of Cluster-Blades by Using Single-Blade Test Results . . . . .	105
7.3.1	Two-Blade Cluster . . . . .	106
7.3.2	Four-Blade Cluster Simulating Torsion . . . . .	111
7.3.3	Summary and Conclusion of Predicting the Aerodynamic Values of Cluster-Blades by Using Single-Blade Test Results . . . . .	114

<b>8 Summary, Conclusions and Outlook</b>	<b>117</b>
8.1 Summary and Conclusions . . . . .	117
8.2 Recommendations for Future Work . . . . .	122
 <b>Bibliography</b>	 <b>123</b>
 <b>A Appendix</b>	 <b>127</b>
A.1 Blade Surface Isentropic Mach-Number at 25% and 90% Blade Height . . . . .	127
A.2 Steady-State Flow Conditions Compared to Rottmeier [2003] and Beretta [2006]	130
A.3 Additional Graphs of the Single-Blade Test Case with Flap-Bending Oscillation Direction . . . . .	133
A.4 Determination of the Global Aerodynamic Damping of the Four-Blade Cluster Test Case . . . . .	134
A.5 Additional Graphs of Predicting the Aerodynamic Values of Cluster-Blades by Using Single-Blade Test Results . . . . .	136
A.5.1 Two-Blade-Cluster with Flap-Bending Oscillation Direction . . . . .	136
A.5.2 Two-Blade-Cluster with Torsion Oscillation Direction . . . . .	138
A.5.3 Impact of the Number of Applied Influence Coefficients of the Four-Blade Cluster Test Case . . . . .	140





# List of Figures

1.1	The Collar triangle of aeroelastic forces. . . . .	2
1.2	First three dominant single-blade vibration mode-shapes with displacement contours. . . . .	4
1.3	Examples of grouped blades, tied together or with snubber. . . . .	4
1.4	Example of shrouded and cantilevered compressor vanes. . . . .	5
1.5	Example of welded-in-pair, cantilevered and interlock shroud connections. . . . .	5
1.6	Vibration model, natural frequencies and mode-shapes for blade groups varying up to a combination of six blades. . . . .	6
1.7	Mode shapes for a group of six staggered blades. . . . .	7
2.1	Two examples of nodal diameter of a blade-row for a single-blade case and for a two-blade cluster case. . . . .	15
2.2	Definition of positive ICPA (respectively IBPA), of blade $n$ and cluster $j$ indexing. . . . .	16
2.3	General processing procedure from influence coefficients to single-blade traveling-wave coefficients. . . . .	19
2.4	Effect of the inter-blade phase angle on the traveling-wave mode response; superposition of the influence coefficients of blades -1, 0 and +1 for four inter-blade phase angles. . . . .	20
2.5	Summary of the superposition principle showing the effect of the traveling-wave mode response. . . . .	21
2.6	Specific processing procedure from influence coefficients to cluster-blade traveling-wave coefficients. . . . .	24
2.7	Determination of the aerodynamic force and moment coefficients. . . . .	27
2.8	Illustration of the reduced frequency. . . . .	30
3.1	EPFL air supply network. . . . .	32
3.2	Schematic view of the non-rotating annular test facility. . . . .	33
3.3	Detailed schematic view of the test facility. . . . .	34
3.4	Tower of the turbine cascade assembly, bending and torsion blade-suspension system. . . . .	36
3.5	Additional slots in the spring and mass element for the fitting key. . . . .	37
3.6	Cascade vibration control system. . . . .	38

## List of Figures

---

3.7	Overview of steady, unsteady and shroud wall pressure-tap distributions along the cascade. . . . .	39
3.8	Steady and unsteady pressure-tap locations along the blade surface, merged onto one blade. . . . .	39
4.1	Definition of the blade vibration coordinate system. . . . .	42
4.2	Example of a welded-in-pair low-pressure turbine cluster deformation. . . . .	44
4.3	Oscillation directions applied at the two-blade cluster. . . . .	45
4.4	Model of a four-blade cluster oscillating with a torsional mode-shape. . . . .	46
4.5	Modelling of the torsional cluster movement by using an axial-bending oscillation direction for the individual cluster-blades. . . . .	47
5.1	5-hole L-shaped probe and probe traversing locations relative to the blade LE and TE. . . . .	52
5.2	Probe traversing measurement grid. . . . .	53
5.3	Embedded unsteady pressure transducer. . . . .	55
5.4	Displacement transducer, Vibro-Meter <sup>®</sup> TQ 402. . . . .	56
5.5	Description of the measuring and post-processing procedure of the four-blade cluster simulating a torsional movement. . . . .	57
5.6	Schematic view of the data acquisition and control system. . . . .	58
5.7	Overview of the unsteady data-reduction process for UPTs and blade displacement transducers. . . . .	62
5.8	Application of the unsteady pressure transducer calibration device. . . . .	63
5.9	Illustration to determine the random error related to the unsteady pressure measurements. . . . .	64
5.10	Averaged raw unsteady pressure amplitude spectrum for the single-blade test case SB-A (axial-bending oscillation direction). . . . .	65
5.11	Averaged raw blade oscillation amplitude spectrum for the single-blade test case SB-A (axial-bending oscillation direction). . . . .	66
6.1	Isentropic Mach-number distribution along the blade surface at mid-span (50% blade-height) of all test cases. . . . .	70
6.2	Isentropic Mach-number distribution along the blade surface for three different channel heights. . . . .	70
6.3	Schematic view of the secondary flow. . . . .	71
6.4	Isentropic Mach-number distribution along the outer wall (tip). . . . .	72
7.1	Unsteady pressure coefficient amplitude and phase lag of the single-blade test case SB-A (axial-bending oscillation direction). . . . .	77
7.2	Unsteady pressure coefficient amplitude and phase lag of the single-blade test case SB-T (torsion oscillation direction). . . . .	77
7.3	Schematic example of a single-blade traveling-wave with an axial-bending and torsion oscillation direction for an inter-blade phase angle of $\pm 180^\circ$ . . . . .	78

7.4	Normalized local aerodynamic work coefficient of the single-blade test cases, SB-A, SB-F and SB-T. . . . .	81
7.5	Influence coefficient of the normalized aerodynamic work coefficient of the single-blade test cases, SB-A, SB-F and SB-T. . . . .	83
7.6	Influence coefficient of the normalized global aerodynamic work coefficient of the single-blade test cases, SB-A, SB-F and SB-T. . . . .	84
7.7	Normalized global aerodynamic damping coefficient of the single-blade test cases, SB-A, SB-F and SB-T. . . . .	85
7.8	Example of the two-blade cluster oscillation with axial-bending oscillation direction, test case C2-A. . . . .	87
7.9	Normalized local aerodynamic work coefficient of cluster-blades A and B of the two-blade cluster test cases, C2-A, C2-F and C2-T. . . . .	89
7.10	Normalized global aerodynamic damping coefficient of the two-blade cluster test cases, C2-A , C2-F and C2-T. . . . .	91
7.11	Overview of the four-blade cluster displaying the normalized local aerodynamic work coefficient. . . . .	95
7.12	Detailed normalized local aerodynamic work coefficient of cluster-blades D and A of the four-blade cluster, simulating a torsional movement of the cluster. . . . .	98
7.13	Detailed normalized local aerodynamic work coefficient of cluster-blades A and B of the four-blade cluster, simulating a torsional movement of the cluster. . . . .	98
7.14	Detailed normalized local aerodynamic work coefficient of cluster-blades B and C of the four-blade cluster, simulating a torsional movement of the cluster. . . . .	99
7.15	Detailed normalized local aerodynamic work coefficient of cluster-blades C and D of the four-blade cluster, simulating a torsional movement of the cluster. . . . .	99
7.16	Normalized global aerodynamic damping of the four-blade cluster C4-A-S-T, shown per cluster-blade. . . . .	101
7.17	Procedure to predict the aerodynamic values of individual cluster-blades by using single-blade measurement data as input. . . . .	105
7.18	Normalized local aerodynamic work coefficient of cluster-blades A and B of the predicted two-blade cluster test case C2-A. . . . .	107
7.19	Normalized global aerodynamic damping coefficient of the predicted two-blade-cluster test case C2-A. . . . .	109
7.20	Impact of the number of applied influence coefficients to simulate either the aerodynamic damping coefficient of cluster-blade A or B of the two-blade cluster case C2-A. . . . .	110
7.21	Normalized local aerodynamic work coefficient of cluster-blades A and B of the predicted four-blade cluster test case C4-A-S-T. . . . .	112
7.22	Normalized local aerodynamic work coefficient of cluster-blades C and D of the predicted four-blade cluster test case C4-A-S-T. . . . .	113
7.23	Normalized global aerodynamic damping coefficient of the predicted four-blade-cluster test case C4-A-S-T. . . . .	114

## List of Figures

---

A.1	Isentropic Mach-number distribution along the blade surface at 25% blade-height of all test cases. . . . .	128
A.2	Isentropic Mach-number distribution along the blade surface at 90% blade-height of all test cases. . . . .	129
A.3	Comparison of the isentropic Mach-number distribution along the blade surface to Rottmeier [2003] and Beretta [2006]. . . . .	132
A.4	Unsteady pressure coefficient amplitude and phase lag for the single-blade test case SB-F (flap-bending oscillation direction). . . . .	133
A.5	Theorem on intersecting lines of the four-blade cluster case. . . . .	135
A.6	Normalized local aerodynamic work coefficient of cluster-blades A and B of the predicted two-blade cluster test case C2-F. . . . .	136
A.7	Normalized global aerodynamic damping coefficient of the predicted two-blade cluster test case C2-F. . . . .	137
A.8	Normalized local aerodynamic work coefficient of cluster-blades A and B of the predicted two-blade cluster test case C2-T. . . . .	138
A.9	Normalized global aerodynamic damping coefficient of the predicted two-blade cluster test case C2-T. . . . .	139
A.10	Impact of the number of applied influence coefficients to simulate the aerodynamic damping coefficient of cluster-blades A or B of the four-blade cluster case test C4-A-S-T. . . . .	140
A.11	Impact of the number of applied influence coefficients to simulate either the aerodynamic damping coefficient of cluster-blades C or D of the four-blade cluster case test C4-A-S-T. . . . .	141

# List of Tables

1.1	Common structural and aerodynamic parameters influencing the aeroelasticity. . . . .	3
1.2	Investigated test cases. . . . .	12
2.1	Kinematic relation between the single-blade influence coefficient terms and the cluster traveling-wave terms of a four-blade cluster oscillating in torsional motion. . . . .	25
3.1	Main blade attributes. . . . .	35
3.2	Relation between the curvilinear coordinate $s$ and the steady and unsteady pressure-tap locations along the blade surface. . . . .	40
4.1	Test case specifications of the two-blade cluster configurations. . . . .	45
4.2	Test case specifications of the four-blade cluster configuration. . . . .	48
4.3	Test case specifications of the single-blade configurations. . . . .	49
6.1	Steady-state mean flow quantities at mid-span (50% blade-height). . . . .	68
6.2	Blade surface isentropic Mach-number on PS at mid-span (50% blade-height). . . . .	69
6.3	Blade surface isentropic Mach-number on SS at mid-span (50% blade-height). . . . .	69
7.1	Unsteady measurement specifications of the single-blade test cases. . . . .	76
7.2	Unsteady measurement specifications of the two-blade cluster test cases. . . . .	88
7.3	Unsteady measurement specifications of the four-blade cluster test case. . . . .	94
7.4	Kinematic relation between single-blade influence coefficients and cluster traveling-wave coefficients of the two-blade cluster test cases. . . . .	106
A.1	Blade surface isentropic Mach-number on PS at 25% blade-height. . . . .	127
A.2	Blade surface isentropic Mach-number on SS at 25% blade-height. . . . .	127
A.3	Blade surface isentropic Mach-number on PS at 90% blade-height. . . . .	128
A.4	Blade surface isentropic Mach-number on SS at 90% blade-height. . . . .	128
A.5	Comparison of steady-state mean flow quantities vs. Rottmeier [2003] and Beretta [2006]. . . . .	131



# Nomenclature

## *Latin Symbols*

Symbol	Unit	Meaning
$a$	[-]	blade displacement
$b$	[ $m$ ]	blade span width
$c$	[ $m$ ]	blade chord length
$\vec{c}_M$	[-]	unsteady moment coefficient vector
$\tilde{c}_p$	[-]	complex unsteady pressure coefficient
$d$	[-]	damping matrix
$ds$	[-]	infinitesimal arcwise surface component per unit span
$f$	[ $Hz$ ]	excitation frequency during controlled vibration measurements
$\vec{F}$	[ $N$ ]	force vector
$h$	[ $m$ ]	blade bending displacement
$i$	[-]	complex number
$I$	[-]	individual blade in the cluster
$j$	[-]	cluster number
$J$	[-]	total number of clusters
$k$	[-]	reduced frequency
$k$	[ $N/m$ ]	stiffness matrix
$L$	[ $m$ ]	pitch (circumferential distance) between two neighboring blades
$m$	[ $kg$ ]	mass matrix
$M$	[-]	Mach-number
$n$	[-]	blade number
$N$	[-]	total number of blades
$\vec{n}$	[-]	normal vector to surface element
$p$	[ $Pa$ ]	pressure
$p_{dyn,n}$	[ $Pa$ ]	n-th unsteady pressure
$q_{\beta,n}$	[-]	complex traveling-wave force coefficient
$\vec{r}_0$	[ $m$ ]	vector to the axis of rotation
$\vec{r}_s$	[ $m$ ]	vector to a location on the blade surface

## Nomenclature

---

Symbol	Unit	Meaning
$R_{Hub}$	[ $m$ ]	hub radius
$R_{Tip}$	[ $m$ ]	tip radius
$s$	[-]	non-dimensional curvilinear coordinate
$\mathfrak{s}$	[ $m$ ]	dimensional curvilinear coordinate
$t$	[ $s$ ]	time
$T$	[ $K$ ]	temperature
$T$	[ $s$ ]	oscillation period
$U$	[ $m/s$ ]	flow velocity
$w$	[-]	local aerodynamic work coefficient
$W$	[-]	global aerodynamic work coefficient

## Greek Symbols

Symbol	Unit	Meaning
$\alpha$	[ $rad$ ]	blade angular displacement
$\beta$	[ $^\circ$ ]	relative flow angle
$\Gamma_\lambda$	[ $^\circ$ ]	inter-cluster phase angle
$\zeta$	[ $rad$ ]	torsional direction
$\eta$	[ $m$ ]	circumferential bending direction
$\kappa$	[-]	ratio of specific heat for air
$\lambda$	[-]	general indices, natural number
$\xi$	[ $m$ ]	axial-bending direction
$\Xi$	[-]	global aerodynamic damping coefficient
$\sigma_\lambda$	[ $^\circ$ ]	inter-blade phase angle
$\Upsilon$	[ $J$ ]	global aerodynamic work
$\varphi$	[ $^\circ$ ]	phase shift between pressure signal and blade oscillation movement

## Diacritic

Abbreviation	Meaning
$\sim$	complex number
$-$	modal
$\wedge$	peak value, modulus
$\rightarrow$	vector



***Superscript***

Abbreviation	Meaning
0	reference blade
$n$	blade number

***Subscript***

Abbreviation	Meaning
1	inlet conditions
2	outlet conditions
$\alpha$	rotational vibration direction
amb	ambient conditions
ax	axial direction
A	cluster-blade A
bl	blade
B	cluster-blade B
C	cluster
C	cluster-blade C
D	cluster-blade D
$\lambda$	natural number
fl	flap direction
F	force
h	bending vibration direction
is	isentropic conditions
I	blade in the cluster
IC	influence coefficient
ms	mode-shape
M	moment
n	blade number
s	location on the blade surface
stat	static conditions
steady	steady conditions
SB	single-blade
t	total conditions
tap	pressure tap along the blade surface
TW	traveling-wave
$\infty$	infinite conditions

## Nomenclature

---

### Acronyms

Abbreviation	Meaning
1D	one-dimensional
2D	two-dimensional
3D	three-dimensional
A/D	analog/digital
ADTurB I	Aeromechanical Design of Turbomachine Blades
ADTurB II	Aeroelastic Design of Turbine Blades
BNC	Bayonet Neill Concelman connection
C2-A	cluster with two blades, vibrating in axial-bending direction
C2-F	cluster with two blades, vibrating in flap-bending direction
C2-T	cluster with two blades, vibrating in torsional direction
C4-A-S-T	cluster with four blades, vibrating in axial-bending direction per cluster-blade and simulating a torsional movement of the cluster
CAD	computer assisted design
CFD	computational fluid dynamics
CPU	central processing unit
CT	axis of rotation
DAQ	data acquisition
DC	direct current
DS	relative to downstream measuring plane of the test section
DSA	digital sensor array
EPFL	École Polytechnique Fédérale de Lausanne
FFT	fast Fourier transform
FUTURE	Flutter-Free Turbomachinery Blades
FP7	EU's Seventh Framework Programme for Research
FS	full scale
GPIB	general purpose interface bus
GTT	Group of Thermal Turbomachinery
HCF	high cycle fatigue
IBPA	inter-blade phase angle
IC	influence coefficient
ICPA	inter-cluster phase angle
Im	imaginary part of the complex number
I/O	input/output
LE	blade leading-edge
LPT	low-pressure turbine
PC	personal computer
PS	blade pressure-side

Abbreviation	Meaning
rpm	revolution per minute
RAM	random-access memory
Re	real part of the complex number
SB-A	single-blade vibrating in axial-bending direction
SB-F	single-blade vibrating in flap-bending direction
SB-T	single-blade vibrating in torsional direction
SS	blade suction-side
StD	standard deviation
TCP/IP	Transmission Control Protocol / Internet Protocol
TE	blade trailing-edge
TTL	transistor-transistor logic
TW	traveling-wave
UPT	unsteady pressure transducer
US	relative to upstream measuring plane of the test section



# 1 Introduction

THIS chapter aims to give a brief introduction into the field of aeroelasticity in turbomachinery and continues by detailing the importance of grouping blades to clusters. Thereafter a literature overview related to the state of the art of the discussed subject is presented. The chapter concludes by describing the scope of the work.

## 1.1 Introduction of Aeroelasticity in Turbomachines

Gas turbines as well as jet engines have been used for several decades for energy production or to produce aircraft thrust. During each development step, the efficiency, reliability and cost reduction as well as the environment impact have been improved in order to overcome the increasing output demands. In the past years, different approaches have been tackled to satisfy these requirements, which can be associated with higher aerodynamic loadings and more lightweight blade designs which decrease the blade stiffness. The variation of these factors can lead to flutter of the blade. This means an oscillation at the natural frequency of the blade takes place, which is self-excited and self-sustained due to the interaction of the fluid flow with the mechanical structure. If not properly damped, this effect can cause the failure of the blade in a very short period of time due to excessive stress or high cycle fatigue (HCF). To avoid such an incident, a reliable prediction of stress amplitudes is needed. Considering the aforementioned factors, a simultaneous study of the interaction of vibrational dynamics, the structural elasticity and the aerodynamics on the turbomachinery blading are necessary. This topic is commonly known as aeroelasticity and can be depicted by the so-called “Collar triangle”, shown in Figure 1.1. It was first introduced by Collar [1946] and describes the relation between the involved disciplines. In each of the triangle vertices, the forces influencing the aeroelasticity are noted. These are the inertial forces related to the dynamics of the system, the aerodynamic forces introduced by the fluid mechanics and the elastic forces due to the structural mechanics. The resulting main phenomena of aeroelasticity observed in turbomachines can be identified in the center of the triangle and are the flow-induced vibrations, either flutter or forced response. The latter describes a vibration of the blade which is caused by an external unsteady flow disturbance. In the case of an unsteady

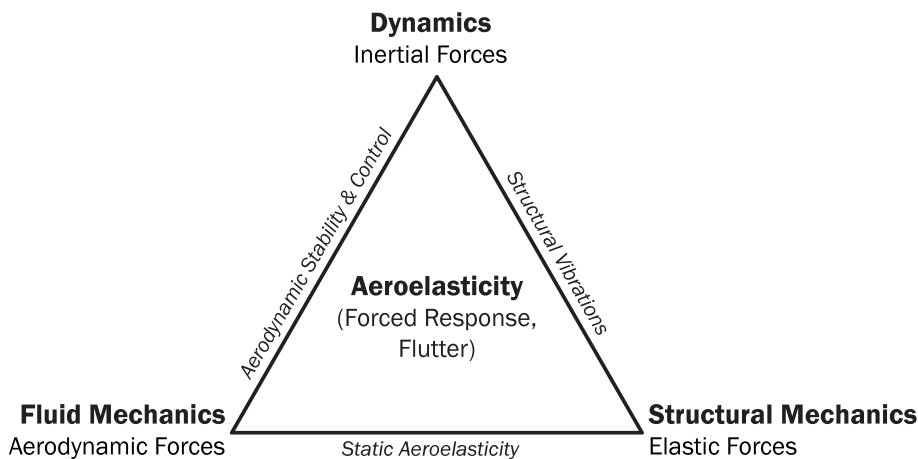


**Figure 1.1:** The Collar triangle of aeroelastic forces (from Collar [1946]).

flow disturbance with a frequency corresponding to a natural frequency of the blade system, resonance occurs which can lead to the failure of the blade. An example of such a disturbance is the fluid-structure interaction of a blade-row subjected to stator wakes. Flutter is the self-excited vibration of a blade and has its source in the presence of pressure fluctuations coming from the blade vibration itself.

## 1.2 Vibration of Single-Blades and Clustered Blades

The prediction of flutter is one of the main problems investigated in recent times. Setting up an experiment capable to simulate flutter as it appears in real turbomachinery is extremely difficult. To overcome the associated problems it is necessary to identify the combination of blade profile and flow condition under which flutter can occur. When this step is accomplished, the next problem to address would be the design and execution of the experiments. One problem encountered here, is how to control flutter in a rotating rig. The problem is related to an effect which is self-excited and self-sustained, leading to the failure of the blade or the supporting structure if not stopped in a short period of time. Hence, a mechanism must be put in place to extract the vibration energy of the blades and limit the self-sustained vibration. These are only a few of the challenges which are necessary to address. For this reason, a different experimental approach has been chosen and applied for decades to circumvent the above mentioned problems. In this method, blades are forced to oscillate in a uniform flow and the generated unsteady loading of the blades is determined. If the results indicate a loading which extracts energy from the flow, the blade vibrations are enhanced and flutter will likely occur. On the contrary, if energy is transferred from the vibrating blade to the flow, the mechanism of self excitation is avoided and flutter is thus prevented. Compared to the previous technique, the latter is more conservative since failure of the blade and the blade structure is less likely to occur and a conclusion of the flutter susceptibility can be made. Nevertheless, the drawback is that the physics of flutter itself cannot be investigated with this method. This

## 1.2. Vibration of Single-Blades and Clustered Blades

type of measurement technique is often referred to as “Controlled Vibration” since the blades are forced into a controlled vibration. For the past few decades, this experimental procedure has been used and compared to computational prediction models and thus has significantly improved the design criteria and the prediction models of turbomachinery blading. An overview of the most common aerodynamic and structural parameters investigated is listed in Table 1.1. Some of the parameters were analyzed in more detail than others.

Structural parameters	Aerodynamic parameters
cascade geometry:	incidence angle
gap-to-chord, number of blades,	blade-loading
blade geometry, blade twist,	separation point
hub-to-tip ratio, aspect ratio,	pressure distribution on blade surface
stagger angle,	shock position and motion
shroud location and shroud angle,	inlet and exit conditions
blade clustering,	relative inlet Mach number
number of blades per cluster	distortion pattern
inter-blade phase angle	velocity and pressure defects
mode-shape	reduced frequency
mechanical damping	
extent of coupling among blades	
mistuning	

**Table 1.1:** Common structural and aerodynamic parameters influencing the aeroelasticity (from Srinivasan [1997]).

The investigation of this thesis is focused on some of these parameters, which are blade clustering, the number of blades per cluster and the mode-shape. These parameters were chosen for several reasons, for example the mode-shape, which is one parameter that was determined by several research studies as having a major influence on flutter stability. This is shown by an analytical study performed by Bendiksen and Friedmann [1982]. They showed, for a large range of flow regimes, that aerodynamic damping depends on the mode-shape of the blades oscillating in a cascade and differs for torsion and bending. An illustration of the three fundamental (first order) mode-shapes is given in Figure 1.2. They have certain eigenfrequencies (natural frequency) at rest, which are a function of the centrifugal forces, or rather the rotational speed of a turbomachine.

One way to increase the aerodynamic damping is to fix blades together. Compared to individual blades, this type of fixation restrains the movement of the blade to some extent. Besides the aerodynamic impact, which is due to limiting the aerodynamic interactions between neighboring blades, grouping blades also influences the structural aspects of the blades due to an increase in the stiffness. Different types of such shrouded blades can be identified and were first reported by Armstrong [1967]. To create a connection, rods between blades are used to group them. In this case, the intended effect of increasing the stability was achieved but the hole necessary to attach the rods to the blade introduced structural stresses which were not

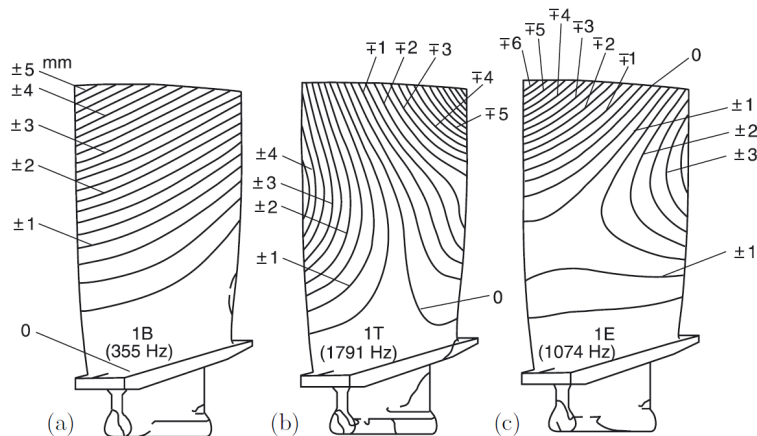


**Figure 1.2:** Fundamental single-blade vibration mode-shapes with displacement contours shown for (a) first flap, (b) first torsion and (c) first edgewise modes (from Grieb [2009]).

satisfactory for service. In a next step, instead of the rods, integral platforms were positioned part way along the span, so that they touched those of the adjacent blades. This connection is called “snubber” due to the damping effect of the design. As Armstrong [1967] reported, the second configuration of snubber blades complied with the specifications and was used in service. Illustrations of these two types of shroud connections are shown in Figure 1.3.

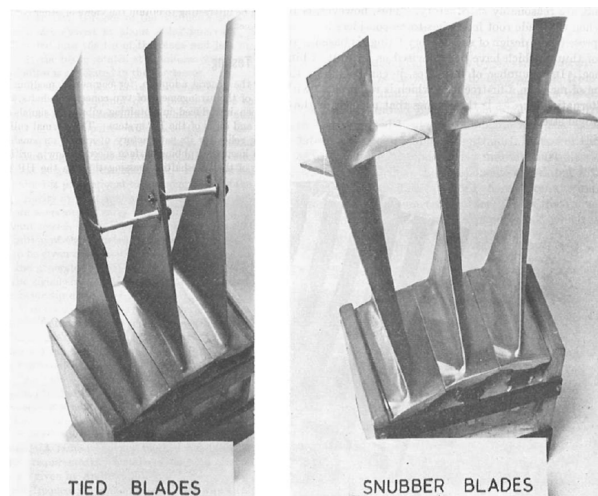


**Figure 1.3:** Left: tied blades, right: snubber blades (from Armstrong [1967]).

In general, the shroud is seen as a connection between the individual blades in the circumferential direction. It can be placed at different radial positions depending on the intended use, for example to decrease the number of pieces in a blade-row. A certain amount of blades are therefore manufactured as one piece, thus being fixed together at the hub and tip. Furthermore, it can be used to change the mode-shape of single-blades (free-standing blade) by fixing several blades together and thus creating a new mode-shape. In a blade-row the number of blades per shroud piece can be arbitrary, since there is no necessity of a circumferential or



## 1.2. Vibration of Single-Blades and Clustered Blades

cyclical symmetry. In the case of compressor vanes, an example is displayed in Figure 1.4 showing the assembly of five vanes connected by an integral shroud. Another example for connected blades is presented in Figure 1.3, in which the snubber represents the shroud connection. For low-pressure turbine blades, tip shrouds are commonly used. In addition to the increase of stiffness, a reduction of the tip losses is achieved. A schematic example with two blades is depicted in Figure 1.5, displaying two possible connection types. From left, the first displays the base-line (cantilevered), the second a welded-in-pair combination and the third an interlock connection. On the right a cluster of five turbine blades welded together is shown. It should be stressed that the aforementioned interlock connection is not necessarily fully locked and can allow some slipping of the blades in order to relax the coupling in certain directions. For the sake of clarity, it should be stated that some literature utilizes the terms “sector of blades”, “blade packet” or “cluster of blades” in order to refer to a connection of blades at the tip shroud.

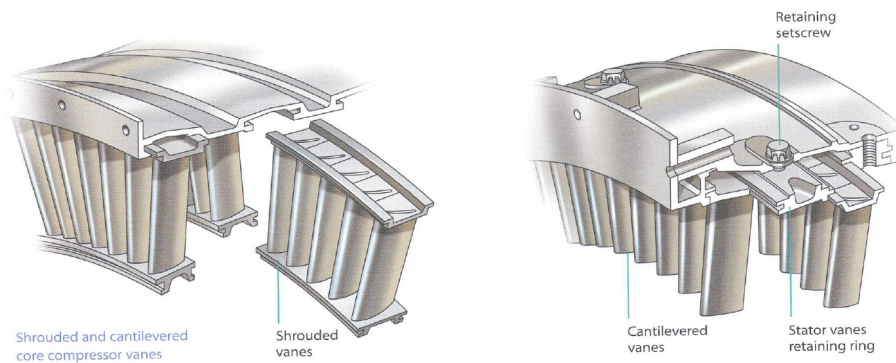


**Figure 1.4:** Example of shrouded (left) and cantilevered (right) compressor vanes (from Rolls Royce plc. [2005]).

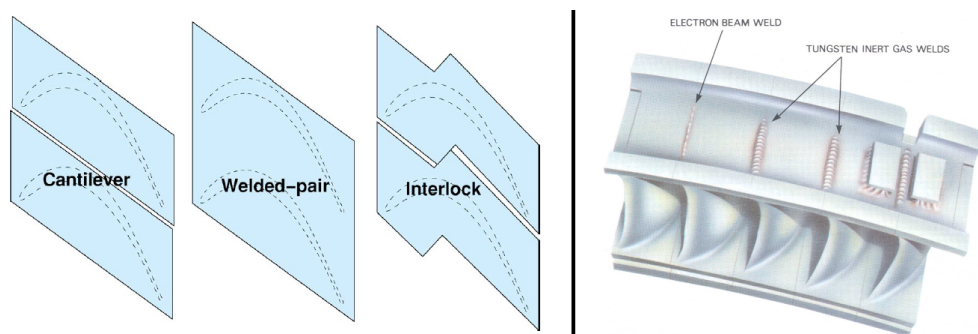


**Figure 1.5:** Left: schematic example of two blades, cantilevered (single-blade), welded-in-pair and interlock shroud-connections (from Corral et al. [2007]). Right: example of five turbine-blades which are welded together (from Rolls Royce plc. [1996]).

These possibilities of different shroud connections imply that it is essential to accurately specify the boundary conditions at the shroud interfaces. This is of importance, since the prediction of the resulting blade-group mode-shapes rely on this specification. The variety of possible mode-shapes is illustrated using the approach of Ewins [1988c]. In this reference the

## Introduction

shroud connections are simulated by using a simple one-dimensional mass-spring parametric model (Figure 1.6 (a)). This, in order to identify the basic characteristic mode-shapes of groups of blades (Figure 1.6 (b)). Starting with one blade, the number of blades increases up to six per group. Next to the mode-shapes, the related natural frequencies are indicated. A general trend can be identified showing that one fundamental mode with all blades vibrating in-phase (left column) seems to be unaffected by the shroud stiffness. It is followed by a group of  $(N-1)$  modes, which strongly depend on the shroud stiffness, with  $N$  being the number of blades per group. Furthermore, it should be noted that the phase angle between neighboring blades can be either  $0^\circ$  or  $180^\circ$ . As this model is one-dimensional, a two-dimensional model is of interest taking the staggering of the blade into account. Ewins [1988c] modeled this as well and concluded that, similar to the one-dimensional model, a single fundamental mode-shape is followed by a group of shroud-controlled modes in a relatively narrow frequency band.

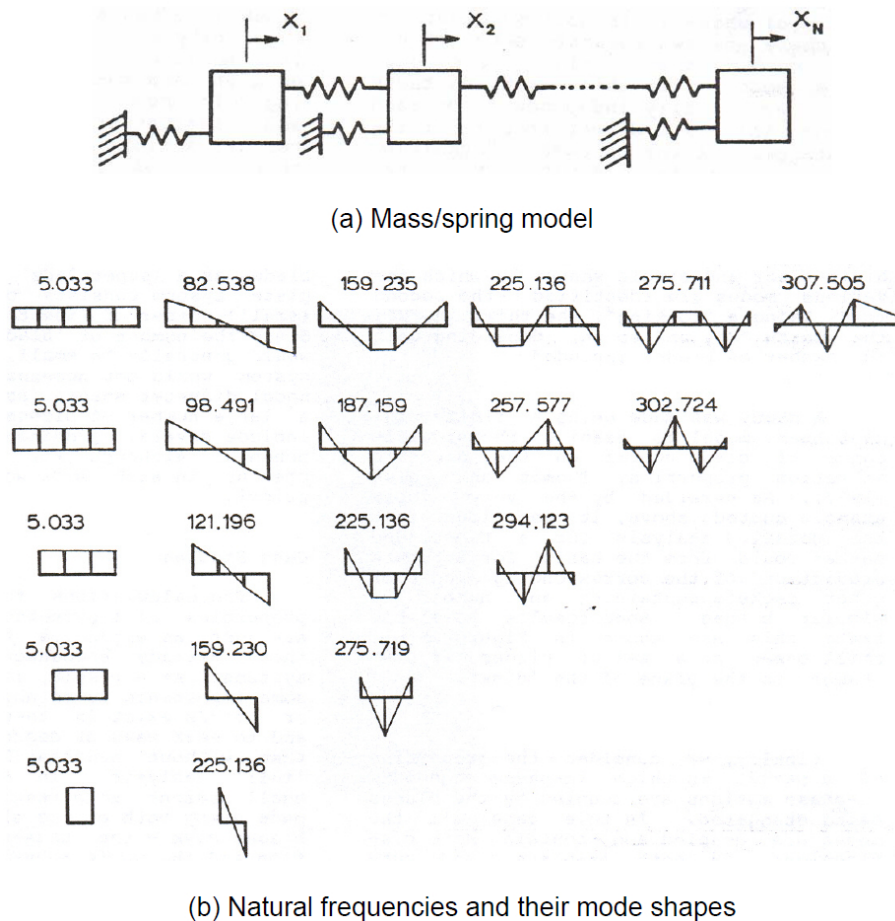


**Figure 1.6:** Vibration model for blade groups varying up to a combination of six blades (from Ewins [1988c]).

The vibration modes he identified are coupled motions which are in- and out-of-phase with the adjacent blades in the group and allow the blades a movement in both dimensions, which

he called out-of- and in-plane directions. Depending on the type of connection, some group modes may be more dominant than others. In Figure 1.7 an example of a six-bladed group is given displaying three modes: left, in both directions (out-of- and in-plane); middle, dominant in the out-of-plane direction and out-of-phase and, right, in the out-of-plane direction and in-phase.

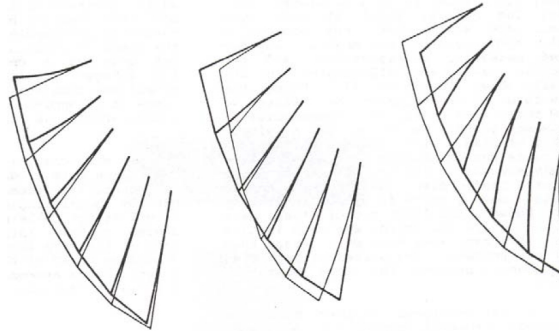


**Figure 1.7:** Mode shapes for a group of six staggered blades (from Ewins [1988c]).

Introducing shroud connections and thus grouping blades into clusters creates new types of mode-shapes. These have a direct impact on the overall stability on the blade-row. From a structural point of view the stiffness increases for most of the cases. From an aerodynamic point of view, a change in the flutter stability appears due to the kinematics of the new mode-shapes. Hence, it is evident that generating and validating knowledge in this discipline of introducing shrouds to increase the aeroelastic stability of blades will help engine designers to accomplish the present challenges on new turbomachines.

### 1.3 State of the Art

In Srinivasan [1997], a comprehensive overview of general vibration problems is provided. The article introduces the different aspects to be considered for flutter and resonant vibrations. Also the AGARD Manual, Verdon [1987] and Ewins [1988a,b,c], serves as an effective overview and is even more detailed.

The following literature overview aims to give a brief summary of the investigations of single-blade (free-standing blade) flutter analysis and then focuses on grouped (clustered) turbine-blades. For both, the focus is directed towards experimental investigations while considering the main computational developments.

A thorough overview of the work performed in the early 1980s can be found in Bölcs and Fransson [1986]. The editors created a set of two-dimensional test cases by gathering the experimental, numerical and theoretical data of researchers in this field. It should be stressed that these so-called “standard configurations” are nowadays still used as validation test cases for code developers in the field of aeroelasticity.

## Introduction

---

The appearance of flutter in turbomachinery is usually found in an arrangement of blades and therefore a blade-row rather than a single-blade is investigated. Each blade induces through its motion a change in the flow field, which influences the pressure response on itself as well as on the adjacent blades. This so-called aerodynamic coupling is largely influenced by the motion of neighboring blades. Crawley [1988], for example, characterized the oscillatory motion of a tuned blade-row during flutter as a so-called “traveling-wave” mode. It is defined so that all blades oscillate with an identical frequency, mode-shape and amplitude but with a specific phase-lag between neighboring blades. In this “traveling-wave” formulation, all blades oscillate, while the response on one blade is measured. It is shown by Hanamura et al. [1980] and Crawley [1988] that the response of the “traveling-wave” formulation can be linearly expressed in the “influence coefficient” formulation. In the latter, each blade in the blade-row is oscillated individually and the response on itself and on the neighboring blades are determined. By superimposing each of the individual influences, the result is identical to the response of one blade in “traveling-wave” formulation.

A comprehensive literature summary of experimental and numerical predictions performed for both methods can be found in Bölcs et al. [1989]. Furthermore, they experimentally validated the linear relationship between the “influence coefficient” and “traveling-wave” formulation for two-dimensional single-blade bending mode-shapes in sub- and transonic flow conditions. Later, Nowinski and Panovsky [2000] continued the work investigating the torsion mode-shape in low-pressure turbines. Apart from validating the superposition principle, they identified that the position of the torsion-axis has a significant influence on the aerodynamic damping of the blade. The outcome of the prior investigations was used by Panovsky and Kielb [2000] to develop a method to graphically represent the impact of the torsion-axis position on the aerodynamical damping. This was achieved by using the superposition principle of the three fundamental mode-shape directions and by taking into account the influences of the blade itself and its direct neighbors in the “influence coefficient” formulation.

A combined analysis of forced response and flutter was performed by Rottmeier [2003]. The intention of this investigation was to prove the validity of the linear superposition principle of local unsteady pressures on the blade due to upstream generated gusts and the vibration of the cascade in traveling-wave mode. The validation was successfully shown for sub- and transonic flow-regimes excluding flows with shocks. In a follow-up project, Beretta [2006] investigated the influence of frequency mistuning on the forced response of a blade-row vibrating in torsion mode-shape. Additionally, a mistuning of the bending mode-shape was studied. The frequency mistuning study led to a simplified frequency mistuning model which is capable of qualitatively reproducing the effects of frequency mistuning and coupling. The bending mode-shape mistuning study showed that the value of the forced response amplitudes was almost identical for both mistuning patterns.

In the studies of Vogt [2005], the aeroelastic response phenomenon was investigated in the influence coefficient domain. In a sector cascade, one blade was oscillated in various three-dimensional rigid-body modes and the unsteady response on several blades was measured. Additionally, a two- and three-dimensional linearized unsteady Euler analyses was performed. Vogt [2005] identified that considerable three-dimensional effects are present, which harm

the prediction accuracy for flutter stability when employing a two-dimensional plane model. Although the overall behavior is captured fairly well when using two-dimensional simulations, notable improvement has been demonstrated when modeling fully three-dimensionally and including tip clearance. Vega and Corral [2013] used the traveling-wave and influence coefficient formulation to study the physics of a low-pressure turbine vibrating in the three fundamental mode-shapes with a linearized Navier-Stokes solver. They concluded that the unsteadiness of the flow of the vibrating blade is due to vortex-shedding mechanisms and that the effect of the Mach-number can be neglected on a first approximation for the unsteady pressure phase. Additionally, it was concluded that the unsteady pressure fluctuation on airfoils far away from the reference airfoil is mainly driven by acoustic perturbations.

To the knowledge of the author, Armstrong [1967] was the first who investigated the supporting effect of a cluster. As stated in the previous section, he introduced a shroud connection between turbine-blades at about mid-span height. This connection is further known as a snubber (see also Figure 1.3). It should be noted that this design is still used in current turbo-machinery designs.

Listvinskaya [1975] developed a code to calculate the natural frequencies and mode-shapes of large packets of twisted steam turbine-blades fixed at two distances from the root by wires and on the tip by a belt. The prediction of the developed code was validated with analytical computations of a packet with 10 blades. Nagarajan and Alwar [1985] developed a three-dimensional model with iso-parametric quadratic elements to analyze grouped steam turbine-blades. Two blades per group were analyzed, one with bending mode-shape and one with torsion. They validated qualitatively their model, which was able to represent the natural vibrations of the blades due the presence of a shroud.

The linear numerical investigation of Whitehead and Evans [1992] focused on using the data of single-blades (free-standing blades) to calculate the stability of grouped turbine-blades. The analysis confirmed the stabilizing effect of grouping blades together. They analyzed packets of five and six blades, all having the same frequency and amplitude, while the blades in a group could have different mode-shapes. The numerical results agreed qualitatively with the experimental results for two low-pressure steam turbine examples. Kahl [1995] pursued this further and developed a different numerical procedure, called the “direct” method, which requires as many passages as airfoils are present in one cluster. Different to that of Whitehead and Evans [1992], his method overcomes the rigid-body limitation on the airfoil section, since a proper mode for each airfoil in the cluster can be specified. The investigated case with the time-linearized Euler method was a cluster of three airfoils vibrating in the first bending mode-shape. For sub- and transonic flow conditions, the aerodynamic damping was well predicted. Limitations were outlined in the case of strong three-dimensional effects and when viscous unsteady effects become dominant, for example in the case of stall flutter.

Using the results from Whitehead and Evans [1992] and Kahl [1995], Chernysheva [2004] continued the work and performed a parameter study investigating the influences of varying amplitudes and phase angles on sectors of up to six blades covering the three fundamental mode-shapes. The study was performed using a two-dimensional inviscid linearized flow

model and the simulation of the sectors is based on the principle of Lane [1956]. Critical (towards flutter) reduced frequency maps are provided for torsion- and bending-dominated sectored vane mode-shapes. The conclusion of this investigation was that grouping blades together improves the stability of the blades but does not exclude completely the possibility of flutter.

In recent years, Corral et al. [2004, 2007, 2009] have published results related to this topic. In Corral et al. [2004, 2007], the aerodynamic damping of low-pressure turbines was investigated numerically with linear methods. The focus of these investigations were single-blades (free-standing blades) with different shroud boundary conditions. The change in boundary condition comprises three different configurations: cantilever (single-blade), interlock and welded-in-pair. The main findings of these studies are that welded-in-pair blades have a higher aeroelastic stability than single-blades (free-standing blades) for torsion and circumferential bending modes. Additionally, they concluded that the increase in the aerodynamic damping, due to the modification of the mode-shapes caused by welding the rotor blades in pairs, is smaller than that due to the overall rise in the reduced frequencies of a bladed disk with an interlock design. In Corral et al. [2009], an aeroelastic analysis of a packet of vanes was performed using a linear simplified mass-spring model. The authors identified a set of vane-packet mode-shapes in a close frequency proximity, these are the result of the much higher stiffness of the lower vane-packet in relation to the airfoils. Taking the presence of unsteady aerodynamic forces into account, they concluded that the structural modes may be coupled and form new aeroelastic modes, which can be very different from the purely structural modes. These new modes may change dramatically the flutter margin of the vane packet. The authors highlight that these aeroelastic modes are not covered when using the standard uncoupled methodology, in which the aerodynamic forces of each structural mode are computed independently.

### 1.4 Objective of the Present Work

The literature review presents a variety of parametric studies which used linearized numerical codes to investigate the aerodynamic stability of grouping blades together. Although some of the prediction tools used are validated by experimental results of single-blades, a lack of experimental data of clustered (grouped) airfoils is evident.

Clustering airfoils is identified as a possibility to lower the flutter susceptibility of the configuration with respect to single-blades. Two factors which have an influence on the aerodynamic stability of clustered airfoils are the mode-shape of the individual cluster-blades, as well as the number of airfoils included per cluster. The objective of this work is to study experimentally the influence of selected cluster configurations with respect to their aerodynamic stability. Furthermore the objective is to validate the applicability of the linear superposition principle using single-blades in order to predict cluster configurations on the basis of experiments. This principle is based on the findings of Hanamura et al. [1980] and has been used by various researchers to perform parametric studies related to clustered airfoils.

The present work was part of the European project FUTURE (acronym for Flutter-Free Turbomachinery Blades, Website of the project FUTURE [2008]) with the aim of improving aero-mechanical analysis for aggressively lightweight blade designs by advancing the state-of-the-art in flutter prediction capabilities and design rules.

### 1.5 Scope of the Work

The experimental investigation was performed in the non-rotating annular test facility on a turbine cascade composed of 20 blades. The test facility offers the possibility to control the oscillation for each blade individually with a constant frequency of all blades. This enables to define the vibration amplitude as well as the phase-angle for each blade, so that selected cluster configurations can be simulated, for example a cluster of two blades oscillating in-phase. In addition to individually control the oscillation of each blade, the blade vibration direction can be changed. This variety of blade oscillation combinations and blade vibration directions is used to perform cluster measurements as well as single-blade measurements in traveling-wave modes. Three first order rigid-body mode-shapes for the single-blade cases are selected (torsion, flap- and axial-bending) to serve also as a basis for the cluster investigations. For the study of clusters, two configurations are selected to represent the configurations frequently used in turbomachinery designs:

- The first case is a cluster of two blades and is meant to represent a configuration of two blades welded-in-pair. The mode-shape of this cluster is simulated by controlling the oscillation of the individual blades in a blade-row according to the kinematics of the cluster.
- The second test case reflects a cluster of four blades and represents a package of four vanes cast as a piece performing a torsional movement. In order to simulate the torsional movement, each of the individual blades vibrates in an axial-bending vibration direction with a specific amplitude according to the kinematics of the cluster.

The experimental cluster test cases serve two objectives. One objective is to determine the aerodynamic stability, the other is to validate the applicability of the linear superposition principle, which uses the aerodynamic parameters of the single-blade test cases to predict those of the individual cluster-blades in the cluster. A brief overview of the investigated test cases is documented in Table 1.2.

The study is based on identical steady-state flow conditions for all test cases. To control the equality of the steady-state flow conditions, they are measured at the inlet and outlet of the test section. Additionally, the blade surface pressure is measured at three different span heights: 25% (close to the inner wall/hub), 50% (mid-span) and 90% (close to the outer wall/tip). The unsteady measurements comprise nine pressure taps along the pressure-side and twelve

pressure taps along the suction-side of the blade surface at mid-span height. The vibration amplitudes are measured individually for each blade.

The present work is composed of the following consecutive structure:

- **Chapter 2** introduces the applied theoretical concept and describes the aerodynamic variables used to study the cluster types presented in Table 1.2.
- In **Chapter 3** the experimental setup is described. It details the non-rotating annular test-facility (Bölcs [1983]) and continues by describing the functionality of the used turbine test model and its measuring capabilities.
- The investigated cluster and single-blade test cases are detailed in **chapter 4**.
- **Chapter 5** is dedicated to the applied measurement techniques for the steady-state and the unsteady aerodynamic parameters. It also includes a description of the data-acquisition systems used and the data-reduction techniques applied.
- The steady-state flow conditions used for all unsteady test cases are detailed in **Chapter 6**, including an overview of the leakage flows. It also documents the consistency of the steady-state results by comparing all measurements with one another.
- In **Chapter 7** the results of the single-blade and cluster unsteady measurements are presented. First the single-blade test cases are presented, followed by the cluster test cases as described in Table 1.2. It also shows the applicability of the linear superposition principle using the aerodynamic parameters of single-blades in order to predict those of cluster configurations on the basis of experiments.

Case	Oscillation direction	Number of blades per cluster	Related to a
SB-A	Axial	1	Single-blade
SB-F	Flap		
SB-T	Torsion		
C2-A	Axial	2	Welded in-pair section
C2-F	Flap		
C2-T	Torsion		
C4-A-S-T	Axial simulating torsion	4	Four-blade section

**Table 1.2:** Investigated test cases.



## 2 Theoretical Concept

THIS chapter introduces the theoretical concept applied in the present work and describes the parameters used to study the aerodynamic stability of the single-blade and cluster cases presented in Table 1.2. It is organized as follows:

- Introduction to the fundamental concept of flutter analysis in turbomachines.
- Description of the traveling-wave technique (inter-blade and inter-cluster phase angle).
- Description of the influence coefficient technique.
- Definition of the aerodynamic flutter stability parameters.

## 2.1 Analysis of Aerodynamic Stability in Turbomachines

The following introduction of the analysis of flutter in turbomachines was developed between 1950 and 1980. A comprehensive summary of this work can be found alongside a detailed derivation in the AGARD Manual, Verdon [1987]. As an effective starting point for an overview, the work of May [2012] and Vogt [2005] are recommended.

Methods to identify the flutter stability of a given blade involve the analysis of the structural dynamics as well as the aerodynamics. The balance between the structural and the aerodynamic forces can be described analytically as follows:

$$m\ddot{\vec{x}}(t) + d\dot{\vec{x}}(t) + k\vec{x}(t) = \vec{F}_{damp}(t) + \vec{F}_{disturb}(t) \quad (2.1)$$

where on the left-hand side,  $m$  describes the mass matrix,  $d$  the damping matrix and  $k$  the stiffness matrix. The coordinate  $\vec{x}(t)$  represents the coordinates to describe the torsion and bending directions. The right-hand side  $\vec{F}_{damp}(t)$  describes the aerodynamic damping forces which result from the motion of the airfoil to the fluid. The second term  $\vec{F}_{disturb}(t)$  on the right-hand side describes the aerodynamic forces which are induced by disturbances originating upstream and downstream of the airfoil. In the case of forced response investigations, the second term  $\vec{F}_{disturb}(t)$  would be of importance. Since the present work focuses solely on flutter, only the forces induced by the motion of the airfoil are of interest thus the second term can be neglected. The first step to solve the aeroelastic Equation 2.1 is performed by introducing a modal coordinate system

$$\vec{x}(t) = \vec{e}_{ms} \bar{a} e^{i\omega t} \quad (2.2)$$

where the oscillation directions are described by  $\vec{e}_{ms}$ , the modal displacement by  $\bar{a}$  and the natural frequency by  $\omega$ . Additionally, it is assumed that the structural damping  $d$  in Equation 2.1 can be neglected, since it is generally very small. This assumption is based on the derivation performed by Ewins [1988a]. He pointed out that the structural damping has virtually no effect on the oscillatory component of the natural frequency. Furthermore, he noted that in the case when the damping is relatively localized and when the natural frequencies of the system are close together, it has to be accounted for. By taking into account the previous assumption and introducing the modal coordinate system (see Equation 2.2) in Equation 2.1, after some reformulation the aeroelastic equation can be stated in the modal form as:

$$(-\omega^2 m_{modal} + k_{modal}) \bar{a} - \vec{e}_{ms}^T F_{damp} = 0 \quad (2.3)$$

where  $m_{modal}$  is the modal mass matrix,  $k_{modal}$  is the modal stiffness matrix and  $\vec{e}_{ms}^T F_{damp}$  represents the modal aerodynamic damping forces. The previous equation represents a complex eigenvalue problem. When solved, the stability of the system is described by the eigenvalues of the solution.

Since the structural forces are usually greater than the aerodynamic ones, and therefore do

not impact on the natural frequencies and mode-shapes of the system, the structural and the aerodynamic terms are usually decoupled in the case of turbomachinery application. This assumption of decoupled structural and aerodynamic forces simplifies the analysis, since both can be determined individually. The structural eigen-modes can be determined by assuming no-flow conditions and the influence of the aerodynamic contribution on the stability from a purely unsteady aerodynamic analysis, as described in Section 2.5.

## 2.2 Traveling-Wave Formulation

In order to characterize the coupling effect of adjacent blades, an approach is used which was firstly introduced by Lane [1956]: the so-called “traveling-wave” formulation. This approach describes the oscillatory motion of a tuned blade-row, for example during flutter. It assumes that all blades oscillate with the same mode-shape, amplitude and frequency, whereas the phase lag between adjacent blades is used as the defining factor. This phase lag between two adjacent blades is known as the inter-blade phase angle. In order to fulfill the kinematic constraint of full cycle periodicity the inter-blade phase angle as discrete values is defined, which can be noted as:

$$\sigma_\lambda = \frac{2\pi\lambda}{N} \quad \lambda \in \mathbb{N}, \mathbb{N} = \{0 \dots N - 1\} \quad (2.4)$$

where  $\lambda$  represents the nodal diameter, which defines the oscillation pattern of the blades in the blade-row. The total number of blades in the cascade (blade-row) is represented by  $N$ . Two examples of nodal diameter are illustrated at the top of Figure 2.1.

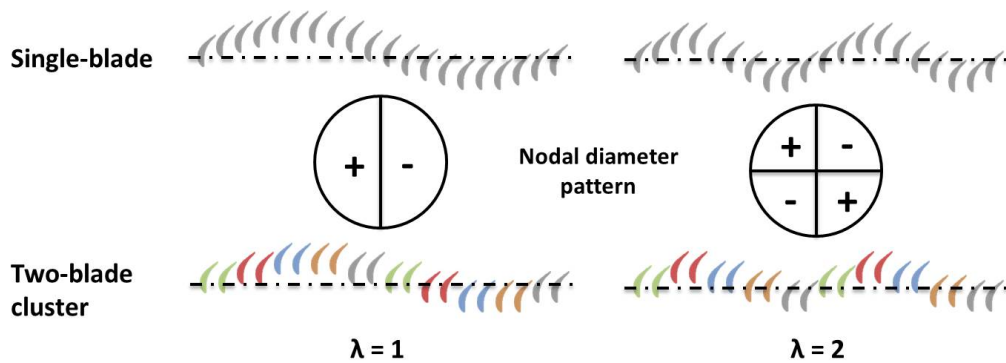


**Figure 2.1:** Two examples of nodal diameter of a blade-row for a single-blade case (top) and for a two-blade cluster case (bottom).

A cluster can be considered as one single structure which fixes blades together. Thus the traveling-wave formulation in the case for cluster is based on similar assumptions as for the single-blade case. It is assumed that all clusters in a blade-row oscillate with the same oscillation direction, frequency and amplitude, whereas the phase lag between two adjacent clusters defines the traveling-wave mode. Therefore, as for single-blades, a variable for the phase lag between adjacent clusters can be defined. In agreement with the inter-blade phase

## Theoretical Concept

angle (IBPA,  $\sigma_\lambda$ ) defined previously (see Equation 2.4), the inter-cluster phase angle (ICPA,  $\Gamma_\lambda$ ) can be written as:

$$\Gamma_\lambda = \frac{2\pi\lambda}{J} \quad \lambda \in \mathbb{N}, \mathbb{N} = \{0 \dots J-1\} \quad (2.5)$$

where  $\lambda$  defines the order of the traveling-wave and also represents the nodal diameter. The total number of clusters in the cascade is represented by  $J$ . Two examples of nodal diameter are illustrated at the bottom of Figure 2.1.

Clusters in a cluster row are indexed in descending order with respect to the direction of rotation. Cluster indices range from 1 to  $J$ . The number of clusters  $J$  is dependent on the type of cluster. As noted before, the inter-blade and inter-cluster phase angles are subject to similar assumptions and therefore the cluster case is used to describe the definition of positive (forward) and negative (backward) traveling-waves. For a positive inter-cluster phase angle, the vibration of cluster  $j$  precedes that of cluster  $j-1$ ; thus the traveling-wave of the cluster moves from one blade's suction-side to the neighboring blade's pressure-side, identical to the direction of rotation. In Figure 2.2 a positive inter-cluster phase angle is depicted. Additionally, the positive inter-blade phase angle for which the vibration of blade  $n$  precedes that of blade  $n-1$ .

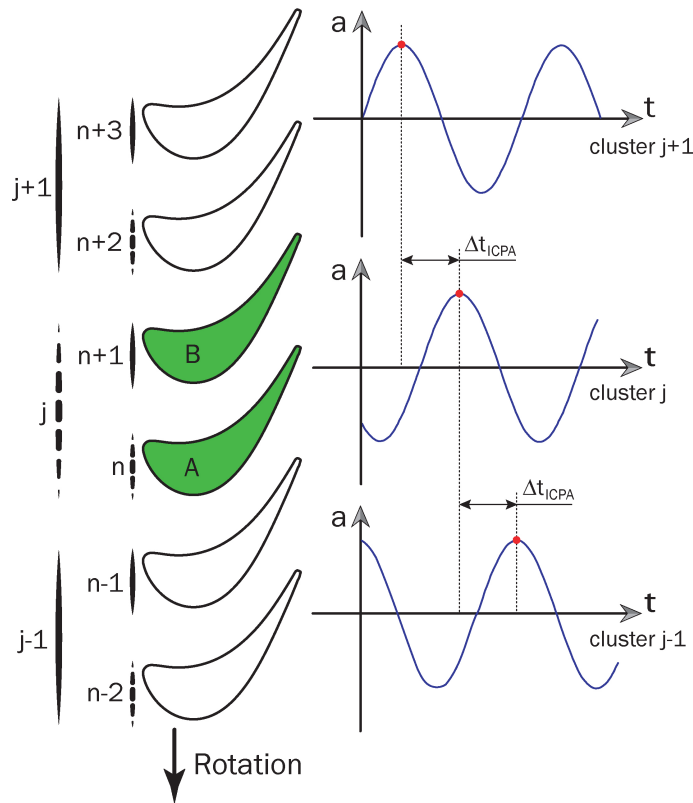


**Figure 2.2:** Definition of positive ICPA (respectively IBPA), of blade  $n$  and of cluster  $j$  indexing. The letters A and B denote the cluster-blades in the cluster  $j$ .

Applying the traveling-wave formulation implies that the aerodynamic forces acting on the blades are determined for all inter-blade phase angles in the case of single-blades, and respectively in the case of clusters for all inter-cluster phase angles. As previously noted, the traveling-wave mode is defined so that all blades are in motion. One blade in the blade-row is therefore influenced by itself and by all other blades at the same time. This implies that the aerodynamic forces can be directly determined on one blade.

### 2.3 Aerodynamic Influence Coefficient Formulation

In the field of turbomachinery, the aerodynamic influence coefficients are used to describe the aerodynamic forces on one blade created by the motion of another blade. This is of interest when the unsteady pressure on one blade is intended to be determined by the influence of several vibrating blades, without having a certain relationship between the blade motions as it would be the case in the traveling-wave formulation. In this work, these influence coefficients and their relation to the traveling-wave formulation will be used to determine the unsteady pressures for individual cluster-blade vibrations.

In order to determine these influence coefficients, a mathematical transformation can be used, which describes the relation between the formulations of traveling-wave and of influence coefficients. On the basis of the work by Hanamura et al. [1980] concerning the introduction of the influence coefficients, Crawley [1988] presented the mathematical relation between traveling-wave and influence coefficients, which states that for small perturbations the influences of the various blades are superimposed linearly. In other words, the response of the observed time-resolved pressures or forces at any given point (e.g. a pressure transducer position on the blade surface) in a vibrating cascade (traveling-wave) can be linearly superimposed on the individual responses of the blade itself and the neighboring blades (influence coefficients) lagged by the respective phase angles between the blades. As this method of Hanamura et al. [1980] uses as a basis similar assumptions as Carta [1967] for the energy method, the following limitations apply:

- no change of the blade's mode-shape due to aerodynamic blade loadings
- no change in the eigenfrequency due to aerodynamic blade loadings
- the blade vibrations are of harmonic nature, as are the resulting unsteady pressure perturbations
- for small perturbations the influences of the various blades superimpose linearly

The influence coefficients can be determined in numerical simulations (see for example Whitehead and Evans [1992], Kahl [1995, 2002], Chernysheva [2004]) or experimentally (see Vogt [2005] and Rottmeier [2003]<sup>1</sup>). Rottmeier [2003] also confirmed for single-blade vibrations

---

<sup>1</sup>The turbine measuring cascade used by the author is identical to the one in the present work.

## Theoretical Concept

---

that measurements using the traveling-wave formulation are identical to those measurements of influence coefficients. The transformation between the response of the coefficients in a vibrating cascade (traveling-wave) and the influence coefficients can be performed by applying a complex Fourier transformation which, according to Schläfli [1989], reads in a general form:

$$\tilde{c}_{Sum}^{\phi_n} = \sum_{n=0}^{N-1} \tilde{c}_{IC}^{n,0} \frac{a_n}{a_0} e^{-i\phi_n} \quad (2.6)$$

where  $\tilde{c}_{IC}^{n,0}$  is the complex influence coefficient of the vibrating blade  $n$ , acting on the non-vibrating reference blade 0,  $\phi_n$  the phase angle of the vibrating blade related to the reference blade "0" and with  $a_n$  the individual blade displacement. The left-hand side of Equation 2.6 represents the aerodynamic parameter when all blades of the blade-row vibrate with a phase lag of  $\phi_n$ . Equation 2.6 can be simplified considering the traveling-wave mode technique, since in this case constant blade vibration amplitudes are present. Additionally, the phase lag  $\phi_n$  can be represented by the inter-blade phase angle and the distance between the  $n$ -th influence coefficient and the reference blade 0. Hence it can be stated that:

$$a_n = a_0 \quad \text{and} \quad \phi_n = \sigma_\lambda n \quad (2.7)$$

Therefore Equation 2.6 reduces to:

$$\tilde{c}_{TW}^{\sigma_\lambda} = \sum_{n=0}^{N-1} \tilde{c}_{IC}^{n,0} e^{-i\sigma_\lambda n} \quad (2.8)$$

with  $\tilde{c}_{TW}^{\sigma_\lambda}$  being the traveling-wave coefficient for an inter-blade phase angle  $\sigma_\lambda$ . Vice versa for calculating the influence coefficients at least as many linear independent equations have to be available as vibrating blades are present in the cascade. This is commonly achieved by measuring all possible traveling-wave modes given by the inter-blade phase angles. This formulation can be written as:

$$\tilde{c}_{IC}^{n,0} = \frac{1}{N} \sum_{\lambda=0}^{N-1} \tilde{c}_{TW}^{\sigma_\lambda} e^{i\sigma_\lambda n} \quad (2.9)$$

Next, the summation of Equation 2.8 shall be visualized on the basis of an example in Figure 2.3. For this, an inter-blade phase angle of  $\sigma_{\lambda=1} = 18^\circ$  is chosen, which is the minimum inter-blade phase angle for a cascade composed by 20 blades as in this case. Hence Equation 2.8 results in:

$$\begin{aligned} \tilde{c}_{TW}^{\sigma_{\lambda=1}=18^\circ} = & \tilde{c}_{IC}^{0,0} + \tilde{c}_{IC}^{1,0} e^{-i18^\circ} + \tilde{c}_{IC}^{2,0} e^{-i18^\circ 2} + \tilde{c}_{IC}^{3,0} e^{-i18^\circ 3} + \dots + \\ & \tilde{c}_{IC}^{(N-3),0} e^{-i18^\circ (N-3)} + \tilde{c}_{IC}^{(N-2),0} e^{-i18^\circ (N-2)} + \tilde{c}_{IC}^{(N-1),0} e^{-i18^\circ (N-1)} \end{aligned} \quad (2.10)$$

Since the summation in Equation 2.8 depends on two variables which are related by the summation variable  $n$  over all blades, a tabular form is chosen for visualization, as presented in Figure 2.3. Along the horizontal direction the phase lag of the  $n$ -th blade to the reference blade 0 is noted. This is performed in steps which relate to the smallest possible inter-blade

### 2.3. Aerodynamic Influence Coefficient Formulation

phase angle of the blade-row ( $\sigma_{\lambda=1} = 18^\circ$ ). Along the vertical direction, the influence coefficients  $\tilde{c}_{IC}^{n,0}$  of all blades are displayed. Considering the aforementioned example ( $\sigma_{\lambda=1} = 18^\circ$ ) influence coefficient  $n = 0$  acts on itself, hence the phase lag must be  $\sigma_{\lambda=1} n = 0^\circ$  indicated by the orange box. Both values (vertical and horizontal) are multiplied and this continues with the next influence coefficient. For the neighboring blades,  $n = 1$  and  $n = 2$ , a phase lag of  $\sigma_{\lambda=1} n = 18^\circ$  and respectively  $\sigma_{\lambda=1} n = 36^\circ$  have to be considered. By multiplying the connected horizontal and vertical terms and adding the result to the previous one, the summation can be continued. This visualization can be simply adopted to include the blade vibration amplitudes by noting them in the filled-in boxes. The advantage of this visualization becomes clear when using it the other way round. Hence the combination of influence coefficient and any arbitrary combination of phase lag and amplitude can easily be identified, for example of an individual cluster-blade in a cluster.

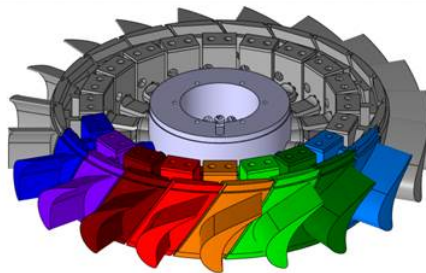
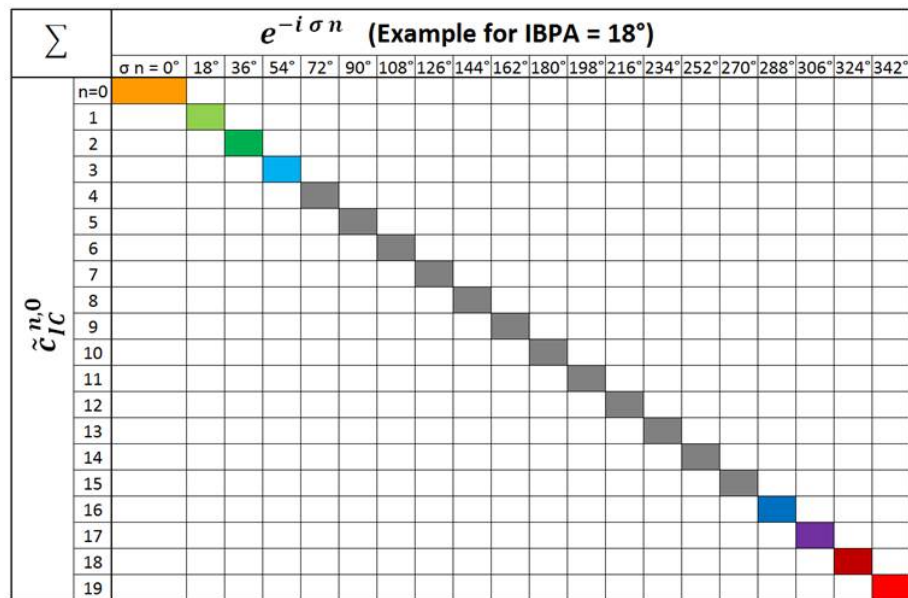


**Figure 2.3:** General processing procedure from the influence coefficient to the single-blade traveling-wave formulation. This example represents the case to determine the traveling-wave coefficient  $\tilde{c}_{TW}^{\sigma_{\lambda=1}=18^\circ}$  for an inter-blade phase angle of  $\sigma_{\lambda=1} = 18^\circ$  based on influence coefficients.

## Theoretical Concept

In the literature, several different descriptions of the equations shown above can be found, for example in Schläfli [1989], Försching [1994] and Vogt [2005]. As indicated in Equation 2.8 and in Figure 2.3, the inter-blade phase angle has a major influence on the outcome when superimposing the influence coefficients. How this effects the results is illustrated in Figure 2.4. In all four graphs, the influence coefficients (colored arrows) of blade 0 (orange) and its neighboring blades -1 (red) and +1 (green) are displayed as complex vectors. The length of each vector represents the magnitude and the orientation by the phase-angle with respect to the blade motion. Hence the real part displays the pressure or force which is in phase with the actual vibrating blade (not the traveling-wave reference blade). The imaginary part displays the ratio which is leading in phase by  $90^\circ$  the vibrating blade. Superimposing these three example blades (orange- and dashed-arrows), while considering the respective inter-blade phase angle, the pressure or force vector for the traveling-wave reference blade can be determined. In the example of Figure 2.4, the inter-blade phase angles of  $\sigma_\lambda = 0^\circ$  (top left),  $\sigma_\lambda = 90^\circ$  (top right),  $\sigma_\lambda = 180^\circ$  (bottom left) and  $\sigma_\lambda = 270^\circ$  ( $-90^\circ$ ) (bottom right) are displayed. The real part of the superimposed vector represents the pressure or force which is in phase with the traveling-wave reference blade. The imaginary part displays the ratio which is leading in phase by  $90^\circ$  the traveling-wave reference blade.

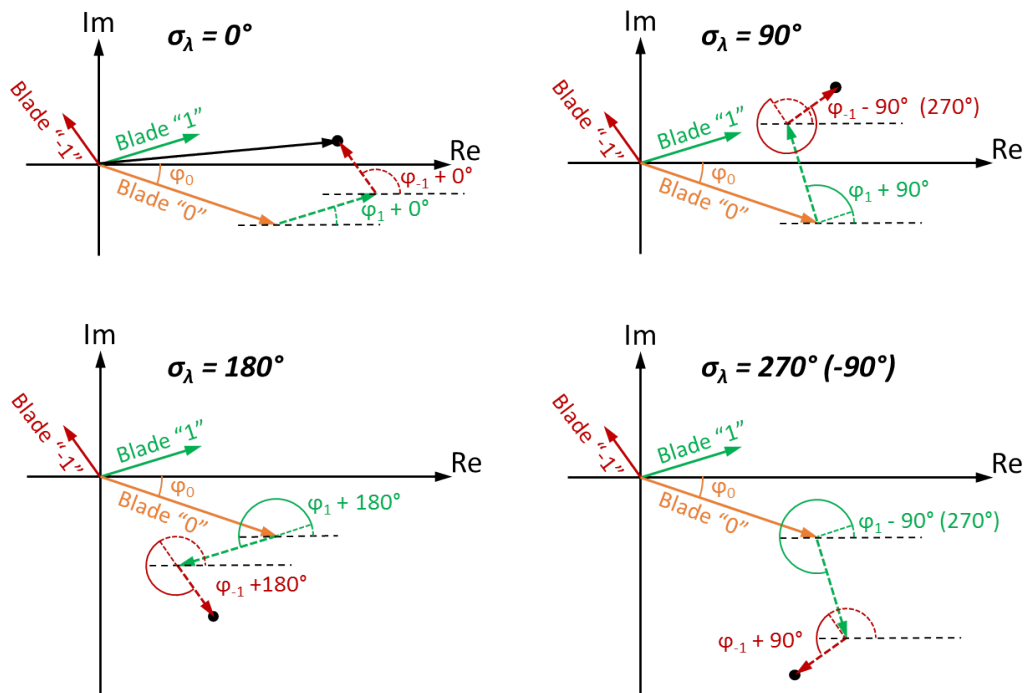


**Figure 2.4:** Effect of the inter-blade phase angle on the traveling-wave mode response; superposition of influence coefficients of blades -1, 0 and +1 for inter-blade phase angles  $\sigma_\lambda = 0^\circ$  (top left),  $\sigma_\lambda = 90^\circ$  (top right),  $\sigma_\lambda = 180^\circ$  (bottom left),  $\sigma_\lambda = 270^\circ$  ( $-90^\circ$ , bottom right).

Considering all possible inter-blade phase angles, the pointer of the superimposed traveling-wave vector creates a closed curved line (see Figure 2.5 on the left). By definition, the negative



### 2.3. Aerodynamic Influence Coefficient Formulation

imaginary part of this curved line is the representative of the aerodynamic damping (see Equations 2.31 and 2.32 and compare to Figure 2.5). Furthermore, the center of the curved line is given by the vector representing the self-induced influence coefficient (blade 0, orange).

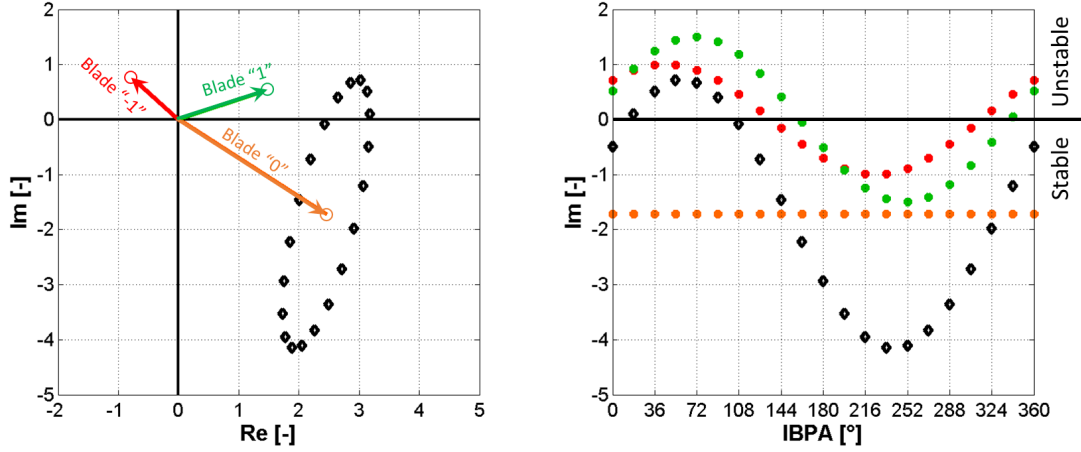


**Figure 2.5:** On the left: locus of the influence coefficient superposition (black dots) for all inter-blade phase angles. On the right: imaginary part of the superposition (black dots) and the influence coefficients of blades -1 (red dots), 0 (orange dots) and +1 (green dots).

When calculating the influence coefficients for all blades of the cascade, as stated in Equation 2.9, a cyclic influence coefficient matrix can be determined (see the matrix in Equation 2.11, for better visibility the subscript has been omitted). The mathematics involved in calculating this matrix can be consulted in Crawley [1988] or in Försching [1994]. Thanks to its cyclic notation this matrix enables to identify how an individual blade influences any other blade in the cascade. For example, if one is interested in how the motion of the second blade influences the first blade, the term in the first column and second row has to be considered ( $c^{1,0}$ ). Taking into account the symmetry of the cascade due to geometric identical blades, this must be the same as the influence of the motion of the third blade on the second, noted in the matrix in the third row and second column. Therefore it can be deduced that the terms in the diagonal contain the influences resulting from the blade's own motion.

$$[C_{IC}] = \begin{bmatrix} c^{0,0} & c^{N-1,0} & c^{N-2,0} & \dots & c^{1,0} \\ c^{1,0} & c^{0,0} & c^{N-1,0} & \dots & c^{2,0} \\ c^{2,0} & c^{1,0} & c^{0,0} & \dots & c^{3,0} \\ \vdots & \vdots & \vdots & \ddots & \vdots \\ c^{N-1,0} & c^{N-2,0} & c^{N-3,0} & \dots & c^{0,0} \end{bmatrix} \quad (2.11)$$



## 2.4 Special Cluster Approach of the Aerodynamic Influence Coefficient Formulation

In the present work, an approach is made to use the traveling-wave aerodynamic data of the single-blade test cases to reproduce the individual cluster-blades of the experimentally investigated clusters. A similar approach was introduced by Whitehead and Evans [1992] to numerically simulate clusters and this approach was also used by Kahl [1995] and Chernysheva [2004]. In order to employ this approach two steps are necessary. First, the influence coefficients of the single-blade test cases are determined using Equation 2.9. Second, the kinematics of the individual cluster-blades are considered in relation to the previously determined single-blade influence coefficients. The formulation of Equation 2.6 is adjusted in order to account for the individual cluster kinematics and is written as:

$$\tilde{c}_{C,I,TW} = \sum_{n=0}^{N-1} \tilde{c}_{SB,IC}^{n,0} a_{C,I}^{n,0} e^{-i\sigma_{C,I}^{n,0}} \quad (2.12)$$

In the above equation,  $\tilde{c}_{C,I,TW}$  represents the cluster traveling-wave coefficient of the zeroth cluster-blade  $I$  in the reference (zeroth) cluster. It shall be noted that “zeroth” relates to the relation between traveling-wave and influence coefficient formulations, which is applied for the individual cluster-blades  $I$ . The variable  $\tilde{c}_{SB,IC}^{n,0}$  represents the  $n$ -th single-blade influence coefficient related to the reference blade in the influence coefficient formulation (Equation 2.9). The amplitude kinematic of the cluster is introduced by the non-dimensional factor  $a_{C,I}^{n,0}$ . The subscript index  $C$  indicates the relation to the cluster and the subscript  $I$  denotes the zeroth cluster-blade in the reference cluster. The superscript index represents with  $n,0$  the relation to the  $n$ -th single-blade influence coefficient  $\tilde{c}_{SB,IC}^{n,0}$  as well as the relation of the  $n$ -th cluster-blade amplitude kinematic to the zeroth cluster-blade  $I$ . The phase kinematic of the cluster is described by  $\sigma_{C,I}^{n,0}$ . The sub- and super-script indices denote the same relationships as for the previous variable  $a_{C,I}^{n,0}$  describing the amplitude kinematic of the cluster.

Next, a cluster of four blades is used as an example to described the above-mentioned approach. The cluster represents a vane-package of four blades performing a torsional oscillation. As previously noted in the presented approach, the individual cluster-blade traveling-wave coefficient is calculated by superimposing the single-blade influence coefficients. Thus, it is necessary to define the kinematics of the individual cluster-blades as they would be single-blades oscillating as a cluster configuration. Assuming for the moment, each single-blade oscillates in an axial-bending oscillation direction with the same blade vibration frequency, the kinematics of the individual cluster-blades (A, B, C and D) can be defined as follows:

- Cluster-blades A and B are oscillating in-phase.
- Cluster-blades C and D are oscillating in-phase and in opposite phase to cluster-blades A and B.
- The blade vibration amplitude of cluster-blades B and C is a third of the nominal blade vibration amplitude of cluster-blades A and D.

Theoretical Concept

**Cluster blade A**

$e^{-i\sigma_{C,l}^{n,0}}$  (Example for ICPA = 72°)

$\Sigma$		$e^{-i\sigma_{C,l}^{n,0}}$ (Example for ICPA = 72°)																				
		$\sigma_{C,l}^{n,0} = 0^\circ$	18°	36°	54°	72°	90°	108°	126°	144°	162°	180°	198°	216°	234°	252°	270°	288°	306°	324°	342°	
$\tilde{C}_{SB,IC}^{n,0}$	n=0	A	a																			
	1	B	a/3																			
	2																					
	3																					
	4																					
	5																					
	6																					
	7																					
	8																					
	9																					
	10																					
	11																					
	12																					
	13																					
	14																					
	15																					
	16																					
	17																					
	18																					
19																						

**Cluster blade C**

$e^{-i\sigma_{C,l}^{n,0}}$  (Example for ICPA = 72°)

$\Sigma$		$e^{-i\sigma_{C,l}^{n,0}}$ (Example for ICPA = 72°)																				
		$\sigma_{C,l}^{n,0} = 0^\circ$	18°	36°	54°	72°	90°	108°	126°	144°	162°	180°	198°	216°	234°	252°	270°	288°	306°	324°	342°	
$\tilde{C}_{SB,IC}^{n,0}$	n=0																					
	1																					
	2																					
	3																					
	4																					
	5																					
	6																					
	7																					
	8																					
	9																					
	10																					
	11																					
	12																					
	13																					
	14																					
	15																					
	16																					
	17																					
	18																					
19																						

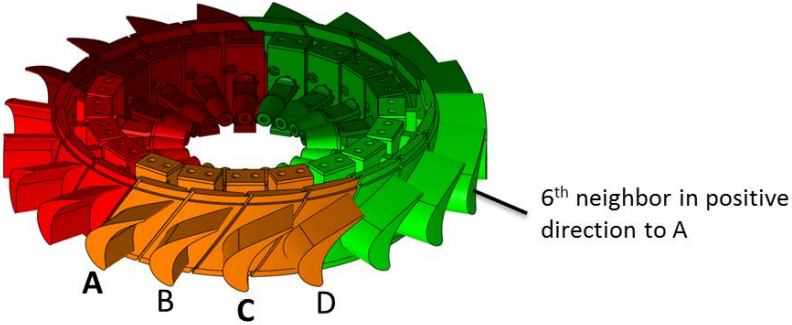


**Figure 2.6:** Specific processing procedure from influence coefficients to cluster-blade traveling-wave coefficients for an inter-cluster phase angle of  $\Gamma_{\lambda=1} = 72^\circ$ . Top: cluster-blade A, bottom: cluster-blade C.

## 2.4. Special Cluster Approach of the Aerodynamic Influence Coefficient Formulation

For this example, the traveling-wave coefficients for cluster-blades A and C are superimposed for an inter-cluster phase angle of  $\Gamma_{\lambda=1} = 72^\circ$ . In Figure 2.6, the amplitude and phase kinematics ( $a_{C,I}^{n,0}$ ,  $\sigma_{C,I}^{n,0}$ ) of Equation 2.12 are displayed, with the visualization procedure previously introduced for the single-blade case only (see Figure 2.3). Cluster-blade A is presented at the top left in Figure 2.6 and cluster-blade C at the bottom left. In order to reproduce a specific cluster-blade  $I$  in the cluster, the individual cluster-blade  $I$  has to be set on the zeroth position ( $n = 0$ ) and the other cluster-blades have to be referred to it. As an example the sixth neighboring blade in the pressure-side direction to the zeroth blade is used. It represents the third cluster-blade in the direct neighboring cluster. Hence, the vibration amplitude must be a third of the nominal vibration amplitude. With respect to the phase lag, the blade is positioned in the direct neighboring cluster, which means a phase lag of  $\Gamma_{\lambda=1} = 72^\circ$  has to be considered. Additionally, the blade is oscillating in counter-phase to the zeroth cluster-blade thus a phase lag of  $180^\circ$  must be added. In Table 2.1 the relation of the amplitude and phase kinematics ( $a_{C,I}^{n,0}$ ,  $\sigma_{C,I}^{n,0}$ ) of Equation 2.12 are stated for all four-cluster-blades.

SB IC index:	Cluster-blade A:		Cluster-blade B:		Cluster-blade C:		Cluster-blade D:	
$n$	$a_{C,A}^{n,0}$	$\sigma_{C,A}^{n,0}$	$a_{C,B}^{n,0}$	$\sigma_{C,B}^{n,0}$	$a_{C,C}^{n,0}$	$\sigma_{C,C}^{n,0}$	$a_{C,D}^{n,0}$	$\sigma_{C,D}^{n,0}$
0	1	$0^\circ$	1/3	$0^\circ$	1/3	$180^\circ$	1	$180^\circ$
1	1/3	$0^\circ$	1/3	$180^\circ$	1	$180^\circ$	1	$\Gamma_1$
2	1/3	$180^\circ$	1	$180^\circ$	1	$\Gamma_1$	1/3	$\Gamma_1$
3	1	$180^\circ$	1	$\Gamma_1$	1/3	$\Gamma_1$	1/3	$\Gamma_1 + 180^\circ$
4	1	$\Gamma_{\lambda=1}$	1/3	$\Gamma_1$	1/3	$\Gamma_1 + 180^\circ$	1	$\Gamma_1 + 180^\circ$
5	1/3	$\Gamma_{\lambda=1}$	1/3	$\Gamma_1 + 180^\circ$	1	$\Gamma_1 + 180^\circ$	1	$\Gamma_2$
6	1/3	$\Gamma_1 + 180^\circ$	1	$\Gamma_1 + 180^\circ$	1	$\Gamma_2$	1/3	$\Gamma_2$
$\vdots$	$\vdots$	$\vdots$	$\vdots$	$\vdots$	$\vdots$	$\vdots$	$\vdots$	$\vdots$
16	1	$\Gamma_{J-1}$	1/3	$\Gamma_{J-1}$	1/3	$\Gamma_{J-1} + 180^\circ$	1	$\Gamma_{J-1} + 180^\circ$
N-3	1/3	$\Gamma_{J-1}$	1/3	$\Gamma_{J-1} + 180^\circ$	1	$\Gamma_{J-1} + 180^\circ$	1	0
N-2	1/3	$\Gamma_{J-1} + 180^\circ$	1	$\Gamma_{J-1} + 180^\circ$	1	0	1/3	0
N-1	1	$\Gamma_{J-1} + 180^\circ$	1	0	1/3	0	1/3	$180^\circ$

**Table 2.1:** Kinematic relation between the single-blade influence coefficient terms and the cluster traveling-wave terms of a four-blade cluster oscillating in torsional motion.

## 2.5 Aerodynamic Stability

The aerodynamic interaction between the blade vibration and the fluid flow can be determined by the motion induced unsteady pressure on the blade surface and the blade motion. The unsteady pressure results in a force acting on the blade and either supports the blade motion, which results in an excitation, or counteracts and damps the blade motion. In the latter case, aerodynamic (flutter) stability is present. In order to determine whether an excitation or a damping is present, the work per cycle exerted by the fluid on the structure is calculated.

As stated, next to single-blade test cases, cluster test cases are investigated with respect to their aerodynamic stability. The formulations outlined in the following consider one blade as a basis and are also used for cluster configurations. This is applicable, since each of the cluster-blades is investigated as an individual blade. Additionally a two-dimensional turbine-blade is considered. As no deformation of the blade profile is present, it can be treated as a rigid body. The principal formulations are noted in the following. For a detailed mathematical development, Verdon [1987] is an effective starting point. He showed that in the case of small perturbations the following simplifications can be applied:

- The blade oscillations are of a harmonic nature.
- For small vibration amplitudes, the unsteady pressures can be linearly superimposed.
- The eigen-modes of the individual blades are not coupled.

These assumptions are in line with the approach known as the “Energy Method” which was introduced by Carta [1967]. Considering a harmonic blade motion, the blade displacement vibration can be described as follows:

$$\vec{a}_n(t) = \hat{a} \cos(2\pi f t - n \sigma_\lambda) \quad n \in \mathbb{N}, \lambda \in \mathbb{N}, \mathbb{N} = \{0 \dots N - 1\} \quad (2.13)$$

where  $t$  describes the time,  $f$  the vibration frequency of the blade,  $n$  the blade number with  $n = 0$  as the reference blade,  $\sigma_\lambda$  the inter-blade phase angle and  $\hat{a}$  the non-dimensional displacement vector of the blade at one radial position. In the case of a torsional movement,  $\hat{a}$  is defined as:

$$\hat{a} = \hat{a}_\alpha = \alpha \vec{e}_\alpha \quad (2.14)$$

with  $\alpha$  describing the blade angular displacement in radians and with  $\vec{e}_\alpha$  as the unit vector parallel to the torsion axis. In the case of a bending movement,  $\hat{a}$  is defined as:

$$\hat{a} = \hat{a}_h = \frac{h}{c} \vec{e}_h \quad (2.15)$$

with  $h$  describing the blade bending displacement in the vibration direction, described by the vector  $\vec{e}_h$ , and  $c$  representing the blade chord length. Based on the harmonic blade motion, the

pressure acting on the blade surface can be described as a sum of the steady mean pressure  $p_{steady}$  and the time-varying unsteady pressure fluctuations  $\tilde{p}(t)$  around this mean value. By calculating the Fourier transformation of the time-varying unsteady pressure fluctuations  $\tilde{p}(t)$  and cross-correlating it with the harmonic blade motion, the pressure amplitude  $\hat{p}_s$  (modulus) and phase lag  $\varphi_s$  along the blade surface  $s$  can be determined. Hence the time-varying unsteady pressure  $\tilde{p}_s(t)$  can be noted in complex form as:

$$\tilde{p}_s(t) = \hat{p}_s e^{i\varphi_s} e^{i(2\pi ft - n\sigma_\lambda)} \quad \tilde{p}_s(t) \in \mathbb{C} \quad (2.16)$$

Considering that the phase lag between unsteady pressure and blade motion is calculated so that it relates to the same blade ( $n = 0$ ), Equation 2.16 can be simplified to:

$$\tilde{p}_s(t) = \hat{p}_s e^{i\varphi_s} e^{i(2\pi ft)} \quad \tilde{p}_s(t) \in \mathbb{C} \quad (2.17)$$

The unsteady aerodynamic force  $\vec{F}(t)$  acting on the discretized blade surface element can be expressed as:

$$d\vec{F}(t) = b p_s(t) \vec{n}_s(t) ds \quad (2.18)$$

with  $\vec{n}_s(t)$  as the direction of the outward normal unit vector,  $b$  the blade span width and  $ds$  as the surface element. These variables are depicted on the left of Figure 2.7. By calculating the spatial integral of Equation 2.18 the aerodynamic force can be determined:

$$\vec{F}(t) = b \oint_s p_s(t) \vec{n}_s(t) ds \quad (2.19)$$

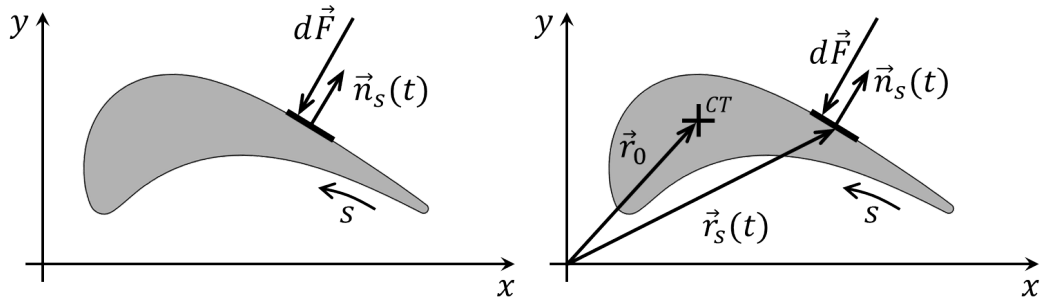


**Figure 2.7:** Determination of the aerodynamic force (left) and moment (right) coefficients.

For convenience, the values describing the aerodynamic stability are depicted in a non-dimensional form. Hence the unsteady pressure amplitude is normalized by a reference dynamic head and the blade vibration amplitude. This results in the unsteady pressure coefficient which is defined as:

$$\tilde{c}_{p,s}(t) = \frac{\tilde{p}_s(t)}{|\hat{a}| (p_{t1} - p_{stat1})} \quad (2.20)$$

## Theoretical Concept

---

with  $|\hat{a}|$  the non-dimensional blade displacement (Equation 2.13),  $p_{tl}$  the total pressure and  $p_{stat}$  the static pressure at the inlet. The subscript  $s$  denotes the non-dimensional curvilinear coordinate which is calculated as follows:

$$s = \frac{\mathfrak{s}}{c} \quad (2.21)$$

with  $c$  representing the blade chord. Taking into account the normalization of the unsteady pressure amplitude (Equation 2.20) and the non-dimensional curvilinear coordinate (Equation 2.21), the unsteady force coefficient vector can be formulated as:

$$\tilde{c}_F = \oint_s \tilde{c}_{p,s}(t) \vec{n}_s(t) ds \quad (2.22)$$

For the torsional motion, the unsteady moment coefficient vector is defined according to the definitions in Figure 2.7 (on the right) and considering Equation 2.20. It reads:

$$\tilde{c}_M = \oint_s \tilde{c}_{p,s}(t) \left[ \frac{(\vec{r}_s(t) - \vec{r}_0)}{c} \times \vec{n}_s(t) \right] ds \quad (2.23)$$

where  $\vec{n}_s$  is the outward normal unit vector and  $(\vec{r}_s(t) - \vec{r}_0)$  is the vector between the center of rotation and the location on the blade surface.

The work coefficient is next introduced and describes the dimensionless work performed per unit arc length by the fluid on the blade. This parameter is used in two ways: as “local” (referring to a specific position on the blade surface defined by the non-dimensional curvilinear blade coordinate  $s$ ) and “global” (referring to the entire surface of the two-dimensional blade). Thus, local changes can be identified more precisely along the blade surface between the test cases, whereas the global view describes the aerodynamic stability of the blade. In the case of a bending motion, the local work coefficient can be described as:

$$w_{F,s} = \int_0^T \tilde{c}_{p,s}(t) \vec{n}_s(t) \dot{\vec{a}}_h(t) dt \quad (2.24)$$

where  $\dot{\vec{a}}_h(t)$  is the first derivative of Equation 2.13 taking into account the bending vibration direction. For the torsional motion, the local unsteady work coefficient is defined as:

$$w_{M,s} = \int_0^T \tilde{c}_{p,s}(t) \left[ \frac{(\vec{r}_s(t) - \vec{r}_0)}{c} \times \vec{n}_s(t) \right] \dot{\vec{a}}_\alpha(t) dt \quad (2.25)$$

where  $\dot{\vec{a}}_\alpha(t)$  is the first derivative of Equation 2.13 taking into account the torsional vibration direction. In the case of a destabilizing pressure contribution to the blade vibration, the local work coefficient is positive, hence indicating flow areas where the flow transfers energy to the blade. This phenomenon reinforces the vibration. Negative values indicate regions where the



pressure contributes to the stabilization of the vibration. Blade vibration energy is therefore absorbed by the flow.

The global aerodynamic work coefficient can be calculated by integrating Equations 2.24 and 2.25 over the entire blade surface. Hence it can be stated in the case of a bending motion that:

$$W_F = \int_0^T \left[ \oint_s \tilde{c}_{p,s}(t) \vec{n}_s(t) ds \right] \dot{\vec{a}}_h(t) dt \quad (2.26)$$

Accordingly, in the case of a torsional motion the global aerodynamic work coefficient is:

$$W_M = \int_0^T \left[ \oint_s \tilde{c}_{p,s}(t) \left[ \frac{(\vec{r}_s(t) - \vec{r}_0)}{c} \times \vec{n}_s(t) \right] ds \right] \dot{\vec{a}}_\alpha(t) dt \quad (2.27)$$

As highlighted before, the sign of the work coefficient describes whether the blade motion is either stabilized or excited by the unsteady flow. Reflecting the equations used to define the work coefficient, it can be stated that the phase lag  $\varphi_s$  between the unsteady pressure and the blade motion (Equation 2.16) is the key parameter for the sign. In order to avoid any sign errors of the work coefficient, it is essential to ensure that the phase lag  $\varphi_s$  is always cross-correlated between the unsteady pressure and the blade motion on which the unsteady pressure is evaluated. This is essential for evaluating individual cluster-blades since it implicitly accounts for the phase lag between the individual cluster-blade motions.

Finally, in order to describe the aerodynamic stability of the blade, a normalized parameter  $\Xi$  is commonly used. This parameter, as reported by Verdon [1987], normalizes the negated work coefficient by the blade vibration amplitude  $\hat{a}$  and  $\pi$ . It can be written as:

$$\Xi = -\frac{W}{\pi |\hat{a}|} \quad (2.28)$$

Thus in case of bending motion it is defined as:

$$\Xi_F = -\frac{W_F}{\pi |\hat{a}_h|} \quad (2.29)$$

and in case of torsional motion as:

$$\Xi_M = -\frac{W_M}{\pi |\hat{a}_\alpha|} \quad (2.30)$$

Bearing in mind that the key parameter to determining the aerodynamic stability is based on the phase lag  $\varphi_s$ , it can be also calculated in the case of bending motion as the negative imaginary part of the unsteady force coefficient (Equation 2.22):

$$\Xi_F = -Im[\tilde{\vec{c}}_F \cdot \vec{e}_h] \quad (2.31)$$

## Theoretical Concept

where  $\vec{e}_h$  is the blade oscillation direction unit vector and  $\tilde{c}_F$  is the complex unsteady force coefficient (Equation 2.23). Accordingly for the torsional motion, it can be written as:

$$\Xi_M = -Im[\tilde{c}_M \cdot \vec{e}_\alpha] \quad (2.32)$$

where  $\vec{e}_\alpha$  is the unit vector parallel to the torsion axis and  $\tilde{c}_M$  is the complex unsteady moment coefficient (Equation 2.23). In the case of a positive value, the blade is damped and leads to a stable behaviour. In contrast, the blade is excited in its oscillations and an unstable behaviour is present.

In the field of turbomachinery, the reduced frequency is a measure to indicate the likelihood of starting flutter. As Vogt [2005] described, the reduced frequency is a relation between the time the air flow needs from LE to TE and the duration of one vibration cycle (see Figure 2.8). Hence, it can be interpreted as the ability of the flow adapting to the blade vibration and is commonly defined in the following way:

$$k = \frac{\pi c f_{bl}}{U_2} = \frac{\pi c}{U_2 \Delta t_{bl}} \quad (2.33)$$

where  $f_{bl}$  is the blade vibration frequency,  $c$  the blade chord length,  $\Delta t_{bl}$  the blade oscillation period and  $U_2$  the outlet velocity. For low reduced frequencies, a quasi-steady character of the flow is present, since the flow is able to settle to the changed conditions. Therefore, the smaller the reduced frequency the higher the susceptibility for flutter. Critical reduced frequencies of turbine-blades are reported (Vogt [2005]) to be situated between 0.1 and 1.1. At this point it has to be noted that these aforementioned values are purely empirical and thus have to be applied with care. The test cases within this work have a reduced frequency of  $k = 0.26$ . Schläfli [1989] reported that non-vibrating single-blade profiles with identical reduced frequency and Mach number show similar unsteady behaviour in incompressible flows. With respect to test cases investigating a cascade of oscillating blades not only does the reduced frequency have to be similar, but also the traveling-wave pattern of the whole cascade. This in order to account for the influences of the vibrating neighboring blades with respect to the investigated blade.

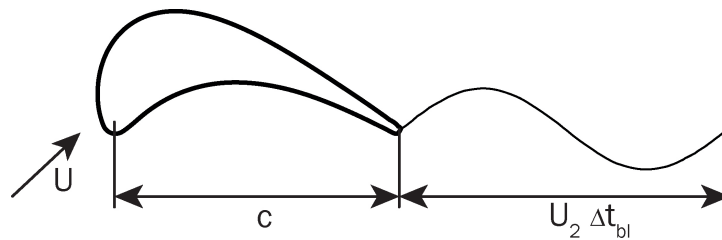


**Figure 2.8:** Illustration of the reduced frequency.

## 3 Experimental Setup

ALL experiments dedicated to this investigation were performed in the non-rotating annular test facility at EPFL. The performed measurements were part of the research project FUTURE (Flutter Free Turbomachinery), funded by the European commission as part of the FP7. Further information about the project details are available on the Website of the project FUTURE [2008]. The test rig, the annular cascade, the measurement techniques and the test cases are presented in this chapter.

### 3.1 Non-Rotating Annular Test Facility

For decades, the non-rotating annular test facility at EPFL, developed by Bölcs [1983], has been dedicated to the investigation of aerodynamic and aeroelastic phenomena of turbine and compressor cascades. The unique design of the test facility changes the flow coordinate system in such a way that the air is swirled instead of rotating the rotor. The avoidance of a rotating rotor simplifies the test facility mechanics since, for example, it allows the researcher to easily implement a system to force the airfoils of a complete blade-row into oscillation. Furthermore there is no necessity for bearings and telemetric devices to control the rotor and to perform measurements. The resulting flow conditions are similar to those in real turbomachinery. An extensive instrumentation is therefore possible and the measurement techniques can be simplified due to the less complex environment, thus allowing reliable data acquisition. The test facility was continuously improved by means of measurement techniques and flow control, thus permitting aeroelastic investigations such as forced response, flutter, gust response and structural mistuning. An embedded blade vibration control system allows the test engineer to perform measurements in the traveling-wave mode (all blades in the cascade vibrate) as well as the influence coefficient mode (only one blade in the cascade vibrates). Furthermore, aerodynamic investigations are possible, such as active flow-control and cascades under reverse-flow conditions.

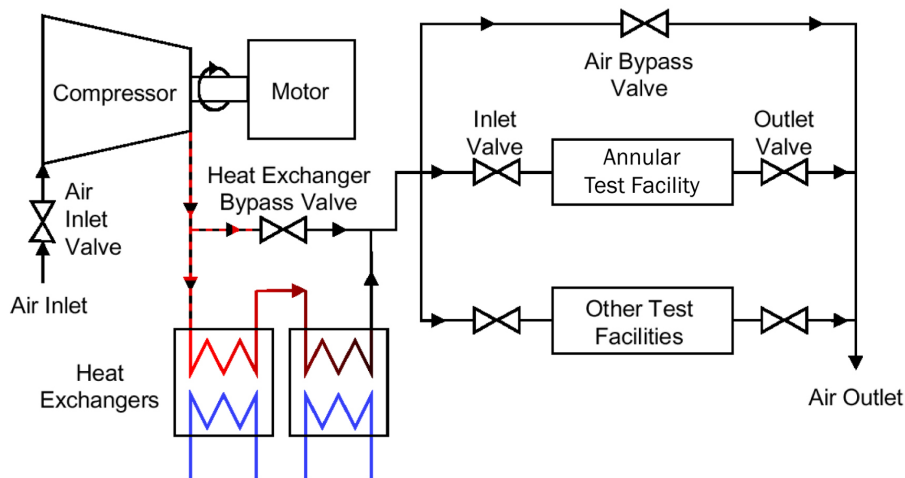
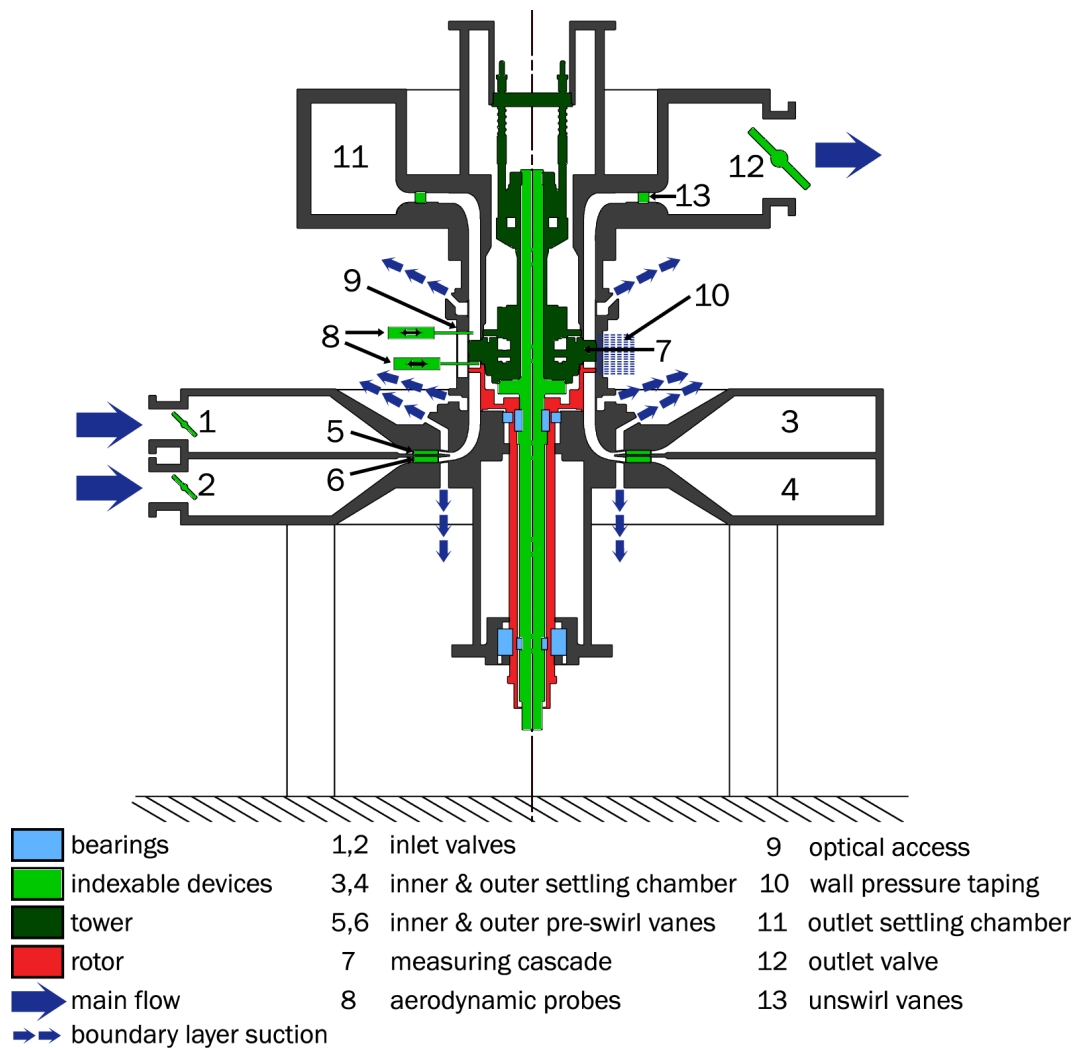


Figure 3.1: EPFL air supply network.

A 2.25 MW four-stage centrifugal compressor supplies the test facility with compressed air in an open loop (see Figure 3.1). The compressor uses air at ambient pressure and temperature. The temperature increases during the compression process and is then cooled by two heat exchangers, thus allowing the air temperature entering the test facility to be adjusted. The entering air temperature can be regulated between 20° and 60° C. The air outlet pressure of the compressor is adjusted by the air inlet valve, so that a compression ratio of 3.5 with a maximum flow rate of 10 kg/s can be achieved.



**Figure 3.2:** Schematic view of the non-rotating annular test facility, Bölcs [1983].

Figure 3.2 presents the test facility and details its main functions (for further information consult Bölcs [1983]). The air enters the test facility radially (Figure 3.2, item 1 and 2) and is pre-swirled by vanes (Figure 3.2, item 5 and 6) before accelerating in the radial-axial nozzle. After acceleration, the flow approaches the test section (Figure 3.2, item 7). Behind the test section, the flow turns in a radial direction and exits (Figure 3.2, item 12) the test facility. With this setup, a quasi-two-dimensional flow at mid-channel height in the test section can be achieved. The flow quantities (total pressure, outlet static pressure and inlet flow angle) can be adjusted by the inlet valves (Figure 3.2, items 1 and 2), outlet valves (Figure 3.2, item 12) and the pre-swirl vanes (Figure 3.2, items 5 and 6). If necessary, adjustments to the flow boundary layer can be performed using the boundary layer suction valves, located after the inlet pre-swirl vanes (Figure 3.2, items 5 and 6) and up- and downstream of the test section (Figure 3.2, item 7).

## Experimental Setup

Different measuring systems are used to identify the steady-state flow conditions at different positions in the test section (Figure 3.2, item 7). Entering the test facility at the upstream settling chamber (Figure 3.2, items 3 and 4), the total temperature of the flow is measured using a thermostat. Next, before and after the test section, aerodynamic 5-hole L-shaped probes (Figure 3.2, item 8) are used to measure the in- and outflow profiles. Additionally, along the test section tip wall (Figure 3.2, item 10) an array of pressure taps is used to identify the flow behaviour along the blade tip-gap.

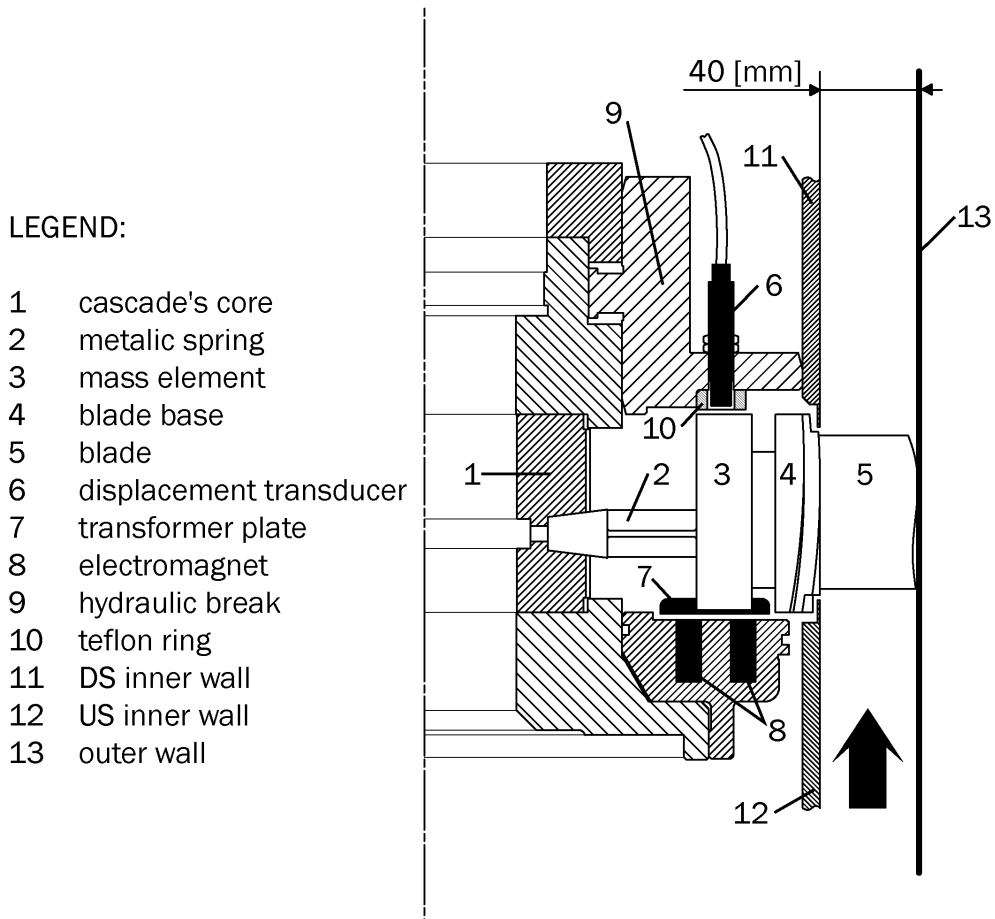


**Figure 3.3:** Detailed schematic view of the test facility (from Rottmeier [2003]).

For controlled vibration measurements, the test facility can be equipped with a magnetic excitation system, which excites the cascade's blades into vibration. The harmonic oscillation of each blade can be individually varied in amplitude and phase with an identical vibration frequency for all blades. Figure 3.3 shows the major parts of the excitation system, the displacement transducers to measure the oscillatory location of the blade (item 6), the electromagnets (item 8) and the transformer plates (item 6) used to create the magnetic force to move the blades. The cascade vibration system is further detailed in Section 3.3.

## 3.2 Annular Turbine Cascade

The annular turbine cascade consists of 20 prismatic turbine-blades (Figure 3.4, bottom right). The blade profile used is identical to the one used during the Brite-Euram ADTurB I (see Rottmeier [2003]) and ADTurB II (see Beretta [2006]) projects. In the frame of both projects the investigations which were performed in the non-rotating annular test facility focused on the influence of gust response to the aerodynamic stability of the turbine-blade. Major dimensions of the annular cascade are noted in Table 3.1. Each of the 20 blades are mounted by a blade-suspension system at the cascade's core (Figure 3.3, item 1). One blade-suspension system itself consists of a blade base (Figure 3.3, item 4), a mass (Figure 3.3, item 3) and a spring (Figure 3.3, item 2). These modular suspension systems can be configured in order to perform vibrations in the bending direction (Figure 3.4, top right) or in the torsion direction (Figure 3.4, middle right). The cross-section of the blade-suspension springs in the torsion mode is cross-shaped, permitting only this type of movement while avoiding all others. For the bending mode beam-shaped suspension springs are applied. The bending blade-suspension system has an additional feature, which enables the direction of vibration to be changed. This feature is realized by a selection of slots for the fitting key between the spring and the mass element of the blade-suspension system (see Figure 3.5), which allows the spring to be rotated relative to the mass element. An additional feature of the blade-suspension system design is that the blade motion is realized only by deforming the spring (Figure 3.3, item 2). Hence the blades (Figure 3.3, item 5) perform a motion as a rigid body.

<b>Number of blades:</b>	$N$	20 [-]
<b>Blade span height:</b>	$b$	40 [mm]
<b>Blade chord:</b>	$c$	75.2 [mm]
<b>Hub radius:</b>	$R_{Hub}$	160 [mm]
<b>Tip radius:</b>	$R_{Tip}$	200 [mm]

**Table 3.1:** Main blade attributes.

In Figure 3.4 on the left, the complete assembly of the turbine test model is presented. The electro-magnetic excitation system (Figure 3.3, item 8) is placed directly below the turbine cascade. Above the turbine cascade module, the hydraulic brake, displacement sensors and wiring/tubing for the various pieces of measurement equipment in the cascade can be identified. These modules of the complete turbine assembly are detailed in the next two sections.



**Figure 3.4:** On the left: turbine cascade assembly with excitation system, measurement equipment, connector support and hydraulic brake. On the top right: one bending blade-suspension system; in the middle right: one torsion blade-suspension system; at the bottom right: turbine cascade.



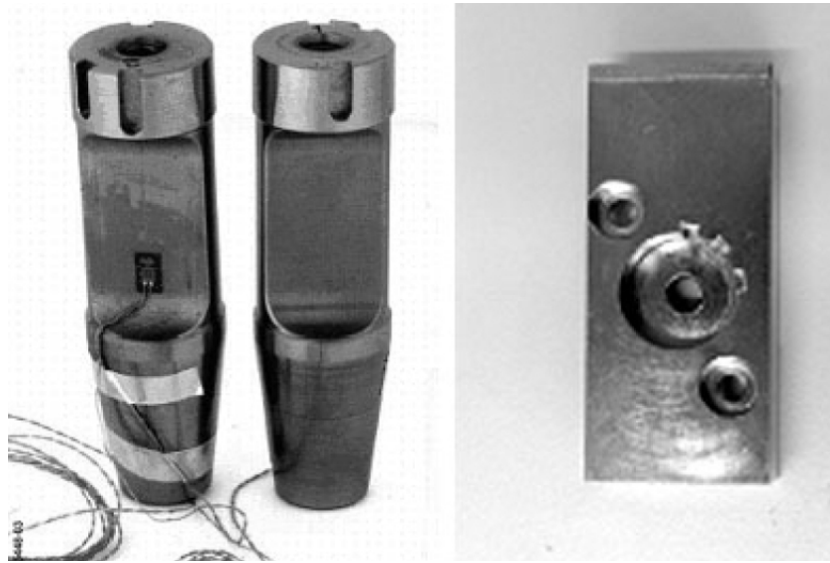


**Figure 3.5:** Additional slots in the spring and mass element for the fitting key, in order to alter the bending direction for the bending blade-suspension system (from Beretta [2006]).

### 3.3 Cascade Vibration Control System

The cascade vibration control system (Figure 3.6) enables the adjustment of the blade vibration amplitudes and phases. The 20 blades are excited by electromagnets (Figure 3.3, item 8) placed below the mass element (Figure 3.3, item 3) of each blade-suspension system. Each of the electromagnets is connected to an amplitude and phase controller. All of these systems are connected to one oscillator creating the reference signal and thus control the excitation frequency of the blade-suspension system. The displacement of the blade is measured continuously via eddy-current displacement sensors and is input to the amplitude and phase controlling system closing the control loop. This system of individually controlled blades, in terms of blade vibration amplitude and phase angle, allows the investigation of the whole set of blade-row vibration patterns (nodal diameters) in the traveling-wave mode. Additionally, measurements can be performed at which only one blade oscillates, as for the influence coefficient formulation. In spite of the advantages of this system, it cannot extract kinetic energy from the vibrating blade-suspension systems and can only transfer kinetic energy into the blade vibration system via the electromagnetic excitation. This can result in the possibility that energy is transferred to the blade vibration system, while the flow conditions also induce a vibrational excitation. Either of the effects can force the system into flutter, which results in the failure of the blade vibration system due to excessive blade vibration amplitudes. In order to avoid exceeding a certain level of vibration amplitude, a hydraulic brake (Figure 3.3, item 9) is positioned above the blade-suspension system. In the case of flutter it can be lowered to stop any blade vibration. Typical vibration frequencies are situated between 150 - 300 Hz, which is the design range of this system. The eigenfrequencies of the investigated blade vibration system structures are in the range of 250 - 280 Hz. The vibration frequency which is finally

## Experimental Setup

used is as close as possible to the eigenfrequency of the structure. This in order to allow the electromagnetic actuation system to excite the blade vibration systems at efficiently large vibration amplitudes. A vibration frequency too close to the eigenfrequency would result in resonance of the blade vibration system and possibly damage it.

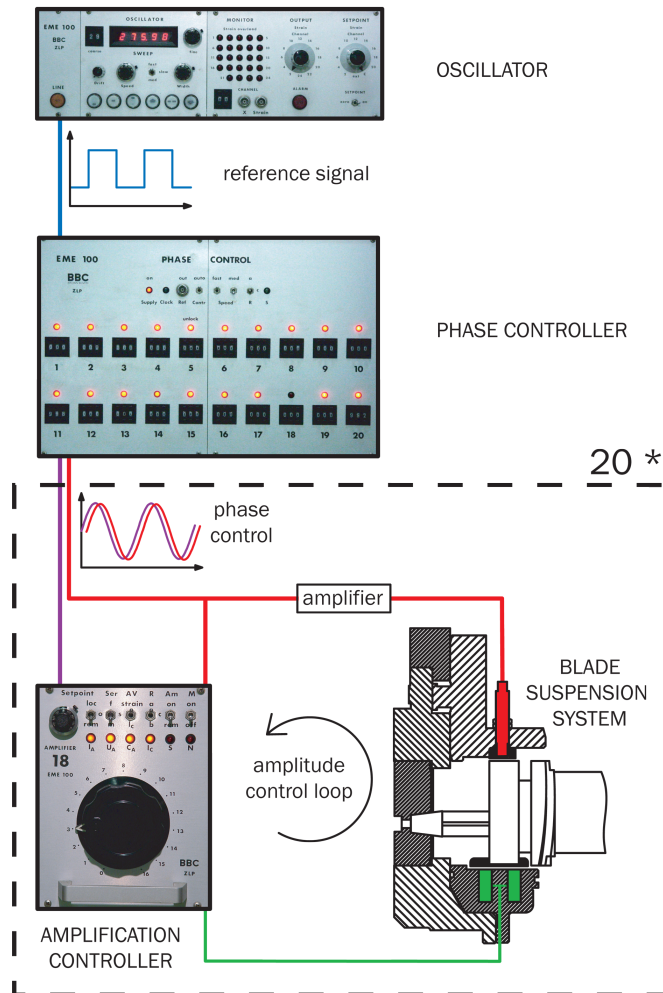


**Figure 3.6:** Cascade vibration control system (from Rottmeier [2003]).

### 3.4 Overview of Cascade Instrumentation

Figure 3.7 presents an overview of the cascade instrumentation. The airfoils of the cascade are equipped in total with four sets of pressure taps. One set is used to measure the unsteady pressures at 50% blade height and the remaining three sets to measure the steady-state blade surface pressure at three different span heights (25%, 50% and 90%). Each of these sets covers one inter-blade channel; that is, blade  $n$  of the inter-blade channel has nine pressure taps on the pressure-side (PS) and blade  $n + 1$  twelve on the suction-side (SS). Figure 3.8 presents the pressure taps along the blade surface; for documentation the pressure-side and suction-side of

### 3.4. Overview of Cascade Instrumentation

the inter-blade channel are depicted onto one blade. Table 3.2 documents the distribution of the pressure taps via the curvilinear coordinate  $s$ . As mentioned in Section 3.3, 20 contactless eddy-current displacement transducers are positioned above each of the blade-suspension masses (Figure 3.3, item 3) to measure time-accurately the displacement of the blades.

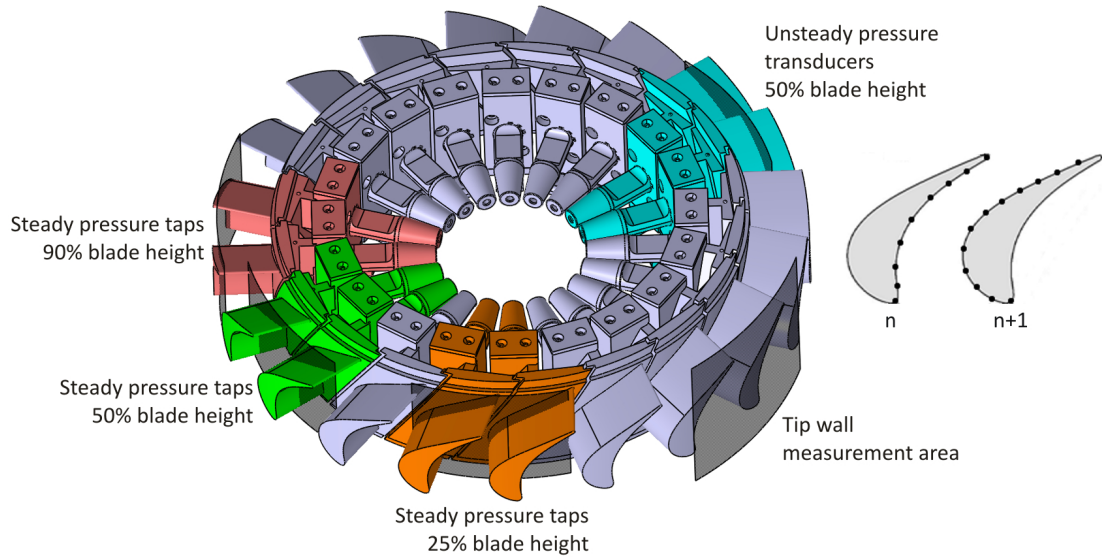


**Figure 3.7:** Overview of steady (orange 25%, green 50% and red 90% blade height), unsteady (blue 50% blade height) and tip-wall pressure-tap distributions along the cascade.

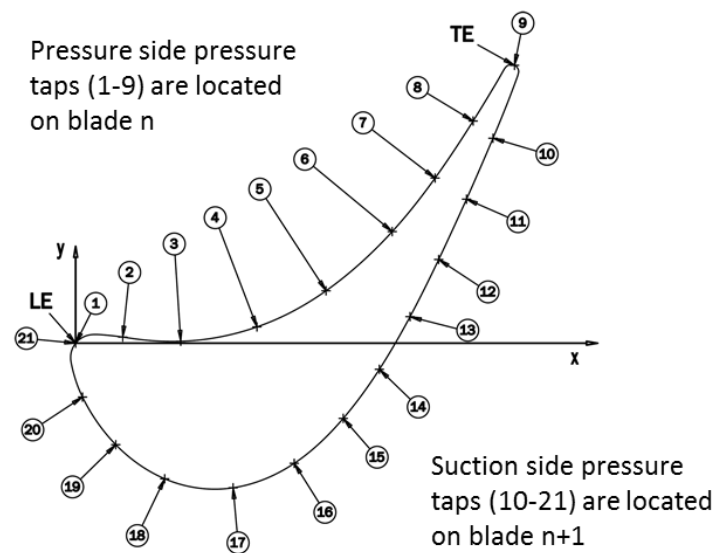
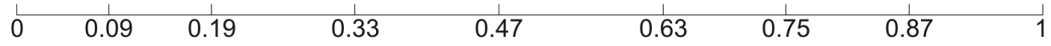


**Figure 3.8:** Steady and unsteady pressure-tap locations along the blade surface, merged onto one blade (from Rottmeier [2003]).

## Experimental Setup

---

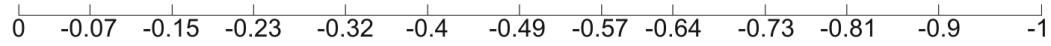
Non-dimensional curvilinear coordinate ( $s$ ) for PS:



Unsteady pressure transducer (UPT) position on PS:



Non-dimensional curvilinear coordinate ( $s$ ) for SS:



Unsteady pressure transducer (UPT) position on SS:

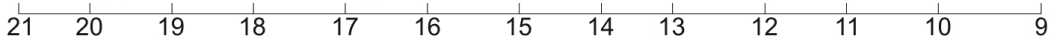


**Table 3.2:** Relation between the curvilinear coordinate  $s$  and the steady and unsteady pressure-tap locations along the blade surface.

## 4 Experimental Test Cases

THIS chapter presents the investigated test cases and depicts their motivation. The test cases comprise single-blade and cluster configurations. The difference between both is that for single-blades no physical connection between the individual blades in the blade-row exists, whereas for cluster configurations fixations between the blades are simulated in the non-rotation test facility. This, as they appear in real turbomachinery applications, such as two blades which are welded-in-pair or four blades which are cast as a piece. These types of clusters are introduced in order to increase the aerodynamic stability of the configuration in contrast to only single-blades in a blade-row and also to reduce the part count in the blade-row and therefore the production costs too. The grouping of the blades, cast or welded, depends on the complexity of the three-dimensional blade design.

As a result of the increase in stiffness, which is due to the grouping of the blades the cluster oscillates in a different mode-shape as it would be the case for single-blades, thus influencing differently the aerodynamic stability. The kinematics of these new mode-shapes can be specified by the oscillation direction, the vibration amplitude and the phase relation of the individual cluster-blades.

The test cases investigated in this work are selected on the basis of the two above-mentioned parameters:

1. the number of blades per cluster, which is defined to be identical for all clusters in the blade-row
2. the mode-shape of the cluster

In order to enable a comparison of the individual test cases, one subsonic flow condition is chosen and applied on a rigid prismatic turbine blade, illustrated in Figure 4.1. All measurements are carried out in the traveling-wave mode (see Section 2.2), with the blade-row oscillating in all possible inter-cluster phase angles which can be achieved for the individual test case. Additionally to the cluster test cases, single-blade test cases are carried out. It shall be noted at this point, that if not otherwise indicated in the following, single-blade test cases

## Experimental Test Cases

always refer to measurements for which the blades in a blade-row are not fixed together and all blades are oscillating in the traveling-wave mode. The single-blade test cases are selected so that similar oscillation directions are investigated as applied to the individual cluster-blades in a cluster. They therefore represent the reference in terms of aerodynamic stability as they are the base configuration in a blade-row. This enables a comparison between the cluster and the single-blade test cases and thus identification of differences in the aerodynamic stability of the individual cluster-blades due to the grouping of the blades. Additionally, as the single-blade test cases have the same oscillation direction as the individual cluster-blades, an attempt is made to validate the procedure of using single-blade test data to predict individual cluster-blades by using the relationship between the traveling-wave and influence coefficient formulation.

The following subsections introduce first the sign convention of the blade vibration direction, and second the cluster and the single-blade test cases. A brief summary of all test cases can be found in Table 1.2.

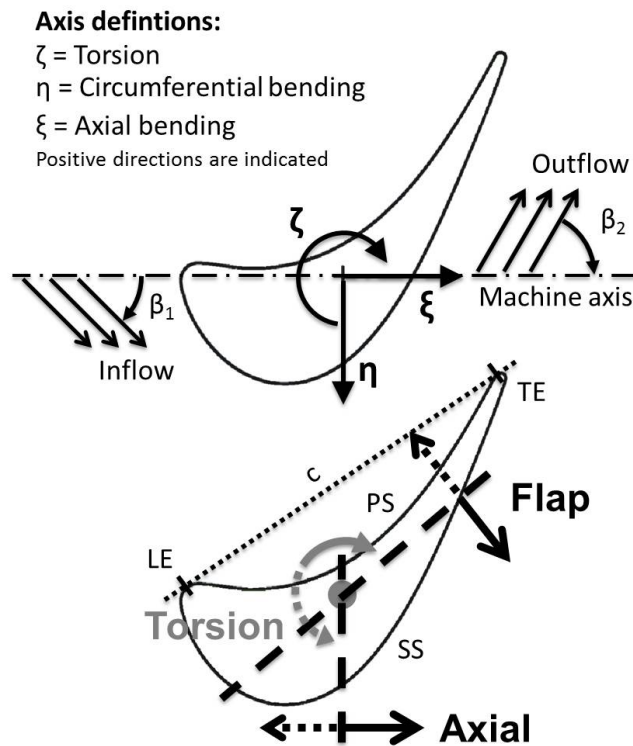


**Figure 4.1:** Definition of the blade vibration coordinate system. The positive oscillation directions of the investigated test cases are indicated with a solid line.

### 4.1 Sign Convention of the Blade Vibration Direction

Figure 4.1 presents, besides the cross-section of the investigated prismatic turbine blade, the blade coordinate system for which the following definition can be noted:

- The origin of the system is positioned in the center of rotation of the blade and the blade structure.
- The positive axis  $\xi$  in the blade axial direction is parallel to the machine axis and points downstream.
- In the blade circumferential direction, the positive axis  $\eta$  is perpendicular to the axis in the axial direction and points towards the suction-side of the blade.
- The torsional direction  $\zeta$  is defined as positive in the clockwise direction, completing the coordinate system and complying with the right-hand rule.

Based on the sign-convention, the positive torsion, axial and flap-bending oscillation directions are indicated by a solid line at the lower blade depicted in Figure 4.1.

### 4.2 Two-Blade Cluster

Overall, three two-blade cluster test cases are investigated in the non-rotating test facility (see Chapter 3). These test cases are based on two blades welded-in-pair and oscillating with different cluster mode-shapes. From a mechanical point of view, both blades are fixed together at both ends in the radial direction. In Figure 4.2 at the top left, an example of such a configuration is presented.

As previously outlined and as stated in various works of research (for example Whitehead and Evans [1992], Chernysheva [2004] and Corral et al. [2007]), the mode-shape of the cluster has a significant influence on the aerodynamic stability. Therefore the mode-shape of the cluster is chosen being the parameter to be investigated. One mode-shape of particular interest is an oscillation of both welded-in-pair blades which is perpendicular to the chord. This oscillation direction appears most in turbines due to the curvature of the blades in combination with the flow direction. It should be pointed out that this oscillation direction is therefore also of interest in the case of single-blades. In the following, this oscillation direction is referred to as flap-bending. In addition to the flap-bending oscillation direction, a second bending oscillation direction is selected, which is in the axial-direction. This is chosen in order to identify any influences on the aerodynamic stability of the blade related to a change in the oscillation direction. The third oscillation direction chosen is in the torsional direction, since it has been identified by previous works of research (the same authors as noted above) that the minimum aerodynamic damping in this case is susceptible to the grouping of blades compared to single-blades. Furthermore it is one of the oscillation directions that appears frequent in turbines.

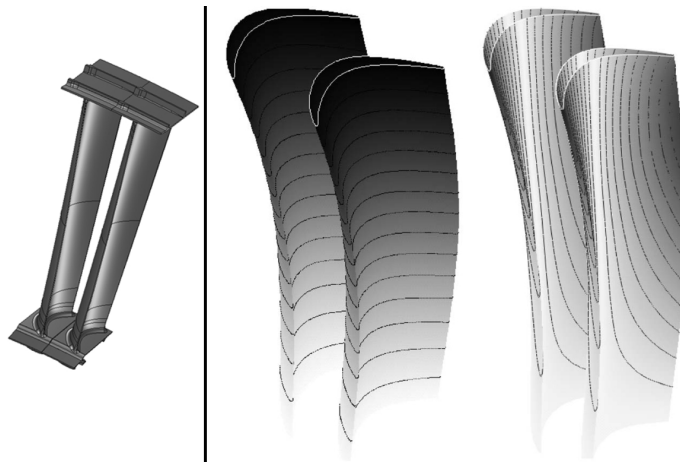


**Figure 4.2:** Left: example of a welded-in-pair low-pressure turbine cluster (from Zanker et al. [2013]). Middle and right: deformation example of a welded-in-pair low-pressure turbine cluster for the first bending and first torsion mode-shapes obtained from a bladed-disk finite element method (from Corral et al. [2007]).

The deformation pattern of the welded-in-pair blades for a bending- and a torsion mode-shape are exemplified in Figure 4.2, respectively in the middle and on the right. Both deformation examples are obtained by a bladed-disk finite element method performed by Corral et al. [2007]. The authors stated that the identified mode shapes are almost two-dimensional, whereas for the torsion mode-shape an exception of the two-dimensionality is stated for the blade root. For the bending mode-shapes, they concluded that both blades have similar deformation iso-contours and are seen in a first approximation as rigid bodies. Thus they can be modelled with the turbine blades of the non-rotating test facility (see Section 3.2). For the torsion mode-shape, because minimal differences between the iso-contour lines can be found at the blade root and tip, a part span height of this configuration is simulated in the non-rotating test facility.

The kinematic features of the welded-in-pair configuration can be replicated in the test facility by adjusting the blade-vibration amplitude and phase individually for each blade vibration-system (see Section 3.3). This is done in such a way that each two consecutive blades in the blade-row are always moving in-phase with an identical blade vibration amplitude. Therefore, with respect to the traveling-wave formulation, an inter-blade phase angle of  $\sigma_\lambda = 0^\circ$  is always present between the blades of a cluster. Between the blades of two adjacent clusters, the inter-cluster phase angle  $\Gamma_\lambda$  is applied, thus in the case of 20 blades in the blade-row results in a total of 10 possible clusters and 10 inter-cluster phase angles, all of which have to be considered.

In order to simulate the previously-introduced oscillation directions the modular setup of the blade vibration system is applied. In the case of bending-oscillation, a bending-suspension is chosen, which can be adapted in order to represent either a suspension in an axial- or flap-bending direction (see Section 3.2 and Figure 3.4 at the top right). To simulate the torsion oscillation a suspension is chosen which enables a movement of the blade vibration system in



the torsional direction and suppresses any bending movement (see Figure 3.4, middle right). In Table 4.1 the principal parameters defining this cluster are stated, namely for the test cases: C2-A for the bending mode-shape in the axial direction (Figure 4.3, top right), C2-F for the bending mode-shape in the flap direction (Figure 4.3, middle right) and C2-T for the torsion mode-shape (Figure 4.3, bottom right). It should be noted that each oscillation direction suppresses all others possible, thus the oscillation is assumed to be one-dimensional.

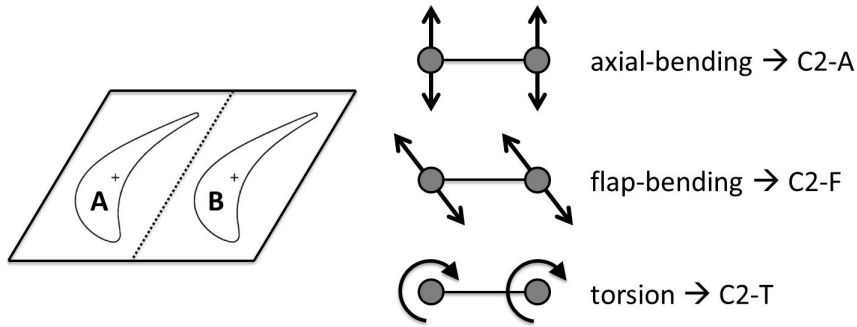


**Figure 4.3:** Left: two blade-vibration systems indicated as a cluster. Right: two-blade cluster oscillation directions (top: flap-bending; middle: axial-bending; bottom: torsion).

Test case:		C2-A	C2-F	C2-T
<b>Cluster blade A:</b>	<b>Oscillation-direction:</b>	Axial	Flap	Torsion
	<b>Amplitude:</b>	$h_{ax}$	$h_{fl}$	$\alpha$
<b>Cluster blade B:</b>	<b>Oscillation-direction:</b>	Axial	Flap	Torsion
	<b>Amplitude:</b>	$h_{ax}$	$h_{fl}$	$\alpha$
<b>Cluster-blades phase-constraint:</b>		In-phase	In-phase	In-phase
<b>Traveling-wave type:</b>		ICPA	ICPA	ICPA
<b>Total number of ICPA:</b>		10	10	10

**Table 4.1:** Test case specifications of the two-blade cluster configurations.

### 4.3 Four-Blade Cluster Simulating Torsion

This cluster is meant to represent a four-vane stator segment of a low-pressure turbine performing a torsional movement as a cluster. Such a four-vane stator segment is presented in Figure 4.4 on the left. All four vanes are fixed to one another on the hub and shroud side. On the right of this figure, a structural analysis is presented (performed by GE Avio S.r.l.) which simulates a torsional movement of the four-vane stator segment fixed together at the tip. The structural analysis indicates that in the region near the hub side an almost rigid body movement of the individual cluster-blades is present. The present test case intends to simulate this motion.

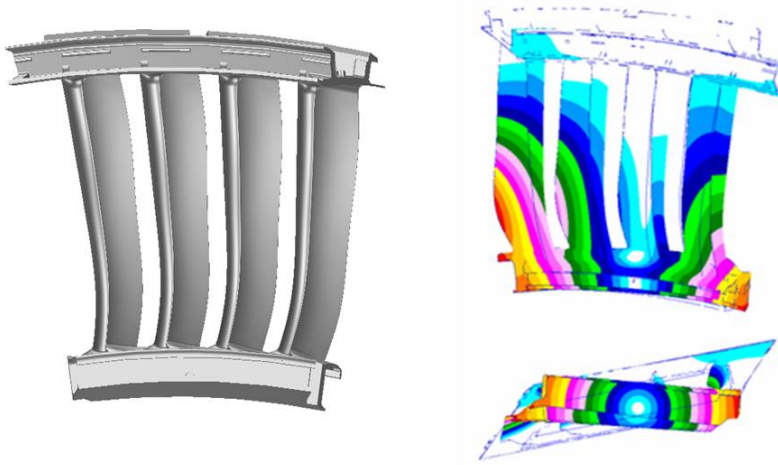


**Figure 4.4:** Left: four-vane stator segment of low-pressure turbine (from GE Avio S.r.l.). Right: torsional deformation of a four-vane package fixed together at the tip, simulated using a structural analysis (from GE Avio S.r.l.).

The blade-row in the non-rotating test-facility consists of 20 single-blades. This means five clusters can be modelled and thus five inter-cluster phase angles  $\Gamma_\lambda$  can be investigated. In order to simulate a torsional motion of a cluster using individual blade oscillations, an axial-bending direction is chosen and the blade oscillation amplitudes and phases are adjusted accordingly. In Figure 4.5 at the top, the torsional movement of a four-vane stator segment is schematically illustrated. In the middle of Figure 4.5 the oscillation of the individual blade vibration-systems (see Section 3.3) in the axial-bending direction is depicted in red and shown at the bottom as the movement of the blades. Before further detailing the kinematics of this cluster, the following two definitions shall be introduced. The inter-blade channel existing between two consecutive clusters is in the following referred to as the outer-cluster channel. Accordingly, the inter-blade channels existing between the individual cluster-blades are referred to as the inner-cluster channels in a cluster.

Due to the grouping of the blades, a fixed blade-vibration phase lag exists between the individual cluster-blades of the inner-cluster channel. In order to simulate the torsional movement of the cluster, cluster-blades A and B have to move in-phase. Cluster-blades B and C have to

### 4.3. Four-Blade Cluster Simulating Torsion

move in opposite-phase and cluster-blades C and D in-phase. As cluster-blades B and C move in opposite-phase, cluster-blades A and D also move in opposite-phase, as previously stated. With respect to the blade vibration amplitudes, cluster-blades A and D are defined as having a nominal amplitude in the axial-direction. Thus cluster-blades B and C have a third of the nominal blade vibration amplitude in order to simulate the torsional movement around the cluster-rotation axis between cluster-blades B and C. The individual cluster-blade kinematics are summarized in Table 4.2.

Overall, and as previously defined, it can be noted that for all inter-cluster phase angles appearing in the outer-cluster channels, the individual cluster-blade vibration amplitudes and phase angles have to be adjusted. This is necessary in order to simulate a torsional movement of the cluster by applying an axial-bending oscillation direction of the individual cluster-blades.

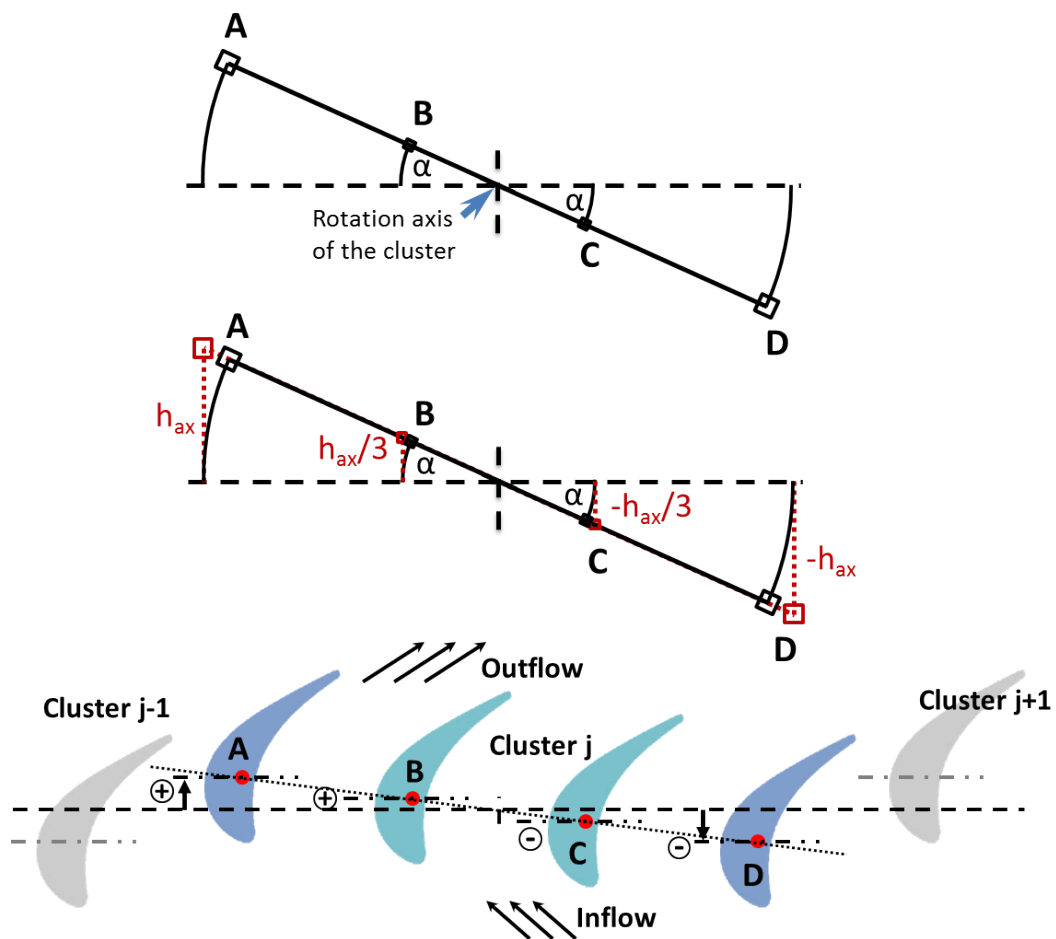


**Figure 4.5:** Modelling of the torsional cluster movement by using an axial-bending oscillation direction for the individual cluster-blades. Exaggerated schematic description of the real four-blade vane segment motion (black) and the simulated motion (red) in the non-rotating test facility.

## Experimental Test Cases

When reflecting a real torsional motion of the four-blade cluster as a whole (see Figure 4.5 at the top), each individual cluster-blade would vibrate along a fraction of a circle and would undergo a translational-torsional displacement. Whereas the cluster movement simulated in the non-rotating test facility is defined by each cluster-blade oscillating along the axial-bending direction (see Figure 4.5 in the middle). Comparing both movements (real torsional: black; simulated via the axial-bending direction: red) the following can be identified: differences between the end position and the rotation of the individual cluster-blades. For example, cluster-blade A in the non-rotating test-facility is not rotated and is further away from the rotation axis of the cluster than the same cluster-blade performing a real torsional movement. In order to estimate the impact of this, the ratio between the cluster-blade vibration amplitude and the radius from the center of the cluster to the individual cluster-blade is determined. As the ratio indicates (three orders of magnitude difference) it is assumed that the vibration along the circle is linear and the fraction of torsional movement negligible.

<b>Test case: C4-A-S-T</b>	
<b>Cluster blade A:</b>	<b>Oscillation-direction:</b> Axial
	<b>Amplitude:</b> $h_{ax}$
	<b>Phase:</b> ICPA
<b>Cluster blade B:</b>	<b>Oscillation-direction:</b> Axial
	<b>Amplitude:</b> $h_{ax}/3$
	<b>Phase relative to blade A:</b> $0^\circ$
<b>Cluster blade C:</b>	<b>Oscillation-direction:</b> Axial
	<b>Amplitude:</b> $h_{ax}/3$
	<b>Phase relative to blade A:</b> $180^\circ$
<b>Cluster blade D:</b>	<b>Oscillation-direction:</b> Axial
	<b>Amplitude:</b> $h_{ax}$
	<b>Phase relative to blade A:</b> $180^\circ$
<b>Traveling-wave type:</b> ICPA	
<b>Total number of ICPA:</b> 5	

**Table 4.2:** Test case specifications of the four-blade cluster configuration.

## 4.4 Single-Blade

The single-blade test cases comprise three oscillation directions, which are directly related to the cluster test cases introduced in the previous sections. This is because the single-blade test cases are meant to serve as a reference to compare to the cluster test cases. The single-blade traveling-wave measurements comprise all possible inter-blade phase angles (20). In Table 4.3 the test case specifications are summarized.

<b>Test case:</b>	<b>SB-A</b>	<b>SB-F</b>	<b>SB-T</b>
<b>Oscillation-direction:</b>	Axial	Flap	Torsion
<b>Amplitude:</b>	$h_{ax}$	$h_{fl}$	$\alpha$
<b>Traveling-wave type:</b>	IBPA	IBPA	IBPA
<b>Total number of IBPA:</b>	20	20	20

**Table 4.3:** Test case specifications of the single-blade configurations.



## 5 Measurement Techniques

**I**N this chapter, the measurement techniques applied to determine the aerodynamic stability of cluster- and single-blades are detailed. As highlighted in Chapter 2, different steady and unsteady values are necessary to determine the trend towards aerodynamic stability of an oscillating blade. The following sections highlight the measurement techniques necessary to determine these values. This includes a description of the individual steady and unsteady values measured next to the data acquisition procedure. The last section details the data-reduction procedure which determines the aerodynamic stability parameters for cluster- and single-blades. This is based on the measured data and the theoretical concept described in Chapter 2. The following Chapters 6 and 7 present the steady-state and the time-resolved results.

## 5.1 Steady-State Measurements

### 5.1.1 Up- and Downstream Flow Quantities

Two 5-hole L-shaped aerodynamic probes (Figure 5.1, left) are used to measure the steady-state flow quantities up- and downstream of the test section. In Figure 5.1 on the right, the positions of the probes relative to the blade's leading-edge (LE) and trailing-edge (TE) are presented.

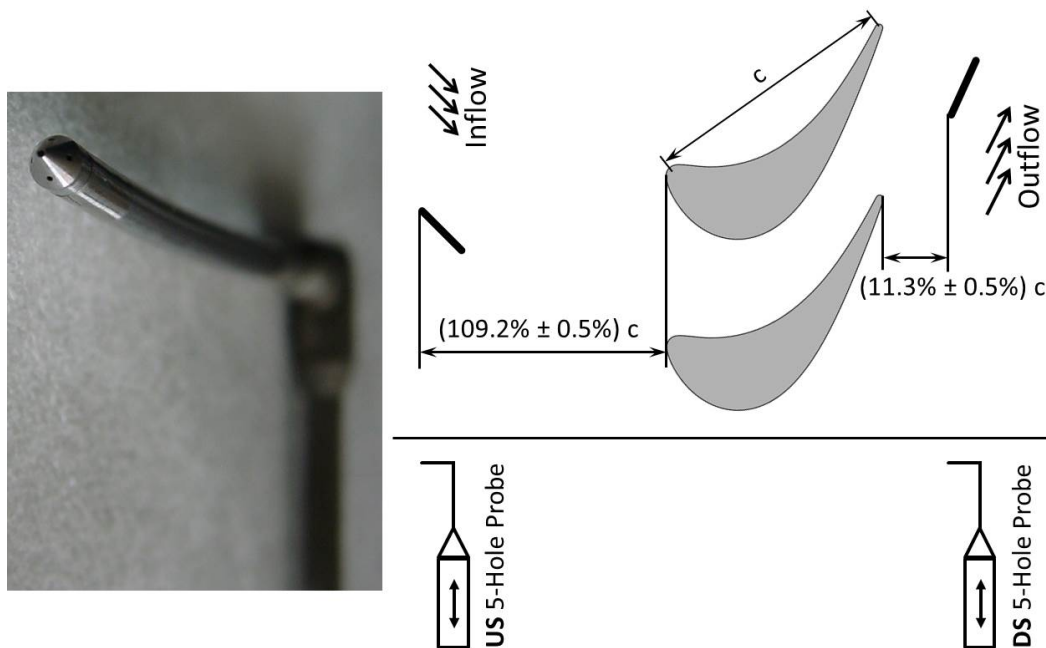


**Figure 5.1:** Left: 5-hole L-shaped probe (from Rottmeier [2003]). Right: probe traversing locations relative to the blade LE and TE.

The probes are fixed on precise industrial linear displacement systems, which are in turn fixed on the probe holders and mounted on the outer wall of the test facility (see Figure 3.3, item 13). The probe heads are aligned with the mean flow direction. The displacement system allows a stepwise displacement of the probes in the radial direction, and the rotation indexing of the cascade allows a stepwise movement in the circumferential direction. A typical measurement grid includes locations in the radial direction in steps of 2.5 mm (maximal step distance 3.5 mm) and in the circumferential direction in steps of  $1^\circ$  (minimum length; 1 pitch consisting of 18 steps  $\times 1^\circ$ , see Figure 5.2).

The probes are calibrated at EPFL in the Laval nozzle. The pitch angle is calibrated for a range of  $\pm 15^\circ$  and the yaw angle for  $\pm 16^\circ$ . Both angles are calibrated for a Mach-number range of 0.1 - 0.95. The calibration is performed according to the process proposed and verified by Schläfli [1986] and Capone [2000, 2001]. During the calibration process, five coefficients are determined for each probe. These coefficients are implemented in the data-acquisition



## 5.1. Steady-State Measurements

program applied to the measurements. The calibration allows the data-acquisition program to determine the total- and static-pressure, the Mach-number as well as the yaw- and the pitch-angles.

To acquire the probe pressure data in digital form, a Scanivalve Digital Sensor Array (DSA, range: 2068 mbar) is used. This device records the pressures and transfers them to the data-acquisition PC, at which a LabView<sup>TM</sup> program applies the calibration coefficients to determine the flow quantities of interest. Additionally, the acquisition program ensures that each measured pressure is within a certain margin of reliability. The applied procedure calculates the arithmetic average and the standard deviation of a certain number of measurement samples (minimum 5). If the standard deviation is not less than one millibar after 20 acquired samples, the program is stopped and the measurement has to be repeated. This routine serves to identify whether stable flow conditions are present and guarantees a precise data acquisition.

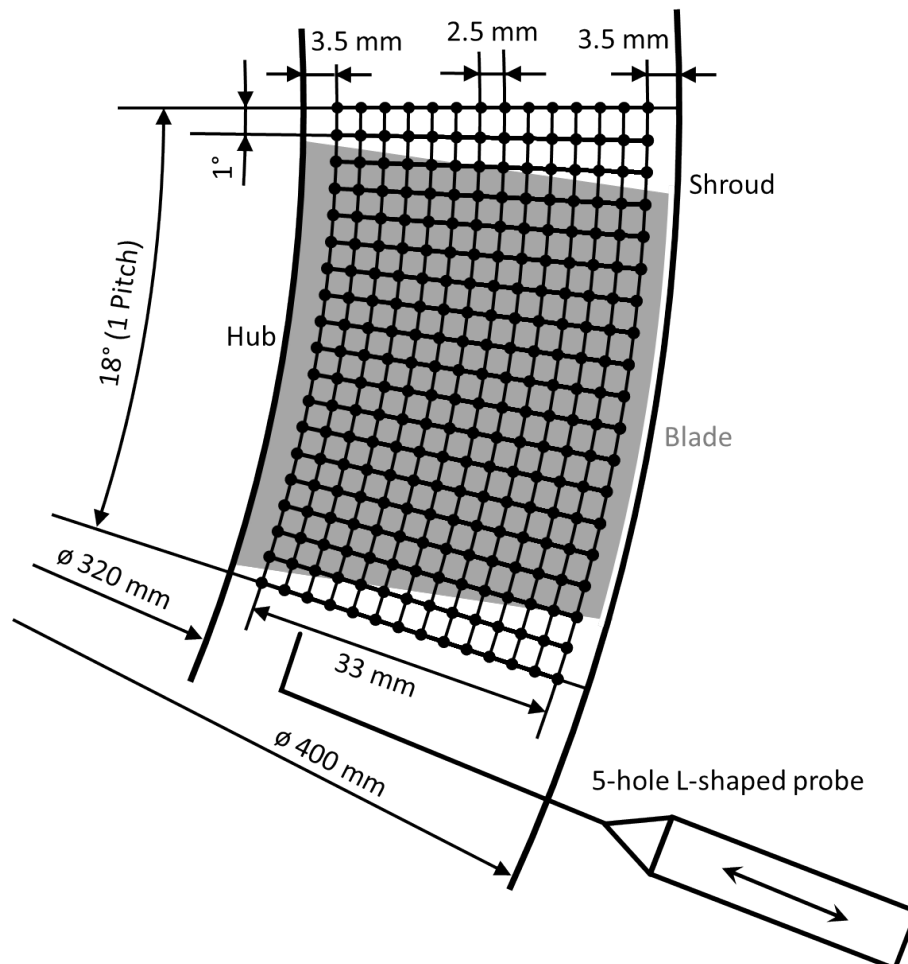


**Figure 5.2:** Probe traversing measurement grid.

### 5.1.2 Blade Surface Pressures

The steady-state blade surface pressures at the three different blade heights (25%, 50% and 90%) are measured using a Scanivalve DSA 3000 system. It consists of electric pressure sensors of the type Scanivalve DSA 3016, each having 16 pressure channel inputs. To control each of the channels, the DSA 3000 system has an embedded computer. This computer handles the ethernet communication with the data-acquisition computer and is able to perform a “zero calibration” of all channels. This is performed before each test cycle. Thanks to the calibration performed by the manufacturer, further calibrations of the temperature-compensated, piezoresistive differential pressure sensors (range: 2068 mbar) are not necessary. The calibration of the system leads to an accuracy of  $\pm 0.8$  mbar. The primary source of error is associated with the steady-state pressure values due to the settling time of the pressures. As settling time, the duration is considered until a change in pressure passes the long cavity between the blade surface and measuring sensor. This error is estimated to be approximately  $\pm 0.5$  mbar. As for the 5-hole L-shape probe measurement technique, a LabView<sup>TM</sup> program is put into place to monitor the standard deviation of the arithmetic average of the acquired pressure data samples. Furthermore, the LabView<sup>TM</sup> program is able to control the DSA 3000 system and to display the acquired blade surface pressures as blade surface isentropic Mach-numbers per blade height.

In order to ensure the comparability between the different test cases, the blades equipped with measuring sensors (Figure 3.7) are always positioned on the same circumferential position in the test facility for each test case.

### 5.1.3 Casing Surface Pressures

The steady-state outer-casing surface pressures are acquired to better understand the passing flow at the blade-tip region. In total, 18 pressure taps are located in the axial direction along the casing surface in the region of the test section (see Figure 3.2, item 10). The pressures are acquired in the same way as documented in Section 5.1.2, using a Scanivalve DSA 3000 system connected to the LabView<sup>TM</sup> data acquisition program. To map the passing tip-gap flow for the whole cross section of the blade profile, the airfoils are moved stepwise in the circumferential direction, passing the pressure taps at the shroud wall with their fixed location. For details, see the procedure measuring the flow quantities up- and downstream of the test section using 5-hole L-shaped probes (see Section 5.1.1). The measurement grid comprises a pressure tap array in the axial direction along the test section height (see Figure 3.2, item 10), and in the circumferential direction 18 measurements are acquired by moving the airfoil in steps of  $1^\circ$  covering one pitch.

## 5.2 Time-Resolved Measurements

### 5.2.1 Blade Surface Pressures

The unsteady pressure fluctuations along the blade surface are measured by two neighboring blades covering one inter-blade channel at the mid-span section (50% blade height). The cylindrically-shaped sensors are high-response piezo-resistive absolute pressure transducers (Endevco, Model 8534A-50) with a pressure range of 3448 mbar and a sensitivity in the region of 0.087 mV/mbar. Variations in the sensitivity are related to the manufacturing tolerances. The frequency response can range up to 300 kHz. In Figure 5.3, the mounting of the unsteady pressure transducer (UPT) in the blade is presented.

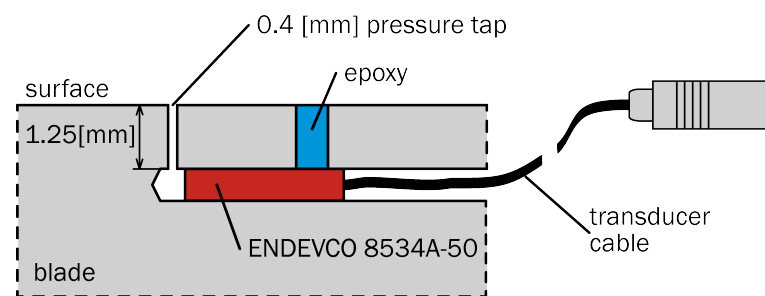


**Figure 5.3:** Embedded unsteady pressure transducer (adapted from Rottmeier [2003]).

The pressure taps have a diameter of 0.4 mm and are tap-drilled perpendicular to the blade surface. The pressure transducers are placed in a lateral hole passing below the blade surface. A second hole next to the pressure tap is filled with epoxy glue to fix the pressure transducer in the lateral position. The main advantage of this fixation is, that it protects the pressure transducer from physical impacts. In addition, the pressure measuring-membrane of the transducer is mounted perpendicular to the blade vibration directions, which means the influence of any acceleration effects due to the blade vibrations are negligible (see also Rottmeier [2003] and Beretta [2006]).

### 5.2.2 Blade Vibration Measurements

The displacement of each blade is measured using proximity probes. As described in Section 3.3, the displacement information is used to feed back the actual sinusoidal position of the blade to the vibration control system. This is in order to determine and control the amplitudes and phases of the blade movements by the vibration control system. The sensors used are Vibro-Meter<sup>®</sup> TQ 402 (Figure 5.4). Together with the matching IQS 452 conditioner, they allow a contactless measurement of the relative displacement between the mass element of the blade (Figure 3.3, item 3) and the displacement transducer (Figure 3.3, item 6).

The operation mode of the sensor is based on the eddy current principle. The sensor provides a small magnetic field which changes due to the movement of the metallic plate, placed in



**Figure 5.4:** Displacement transducer, Vibro-Meter<sup>®</sup> TQ 402.

front of the sensor (Figure 3.3, item 6) on top of the mass element (Figure 3.3, item 3). This change in the magnetic field induces an eddy current in the sensor, which is measured and amplified. This type of sensor is capable of measuring with a sensitivity of up to 4 mV/ $\mu\text{m}$  and has a frequency response of up to 20 kHz. The calibration procedure is described in Section 5.4.1 as well as details about the influences of the amplifiers.

### 5.2.3 Cluster Specific Procedures

For the time-resolved measurements of cluster test cases, a procedure is employed which is adjusted to the experimental setup of the test facility, the measurement equipment and the cluster configuration. Beforehand to the description, the following can be summarized as influencing factors of the procedure:

- two blades are equipped with unsteady pressure transducers (together they cover one inter-blade channel)
- the cluster configuration under investigation (e.g. two- and four-blade cluster)
- traveling-wave mode

As the items indicate, a complete data set for the minimum cluster configuration of two-blades cannot be acquired during one test run. Hence several test runs have to be performed in order to determine the unsteady pressures on all cluster-blade surfaces in a cluster for one inter-cluster phase angle in the traveling-wave mode measurement technique. This procedure will be illustrated using the four-blade cluster test case C4-A-S-T, and can be used respectively for the two-blade cluster test-cases.

Figure 5.5 depicts the measuring procedure for the individual blades in the four-blade cluster. Bearing in mind that only one inter-blade channel is equipped with unsteady pressure transducers, in total four measurements (first four lines in Figure 5.5) have to be performed to cover each inter-blade channel of the cluster. In order to do this the blade actuation (amplitude and phase) is adjusted accordingly via the vibration control system (see Section 3.3). The last line

## 5.2. Time-Resolved Measurements

in Figure 5.5 shows how the four measurements fit together to create a complete data set for each individual cluster-blade. As noted before, this method can be used accordingly for the test cases of a two-blade cluster.

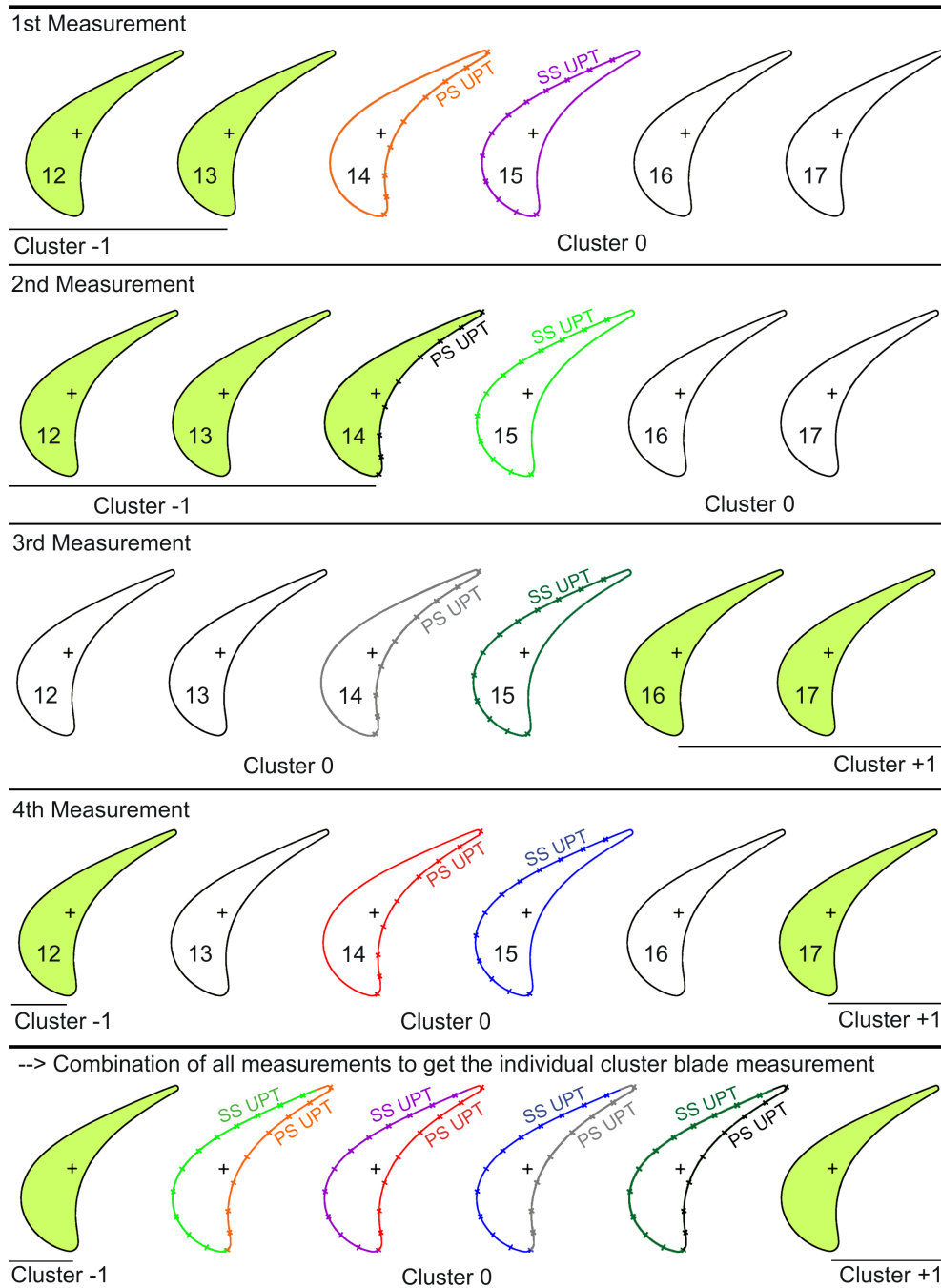


**Figure 5.5:** Description of the measuring and post-processing procedure of the four-blade cluster simulating a torsional movement.

### 5.3 Data Acquisition Systems

Two standard PCs are used to operate the data acquisitions systems (DAQ). One is dedicated to the steady-state parameters and the other to the unsteady parameters. Both are operated with National Instrument's LabView<sup>TM</sup> software, which allows the acquisition and saving of the measurement data as well as the handling of the measurement equipment. In Figure 5.6 a schematic overview of the data acquisition and control system is presented. In the following sections the context of the different sensors, amplifiers, control modules and data acquisition PCs is presented.

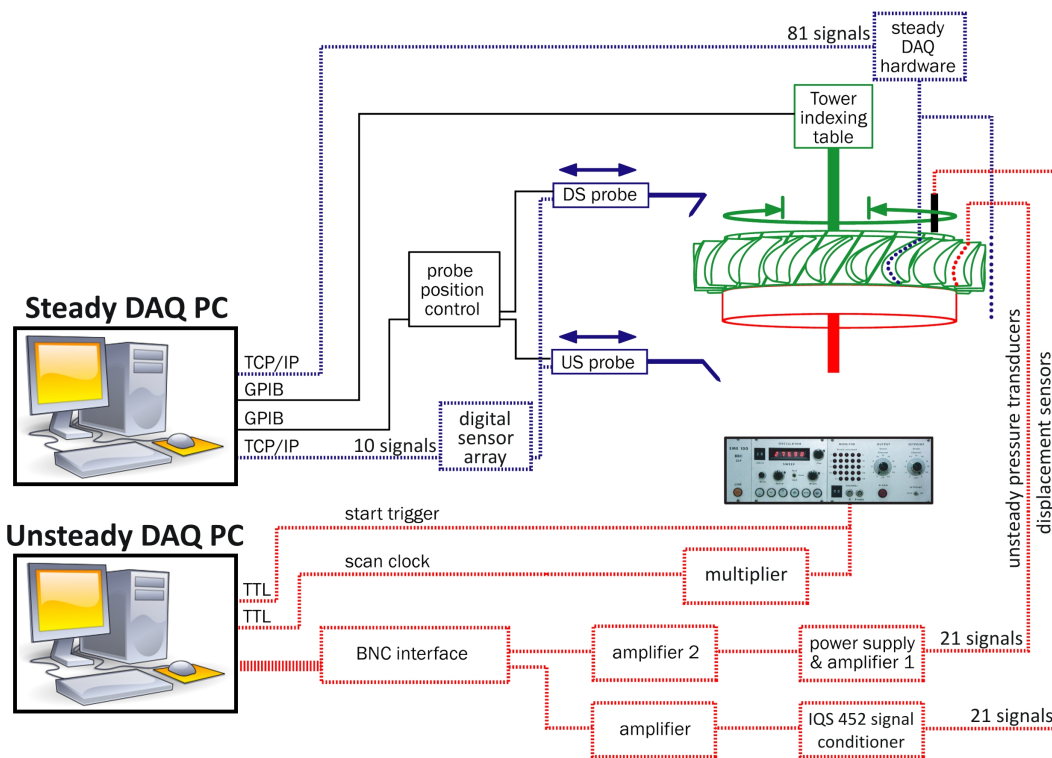


**Figure 5.6:** Schematic view of the data acquisition and control system (adapted from Beretta [2006]).

#### 5.3.1 Steady-State Measurements

The steady-state measurement system is devoted to the control and acquisition of the following measurement data:

- steady-state blade-surface and casing-surface pressures
- US- & DS-5-hole L-shaped aerodynamic probe pressures
- indexing of the measuring cascade

The steady-state blade-surface and shroud pressures are acquired using an Ethernet connection via the TCP/IP protocol to connect with the Scanivalve DSA 3000 system, as documented in Section 5.1.2. Another task of the steady-state PC is to acquire the pressures of the US- and DS- 5-hole L-shaped probes, as well as to move the probes in the radial direction. The communication with the industrial linear displacement motors is achieved by using a General Purpose Interface Bus (GPIB) and a probe position controlling device (isel step motor controller C-116). The pressures are acquired using a DSA module connected to the PC using an Ethernet connection with a TCP/IP protocol. The rotational indexing of the cascade permits a stepwise rotation of the cascade. Hence measurements in circumferential direction of the 5-hole L-shaped aerodynamic probes and the steady-state shroud pressure-taps are possible. Both measurement procedures are detailed in Section 5.1.1 and 5.1.3.

#### 5.3.2 Unsteady Measurements

The unsteady measurement system is devoted to acquiring the unsteady blade surface pressures and the individual blade displacements. To guarantee a good signal quality both time-resolved measurements have to be acquired simultaneously, preferably over several vibration cycles. The time depending of the signals allows different post-processing methods to be used (e.g. direct method or the ensemble-average method) to determine the unsteady pressure amplitude (modulus) and phase angle. In a second step, this enables the determination of the aerodynamic values of interest for the entire blade, such as the aerodynamic-damping and aerodynamic-work coefficient.

Figure 5.6 shows in a representative way two amplifiers and a power-supply unit connected to one unsteady pressure transducer. Each of the 21 pressure transducers is connected to such a set of electronics in order to provide the necessary power to the transducer to perform measurements. Furthermore, this system filters the DC component (steady part of the pressure) out of the signal and amplifies the unsteady signal by a factor of 10. In the second amplifier, a low pass filter (4 kHz) is applied to the measured signal supporting the signal quality (less aliasing errors). Furthermore, another amplification with a gain of either 10, 100 or 1000 is applied. The variation in gain of the second amplifier is used to adapt the voltage range of the measured unsteady pressure transducer signal to the voltage input range of the acquisition data boards. This adjustment is necessary, since the strength of the unsteady pressure transducer signal can vary due to local variations in the unsteadiness of the flow, for example when aerodynamic shocks exist.

Representative of displacement sensors, one measuring chain is detailed showing an amplifier and a signal conditioner (Figure 5.6). The signal conditioner provides the displacement transducer with the necessary power to create the magnetic field and to sense any change in the eddy-current value, which is proportional to the displacement of the corresponding blade. The following amplifier has the property of an adjustable gain. This is essential, since the vibration control system requires tuned sensitivities for all 20 blade-suspension systems, so

that for one given voltage all blades have an identical vibration amplitude (see Section 3.3). In total 21 displacements are measured: 20 are used to measure the displacements of the blade vibrations and one displacement sensor is dedicated to measure the position of the hydraulic brake (Figure 3.3, item 9).

Both time-resolved signal types, the 21 unsteady pressures and the 20 blade displacements, are connected via three Bayonet Neill Concelman (BNC) connector platforms (outside the PC) to three internally synchronized PCI-6071E National Instruments data-acquisition boards (inside the PC). Each of these cards can perform a multiplexed sampling of 32 signals with a maximum sampling rate of 1.25 MHz divided by the total number of acquired channels. The internal synchronisation of the three boards allows the sharing of the external trigger and external scan clock between the cards, ensuring that the three boards take the samples at the same moment.

For the data acquisition, a phase-locked technique is applied, ensuring that the number of samples per acquisition corresponds to a multiple of the number of samples per blade oscillation period. This technique avoids the effects of FFT leakage due to non-periodic samples, which would be the case if an arbitrary sampling frequency was used. Furthermore, the phase-lock technique ensures a high signal-to-noise ratio. The data-acquisition boards from National Instruments require two common input signals: a start trigger signal and a scan clock signal. Both signals are connected to the reference TTL signal of the cascade vibration-control system oscillator (see Figure 3.6), whereas the scan clock signal is multiplied (multiplication factors are in the range of  $2^n$  with  $n = 1 - 5$ ) to conform with the phase-lock technique requirements. Each scan clock signal initializes the acquisition of a single sample for all connected data channels. Common data sets consist of 32 samples per oscillation period with a total number of 512 periods (total number of samples per acquisition: 16384, representing one data set) for each acquired channel (in total 41 channels: 21 unsteady pressure transducers and 20 blade displacement sensors). Bearing in mind the applied phase-lock technique, the sampling frequency is a multiple of the oscillation frequency. To ensure the signal quality and verify the repeatability of the measured results, a minimum of two data sets per test condition (per IBPA/ICPA) are acquired and used as input for the data-reduction determining the aerodynamic values of interest. The two or more sets are acquired consecutively within a time frame of 2-3 minutes.

### 5.4 Unsteady Data-Reduction Technique

The basis of the unsteady data-reduction technique is the acquired unsteady data, as described in Section 5.3.2, and the application of the Fast Fourier Transformation. Of interest for detailed aerodynamic investigations are:

- the individual blade vibration amplitude
- the individual blade vibration phase angle



- the unsteady pressure-fluctuation amplitudes on the blade surfaces
- the unsteady pressure-fluctuation phase angle along the blade surface related to the reference blade displacement phase (typically the blade in which the unsteady pressure transducer is incorporated)

These parameters can be determined with the aforementioned measurement procedures. The data-reduction program is coded in the MATLAB<sup>®</sup> programming language and set up in a modular way permitting the simple adjustment of the different data-reduction program parts to the different blade vibration directions of the single-blade and the cluster configurations. In the following chapters further details are documented describing the unsteady data-reduction techniques for single-blade, two-blade cluster and four-blade cluster measurements. In particular, Section 5.4.1 is dedicated to the general data-reduction technique and the modular setup. Section 5.4.2 describes how the program modules are adjusted in order to enable a data-reduction of the different cluster types.

### 5.4.1 General Procedure

The data-reduction technique converts the acquired digital voltage signals of the unsteady pressure transducers and the blade displacement transducers to physical units of interest, (respectively Pascal and meter/degree of arc). In addition, it provides synchronous data of the aforementioned signals. The introduced time delay due to the applied measurement electronics (see Section 5.3.2) is known and corrected. For an overview of the used measurement electronics, see Figure 5.6. The main steps of the data-reduction process, starting with the sensor reading saved on the data acquisition PC and ending with the true physical value output, are presented in Figure 5.7.

The data-reduction process splits each signal into identical sections in a first step and performs then for each section a Fast-Fourier Transformation to convert it from the time to the frequency domain. As each signal consists of at least two data sets (each with 16384 data points) and as an overlapping of 50% for the individual data sections (8192 data points) is applied, in total six data sections are considered. In a following step the average of the sections is calculated. This is performed in order to increase the reliability of the results and to enable an estimation of the random error, which is described later in this section.

The Fast-Fourier transformation (also known as: harmonic signal analysis) of the data section permits an easy phase angle correction of the investigated signals. Furthermore it identifies the fundamental harmonics present at the vibration frequency of interest. The data-reduction continues and applies a time correction of each signal due to the multiplexing of the unsteady data acquisition. As described in Section 5.3.2, one data sample per channel is acquired with each rising edge of the scan clock signal. Each data sample of the different channels is stored in a consecutive way, with a fixed time delay of about 3  $\mu\text{s}$ <sup>1</sup>. Hence, knowing the time delay

---

<sup>1</sup>This value is given by the manufacturer and was validated by Beretta [2006].

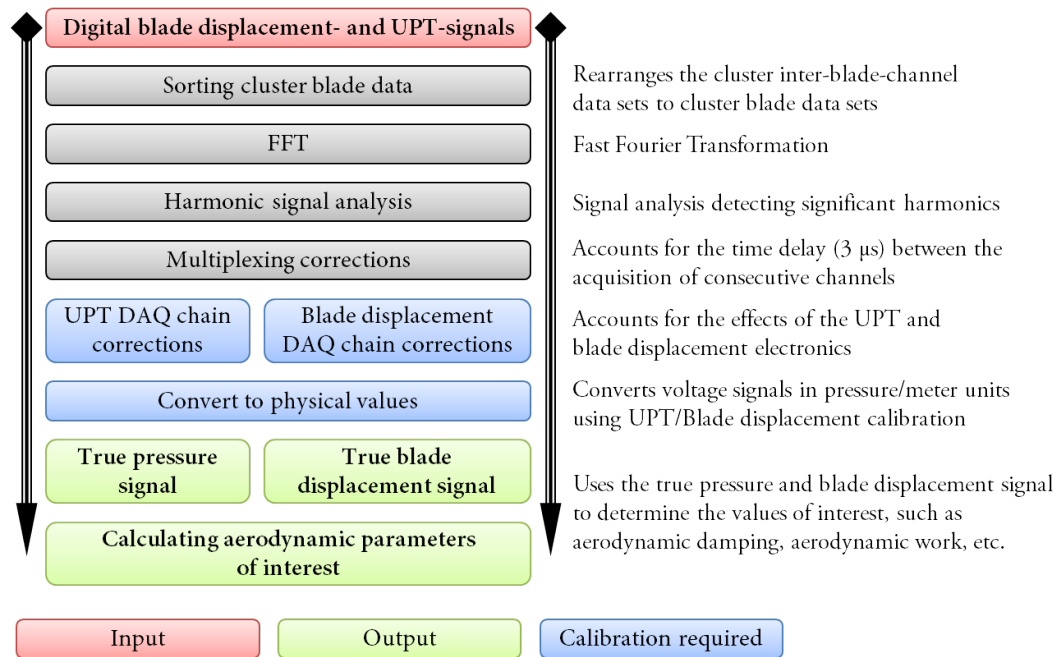


**Figure 5.7:** Overview of the unsteady data-reduction process for unsteady pressure transducers and blade displacement transducers.

means an effective correction can be performed during the data-reduction process.

The output of electrical sensors is usually given in voltage, which is proportional to the measured physical unit. The relation between the electrical signal of the sensor and the physical unit is described by the sensor's sensitivity, commonly provided by the sensor manufacturer. This sensitivity does not account for any influences introduced by external parameters. In order to maintain an accurate sensitivity, the latter have to be identified and accounted for. In the case of unsteady pressure transducers the influencing parameters are:

- the travel distance of the pressure fluctuation from the point of measurement (blade surface) to the sensor (embedded in the blade; see Figure 5.3)
- electronics handling the functionality of the sensor (amplifier, filter and power supply)
- range of the pressure fluctuation frequency
- orientation of the sensing surface with respect to the sensor's direction of movement

The last item is mentioned for completion, as documented in Section 5.2.1. The sensing surface of the unsteady pressure transducer is placed perpendicular to its movement axis and is therefore negligible. In order to cover the above-mentioned first three items, a calibration of each unsteady pressure transducer is necessary to account for modifications in the pressure amplitude and phase signal. This calibration is performed using an in-house-designed calibration device, displayed in Figure 5.8. The device creates a fluctuating pressure-signal which

is measured simultaneously by a reference unsteady pressure transducer<sup>2</sup> and the transducer to be calibrated. As the latter is connected to the measurement chain as described previously, a corrected sensitivity was determined. Finally, the corrected sensitivities are used in the unsteady data-reduction process to convert the measured voltage signal into pressure values (see Figure 5.7).

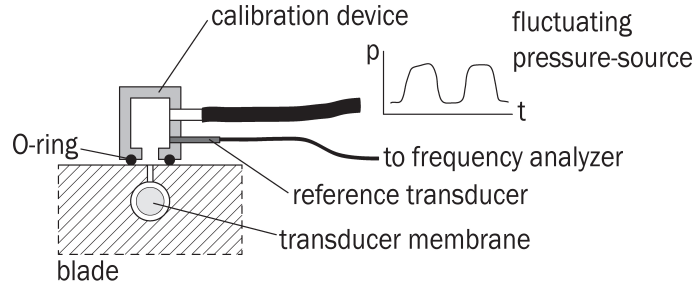


**Figure 5.8:** Application of the unsteady pressure transducer calibration device (adapted from Rottmeier [2003]).

As for the unsteady pressure transducers, the blade displacement transducers are affected by the electrical devices between each of the transducers and the data acquisition interface (see Figure 5.6). For the purpose of calibration, an acceleration sensor (type 4375, Brüel & Kjær) and a matching charge amplifier (type 2635, Brüel & Kjær) are used. As for the unsteady pressure transducers, the resulting amplitude and phase corrections are included in the post-processing procedure. The next step adjusts the gain of the sensor's amplifiers so that each calibrated sensitivity is identical. This is necessary to comply with the signal requirements of the vibration control system. An identical sensitivity allows the vibration control system to properly adjust amplitudes and phases of the vibrating blades. In total 21 displacement transducers are present, one for each blade vibration system plus one for the hydraulic flutter break (Figure 3.3, item 9).

In the last steps of the unsteady data-reduction technique, the unsteady pressure transducer and the blade displacement transducer corrections are applied, including the conversion from voltage to physical values. Furthermore, the aerodynamic parameters of interest (such as aerodynamic forces, damping and work) are calculated on the basis of the first harmonic of the unsteady pressure signal and then stored.

The unsteady data-reduction technique described above is similar to the one of Rottmeier [2003]. In his investigation he concluded that by taking into account the aforementioned calibrations and signal corrections, the unsteady pressure measurement uncertainty related to the systematic errors is considerably smaller than those originated from random errors. The latter are a result of random disturbances due to the turbulence in the flow or interferences. In order to account for these random errors a statistical error estimation is performed. As the true value of the unsteady pressure is unknown, it has to be assumed that it is situated with

<sup>2</sup>The sensitivity of the reference transducer was provided by the manufacturer and verified in-house.

a certain probability inside of a confidence interval. This confidence interval is determined by considering the number of sections per signal and by using the Student's t-distribution to determine the variance of the signal for a 95% confidence interval. It should be noted that the Student's t-distribution is chosen in order to account for the low number of sections as it is developed especially for low test sample numbers (see Bendant and Piersol [2009], section 4.4). The detailed mathematical procedure to determine this confidence interval of the complex unsteady pressure is detailed in Schläfli [1989] and was also used in other works of research as for example in Korbächer [1996] and Rottmeier [2003]. In Figure 5.9 it is illustrated how the confidence intervals of the unsteady pressure amplitude  $\Delta\hat{p}_s$  and phase  $\Delta\varphi_s$  influence the complex unsteady pressure coefficient  $\tilde{p}_s$ . In order to determine the confidence interval of the global aerodynamic damping coefficient (see Section 2.5), the confidence intervals of the unsteady pressure amplitude  $\Delta\hat{p}_s$  and phase  $\Delta\varphi_s$  are used.

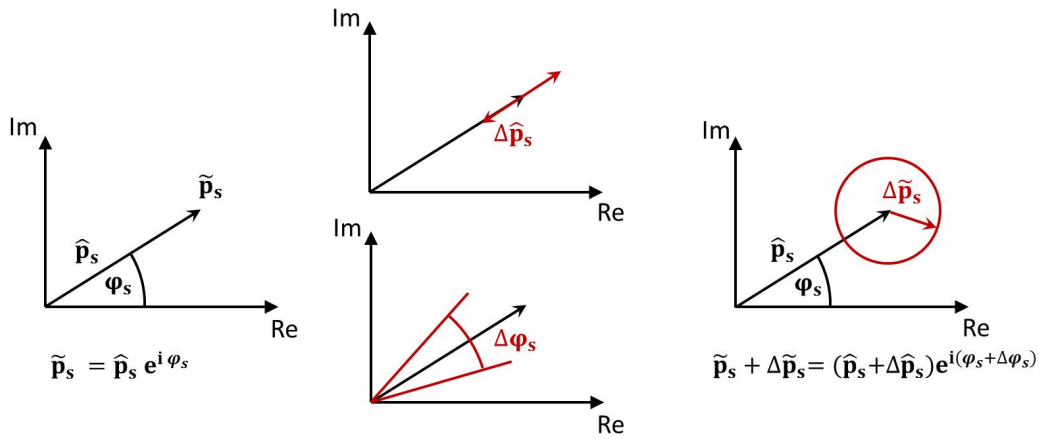


**Figure 5.9:** Illustration to determine the random error related to the unsteady pressure measurements (adapted from Schläfli [1989]).

### 5.4.2 Cluster Specific Procedures

The data-reduction technique described in the previous section is created in a modular way to easily adjust it for varying configurations, e.g. cluster. In Section 5.2.3, the measuring procedure was introduced for cluster test cases. It resulted in multiple test cycles for each of the cluster test cases. In order to combine and sort the data of the test cycles, an extra step has to be included in the data-reduction process. This step can be identified in the second line of Figure 5.7. The sorting is performed so that a complete data set (pressure- and suction-side) for the individual cluster-blades are present. It should be noted that a data set consists of unsteady pressure data and blade displacement data of the blade on which the unsteady pressure is measured. This ensures that the resulting phase lag between the unsteady pressure and the blade motion relates to the individual cluster-blades.

### 5.4.3 Exemplary FFT Spectra of Raw Signals

The previous section described the data-reduction of the time-resolved measurement data, in particular the unsteady pressure on the blade surface next to the blade oscillation. One of the first steps after rearranging the data is converting it from the time to the frequency domain. This is achieved by means of calculating a Fast-Fourier Transformation and the results are given as averaged raw amplitude spectra. In order to calculate the phase lag between both signals, it is necessary to determine the cross-correlation between both.

The example presented in this section represents a single-blade test case oscillating with an axial-bending oscillation direction (SB-A) and an inter-blade phase angle of  $\sigma_\lambda = 90^\circ$ . In Figure 5.10, the raw amplitude spectra of the unsteady pressure signal are presented. The graph at the top-left represents the pressure tap at the leading-edge position. The top-middle and top-right hand graphs represent pressure taps on the pressure-side positions, PS 3 and PS 7. The graphs below represent the pressure taps at the suction-side positions, SS 10, SS 16 and SS 19. The individual positions can be consulted in Figure 3.8. In Figure 5.11, the raw amplitude spectra of the blade oscillation is shown for two blades, which represent those on which the unsteady pressure transducers are mounted (see Figure 3.7).

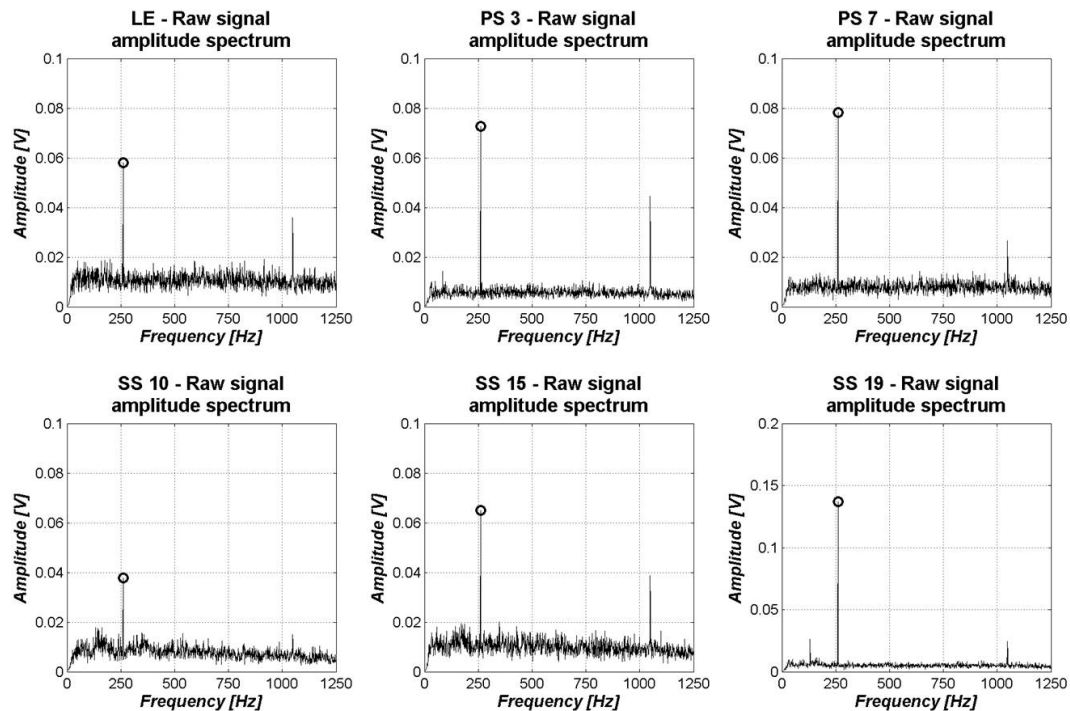


**Figure 5.10:** Averaged raw unsteady pressure amplitude spectrum for the single-blade test case SB-A (axial-bending oscillation direction), IBPA  $\sigma_\lambda = 90^\circ$ .

Within both figures, the fundamental (1<sup>st</sup>) harmonic amplitude is indicated with a circle. Focussing on the shape of the detected peaks, it can be observed that all are of a sharp nature. This is an indicator that no spectral leakage is present when calculating the Fast-Fourier

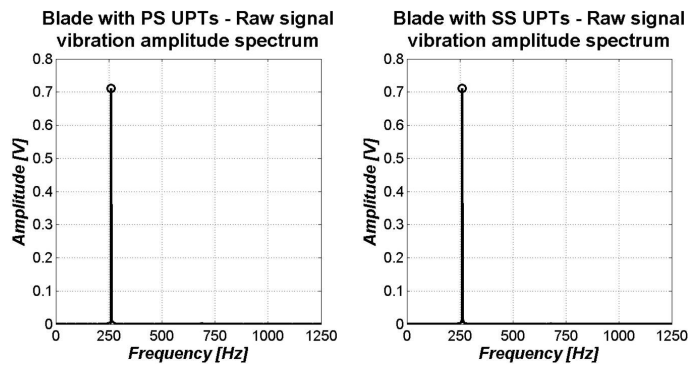


**Figure 5.11:** Averaged raw blade oscillation amplitude spectrum for the single-blade test case SB-A (axial-bending oscillation direction), IBPA  $\sigma_\lambda = 90^\circ$ .

transformation. Hence, it can be assumed that the determined amplitudes reflect the measured amplitudes. Additionally, it can be seen that the detected peaks are well distinguishable from the noise. These two factors support the calculation of the cross-correlation (phase lag) between the unsteady pressure and the blade oscillation, since the better these two factors are the better the cross-correlation determines the phase lag.

As Rottmeier's [2003] conclusions show, the 2<sup>nd</sup> peak observed in Figure 5.10 between 1 - 1.1 kHz is a result of the vibrating splitter disk, which is placed between the inner and outer settling chamber (see items 3 and 4 in Figure 3.2). Its vibrations in the aforementioned frequency range produce the detected pressure fluctuations. Considering that no further peaks can be identified within the unsteady pressure spectra, it can be stated that the unsteady pressure fluctuations generated by the blade oscillation and measured at the blade vibration frequency are sinusoidal. For all test cases investigated, the measured signals are similar to those presented, whereas it is stated that a variation in the amplitudes exists depending on the blade vibration direction, the inter-blade/-cluster phase angle and cluster configuration.

## 6 Steady-State Flow

THIS chapter is dedicated to present the steady-state flow measurement results of the test cases investigated in Chapter 7, all of which feature identical steady-state flow conditions. Since the unsteady results of the different test cases (single-blade and cluster) are compared to each other, the steady-state test results have to be as identical as possible. This is also presented in this chapter.

The steady-state test conditions are measured by two 5-hole L-shaped probes (see Section 5.1.1), one upstream and one downstream of the measuring cascade. Additionally, measurements are taken along the outer wall (see Section 5.1.2) and the blade surface (see Section 5.1.3).

### 6.1 Definitions

For expressing steady-state parameters, next to the isentropic Mach-number the in- and outflow angles are commonly used. The isentropic Mach-number is defined as:

$$M_{is} = \sqrt{\frac{2}{\kappa - 1} \left[ \left( \frac{p_{tI}}{p_{stat}} \right)^{\frac{\kappa-1}{\kappa}} - 1 \right]} \quad (6.1)$$

where  $\kappa$  is the ratio of specific heats for air ( $\kappa = 1.4$ ) and  $p_{stat}$  the static pressure at the measuring location along the blade surface (see Section 5.1.2) or the shroud wall (see Section 5.1.3). The inlet total pressure  $p_{tI}$  is represented by the arithmetic average along one pitch at mid-channel height, which is measured by the upstream 5-hole L-shaped probe (see Section 5.1.1). The in- and outflow angles are defined in relation to the machine axis as described in Figure 4.1.

## 6.2 Measurement Results

In Table 6.1 the results of the 5-hole L-shape probes are presented for each test case. The documented measured values (upstream and downstream) are calculated as arithmetic averages in the circumferential direction over one blade passage (18°, every 1°) at mid-channel height in the radial direction.

Case		Mach-	Flow	Total	Static	Ambient	Total
		number	angle	pressure	pressure	pressure	temper- ature
		M [-]	$\beta$ [°]	$p_t$ [hPa]	$p_{stat}$ [hPa]	$p_{amb}$ [hPa]	T [K]
SB-A & C2-A	US:	0.35	45.9	1337	1231	958	301.6
	DS:	0.68	-57.7	1292	949		-
SB-F & C2-F	US:	0.34	46.0	1354	1249	976	300.9
	DS:	0.68	-58.5	1310	961		-
SB-T	US:	0.34	45.9	1332	1232	950	300.6
	DS:	0.70	-57.8	1297	933		-
C2-T	US:	0.34	45.9	1332	1231	948	300.4
	DS:	0.70	-57.9	1296	928		-
C4-A-S-T	US:	0.35	46.0	1358	1250	967	300.9
	DS:	0.68	-57.8	1315	958		-
Average	US:	<b>0.34</b>	<b>46</b>	<b>1343</b>	<b>1239</b>	-	<b>300.9</b>
	DS:	<b>0.69</b>	<b>-57.9</b>	<b>1302</b>	<b>946</b>		-
Standard deviation [%]	US:	<b>1.4</b>	<b>0.1</b>	<b>0.9</b>	<b>0.8</b>	-	<b>0.1</b>
	DS:	<b>1.9</b>	<b>-0.6</b>	<b>0.8</b>	<b>1.6</b>		-

**Table 6.1:** Steady-state mean flow quantities at mid-span (50% blade-height), arithmetically averaged in circumferential direction over one pitch (18°, each degree one measurement).

By comparing the results of the various measurements in Table 6.1, it can be seen that almost identical test conditions for all test cases are achieved. At the bottom of the table, the average and the standard deviation of all test cases are noted. The low values of the standard deviation confirm the aforementioned conclusion, that close to identical test conditions were achieved for the different test cases. The small differences between the individual test cases were expected and are related to external parameters, such as slightly varying ambient conditions. Considering that the unsteady measurement results of the different configurations (single-blade and cluster) are compared with one another, these almost identical steady-state flow results are the basic requirement to perform this comparison.



In addition to the aforementioned 5-hole L-shaped probe measurements, the blade surface static pressures are evaluated by using the isentropic Mach-number (see Equation 6.1). These results serve as a basic requirement for comparing the test cases with one another. Tables 6.2 and 6.3 document the isentropic Mach-number as a function of the non-dimensional curvilinear coordinate on the pressure and suction-side surface at 50% blade height. Similar to Table 6.1 above, the average and standard deviation of all test cases are noted. The very low standard deviation indicates almost identical results for all test cases and therefore supports the aforementioned steady-state measurement basis for combining and comparing the test cases with each other. In addition to Tables 6.2 and 6.3 shows Figure 6.1 the blade surface isentropic Mach-numbers of the individual test cases. It can be identified that all test cases have identical profiles. In Appendix A.1 the blade surface isentropic Mach-numbers for 25% blade-height (Tables A.1 and A.2 and Figure A.1) and 90% blade-height (Tables A.3 and A.4 and Figure A.2) are presented.

Non-dimensional curvilinear location on PS s [-]	Isentropic Mach-number on PS	
	Average of all test cases $M_{is}$ [-]	Standard deviation [%]
0.00	0.09	2.5
0.09	0.18	3.8
0.19	0.18	2.4
0.33	0.19	1.7
0.47	0.24	1.0
0.63	0.33	0.4
0.75	0.42	0.3
0.87	0.54	0.3
1.00	0.71	1.0

**Table 6.2:** Blade surface isentropic Mach-number on PS at mid-span (50% blade-height).

Non-dimensional curvilinear location on SS s [-]	Isentropic Mach-number on SS	
	Average of all test cases $M_{is}$ [-]	Standard deviation [%]
0.07	0.49	0.4
0.15	0.60	0.5
0.23	0.68	0.6
0.32	0.74	0.3
0.40	0.76	0.4
0.49	0.77	0.7
0.57	0.78	0.8
0.64	0.77	0.8
0.73	0.76	0.9
0.81	0.75	1.3
0.90	0.75	1.2

**Table 6.3:** Blade surface isentropic Mach-number on SS at mid-span (50% blade-height).

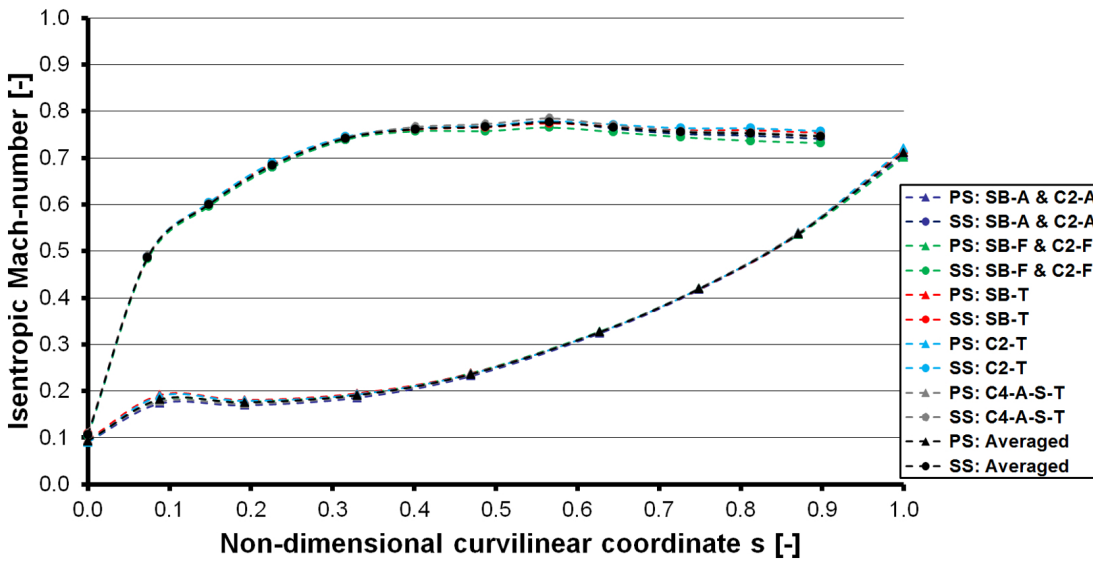


**Figure 6.1:** Isentropic Mach-number distribution along the blade surface at mid-span (50% blade-height) of all test cases.

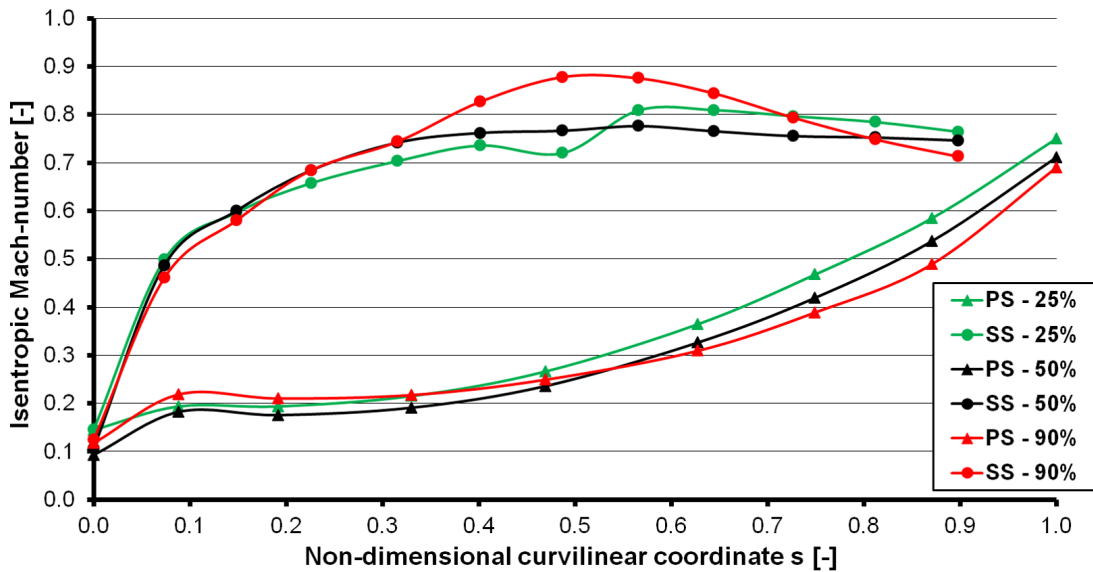


**Figure 6.2:** Averaged (for all test cases) isentropic Mach-number distribution along the blade surface for three different channel heights (25%, 50% and 90%).

In Figure 6.2, the average values of the blade surface isentropic Mach-number is visualized for all three blade heights (25%, 50% and 90%). Overall, the measurements at the three different blade heights indicate a typical turbine-blade loading pressure distribution. However, for the blade heights of 25% and 90%, humps can be identified in the distributions. These humps are related to leakage flows created either by the gaps between the individual blade bases on the hub side or by the tip-gap. In Figure 6.3, an overview of the different secondary flows is

given, the yellow and blue arrows indicating the flow at the hub region, and the red and black arrows the flow in the tip-gap region. How the tip-gap influences the flow on the pressure- and suction-side can be observed in Figure 6.4 by the graph showing the isentropic Mach-number distribution along the shroud wall surface for two pitches. It can be seen that due to the pressure differences a fluid flow from the pressure- to suction-side is present and creates a tip-gap vortex on the suction-side towards the trailing-edge. A detailed description of the different leakage flows is documented in Rottmeier [2003], whose investigations show that the observed secondary flow effects along the hub and shroud region of the test section do not affect the mid-channel flow. Hence, a quasi two-dimensional flow can be considered in this region. These conclusions of Rottmeier [2003] are assumed to be valid, since the same turbine cascade configuration was used and almost identical flow conditions were applied. A comparison of the steady-state flow conditions between this work and those of Rottmeier [2003] is documented in Appendix A.2.

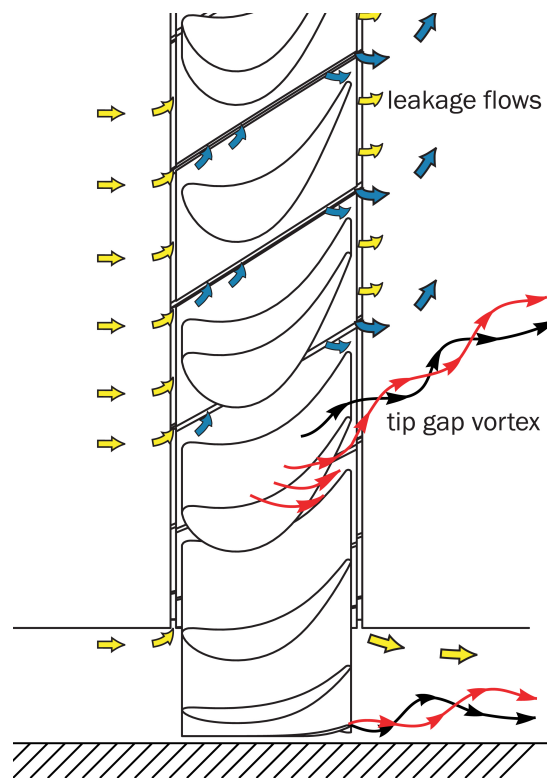


**Figure 6.3:** Schematic view of the secondary flow (from Rottmeier [2003]).

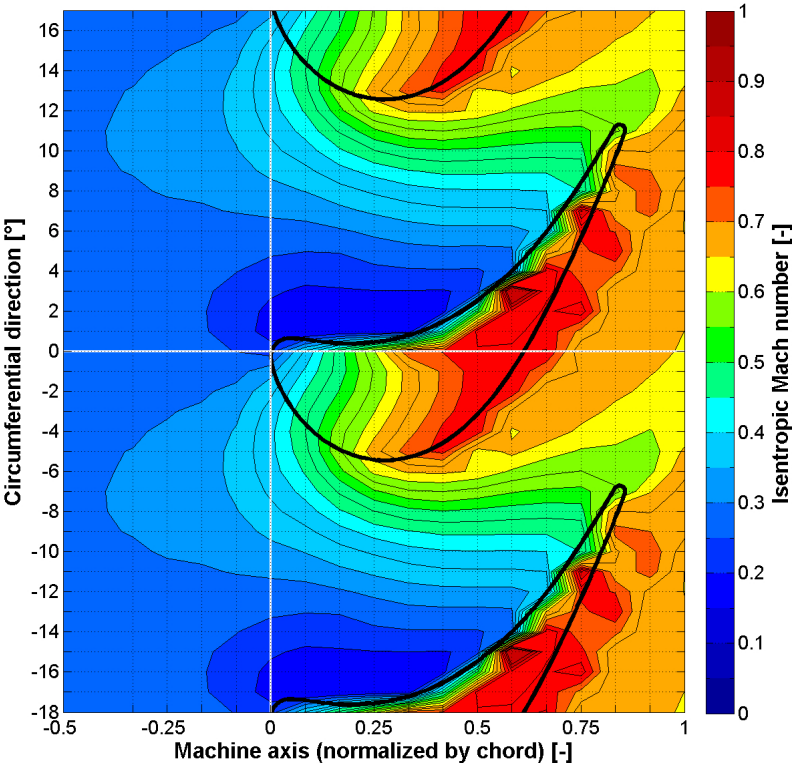


Figure 6.4: Isentropic Mach-number distribution along the outer wall (tip).

## 6.3 Summary on Steady-State Measurement Results

Considering the steady blade- and shroud-surface and probe measurements, the following main findings can be recapitulated:

- Close to identical flow conditions are achieved for all investigated test cases, allowing a comparison of the different test cases.
- The average Mach-numbers of all test cases (single-blade and cluster) are  $M_1 = 0.34$  at the inlet and  $M_2 = 0.69$  at the outlet.
- The average flow angles of all test cases (single-blade and cluster) are  $\beta_1 = 46^\circ$  at the inlet and  $\beta_2 = -57.9^\circ$  at the outlet.
- The blade surface is exposed to subsonic flow conditions typical for a turbine-blade loading at mid-channel (50% blade height).
- Along the hub and shroud region, secondary flows are observed but do not influence the flow at mid-channel height. Therefore a quasi two-dimensional flow can be considered in this region.



## 7 Time-Resolved Results and Aerodynamic Stability Analysis

THIS chapter is dedicated to the investigation of the aerodynamic stability of the different cluster test cases. The main structure is as follows:

- Single-blade reference test cases with a different oscillation direction per test case
  - SB-A (axial-bending oscillation direction)
  - SB-F (flap-bending oscillation direction)
  - SB-T (torsion oscillation direction)
- Two-blade cluster test cases with varying oscillation directions per test case
  - C2-A (axial-bending oscillation direction)
  - C2-F (flap-bending oscillation direction)
  - C2-T (torsion oscillation direction)
- Four-blade cluster test case (C4-A-S-T) which simulates a torsional oscillation direction of the cluster by imposing an individual cluster-blade oscillation in the axial-bending direction
- Prediction of the aerodynamic parameters of individual cluster-blades by using aerodynamic data of single-blades as input
  - Two-blade cluster test case C2-A (axial-bending oscillation direction)
  - Four-blade cluster test case C4-A-S-T (axial-bending oscillation direction of the cluster-blades simulating a torsional oscillation of the cluster)

In addition to the summary above of the test cases, a detailed description of the measured clusters is presented in Chapter 4. The associated steady-state flow conditions are discussed in Chapter 6. For the aerodynamic stability analysis, the following parameters are of main interest: the local aerodynamic work coefficient and the global aerodynamic damping coefficient. The first one is used to identify the local regions on the blade surface which influence the aerodynamic stability. The second one, the global aerodynamic damping coefficient, is used to assess whether the individual blade of the test case is aerodynamically stable or unstable. Both parameters are based on the unsteady pressure coefficient amplitude and phase, which will also be used to discuss aerodynamic effects in certain test cases. In Section 2.5, the aforementioned parameters are described in detail.

In order to visualize the parameters previously mentioned, a type of diagram is used which is of similar structure, except for the data included. Prior to the analysis of the different test cases, the structure of this type of diagram is described, using as an example the unsteady pressure coefficient amplitude in Figure 7.1 on the left. The x-axis denotes the non-dimensional curvilinear coordinate  $s$  along the blade surface. The trailing-edge (TE) is indicated by  $s = \pm 1$  and the leading-edge (LE) by  $s = 0$ . The pressure-side (PS) is represented by positive non-dimensional curvilinear coordinates and the suction-side (SS) by the negative. The exact locations of the pressure measurement positions can be consulted in Figure 3.8 and Table 3.2. They are indicated by dashed lines within the figure. Along the y-axis, either the inter-blade phase angle (IBPA) or the inter-cluster phase angle (ICPA) is displayed. Each phase angle is indicated within the figure by dashed lines. For single-blade test cases the y-axis ranges from an inter-blade phase angle of  $-180^\circ$  to  $+180^\circ$ , with both being identical due to the sine identity. In the case of cluster test cases, the range of the y-axis is adjusted to the inter-cluster phase angle, which depends on the number of clusters in the cascade (blade-row) (see Equation 2.5). Each x/y-crossing of the aforementioned dashed lines represents a measurement location. The coloring in each figure is dedicated to the value presented and detailed within the analysis.

## 7.1 Single-Blade Reference Test Cases

Three single-blade reference test cases are analyzed in the following. An overview of the principal unsteady parameters is presented in Table 7.1. It can be noted that very similar reduced frequencies are achieved for the different test cases. The minor differences are due to the slightly different blade excitation frequencies, as well as to minor variations in the steady-state flow conditions. The variation in the selected vibration frequencies is related to the vibration control system. Due to the different oscillation directions interacting with the flow, the excitation frequencies had to be adjusted in order to excite all blade vibration systems with the same blade vibration amplitude.

Case	Vibration frequency	Bending vibration amplitude	Torsional vibration amplitude	Reduced frequency
	$f$ [Hz]	$\hat{a}_h * 10^{-6}$ [m]	$\hat{a}_\alpha * 10^{-3}$ [°]	
SB-A	261	68	-	0.26
SB-F	270	44	-	0.27
SB-T	259	-	75	0.25

**Table 7.1:** Unsteady measurement specifications of the single-blade test cases

In Figure 7.1 on the left, the unsteady pressure amplitude for the single-blade test case SB-A vibrating in an axial-bending vibration direction is displayed for all inter-blade phase angles.



## 7.1. Single-Blade Reference Test Cases

In order to identify the influence of different inter-blade phase angles onto the unsteadiness around the blade, the distributions along the blade surface are compared between the different inter-blade phase angles. For this purpose, the chord-wise distribution with the highest peak is used as a reference for comparison, which can be observed for an inter-blade phase angle of  $\sigma_\lambda = 162^\circ$ . In a next step by varying the inter-blade phase angle in both directions (positive and negative) and comparing each of the chord-wise distributions to the reference distribution, a decrease in the unsteady pressure amplitude can be observed. Its minimum level is found at about an inter-blade phase angle of  $\sigma_\lambda = 0^\circ$ .

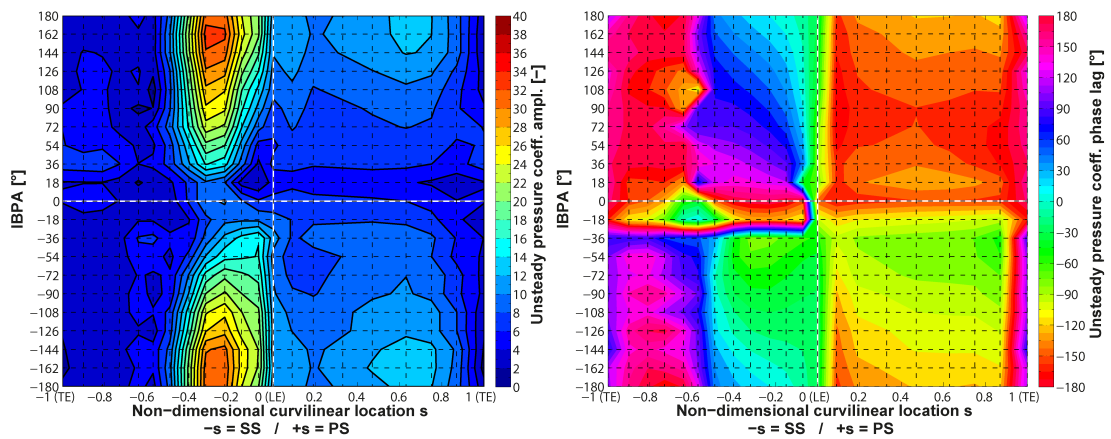


**Figure 7.1:** Unsteady pressure coefficient amplitude (left) and phase lag (right) of the single-blade test case SB-A (axial-bending oscillation direction).

A similar observation can be made for the test case with a torsional oscillation direction (SB-T) presented in Figure 7.2 on the left, whereas the peak value in this case is present for an inter-blade phase angle of  $\sigma_\lambda = -126^\circ$  and the minimum level is reached for an inter-blade phase angle of  $\sigma_\lambda = 18^\circ$ .

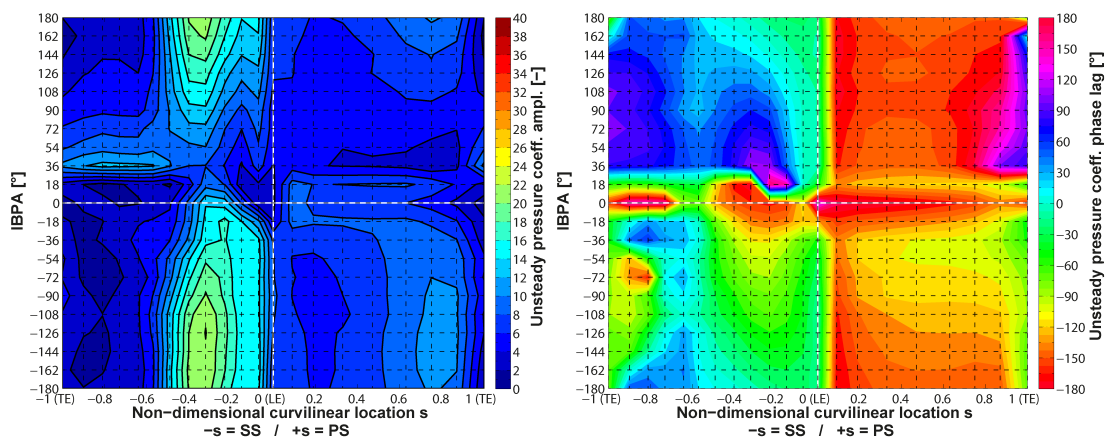


**Figure 7.2:** Unsteady pressure coefficient amplitude (left) and phase lag (right) of the single-blade test case SB-T (torsion oscillation direction).

The aforementioned effects are based on the movement of the blades with different inter-blade phase angles. In Figure 7.3, this is illustrated exemplarily for an inter-blade phase angle of  $\sigma_\lambda = \pm 180^\circ$ . It can be seen that the positions of two consecutive neighboring blades oscillate so that they are either closest together or farthest away. Hence, the throat of an inter-blade channel is either the smallest or largest and the highest unsteady pressure amplitudes are usually discovered in this region of inter-blade phase angles. It can be stated that this effect has a great influence on the unsteady pressure distribution. As previously noted, because of other effects which also influence the unsteadiness around the blade, the peak values are observed at an inter-blade phase angle different to  $\sigma_\lambda = \pm 180^\circ$ . These are the influences of the neighboring blades, the oscillation direction of the blade, the flow conditions and the curvature of the blade.

As highlighted in the previous paragraph, the curvature of the blade as well as the flow influences the unsteady pressure amplitude. To illustrate this, a reference distribution in the chord-wise direction for an inter-blade phase angle of  $\sigma_\lambda = 162^\circ$  is used again (in Figure 7.1 on the left). Along the suction-side, it can be seen that the increase starts close to the leading-edge and ends at about mid-chord. Identifying this surface area at the blade profile (see Figure 3.8) shows the highest curvature for this particular region. Hence, an acceleration of the flow is given (see the isentropic Mach-number distribution in Figure 6.2) which increases the susceptibility to flow disturbances due to the blade motion. Continuing further towards the trailing-edge, the curvature of the blade flattens and less unsteadiness occurs. Along the pressure-side a nearly consistent blade profile curvature is present and thus the variation of the unsteady pressure amplitude is smooth too. For the test case with a torsion oscillation direction SB-T, similar observations can be made.

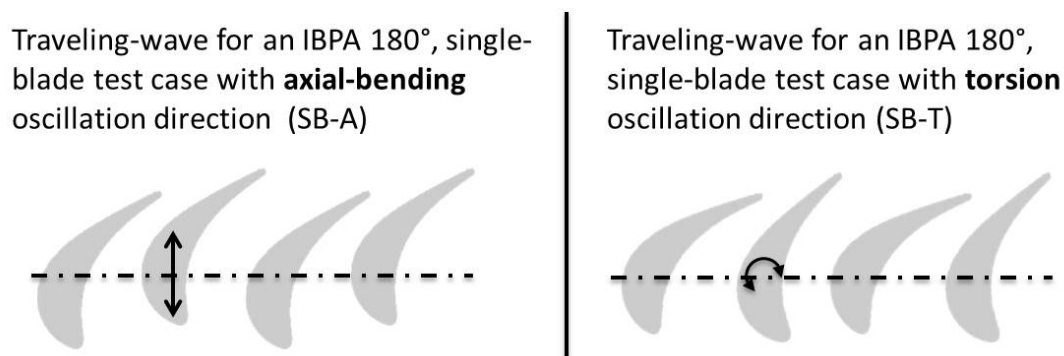


**Figure 7.3:** Schematic example of a single-blade traveling-wave for an inter-blade phase angle of  $\sigma_\lambda = \pm 180^\circ$ . On the left: SB-A (axial-bending oscillation direction) and on the right: SB-T (torsion oscillation direction).

In Figure 7.1 on the right, the unsteady pressure coefficient phase shift is displayed for the single-blade test case SB-A, vibrating in an axial-bending oscillation direction. In Figure 7.2 on the right, the unsteady pressure coefficient phase shift of the torsion oscillation direction is shown. The documented phase lag is calculated between the individual unsteady pressure

transducer signal at blade mid-span and the blade displacement signal of the blade carrying the individual unsteady pressure transducer. Some step changes in coloring are possible and are related to the fact that the interpolation used for scaling does not account for the sine periodicity, stating that a phase angle of  $-180^\circ$  is equal to  $+180^\circ$ . As expected, the inter-blade phase angle has a noticeable impact on the appearance of the flow unsteadiness, which relates to the blade motion. The pressure-side shows overall, for both test cases, that the appearance of the unsteady pressure is lagging behind the blade motion, which is indicated by a negative phase-angle. Furthermore, a rather uniform distribution in the chord-wise direction can be identified. In contrast, the suction-side shows a less uniform distribution with varying inter-blade phase angles thus expecting varying aerodynamic work contributions.

With respect to the unsteady pressure amplitude and phase shift distribution of the test case SB-F with a flap-bending oscillation direction, similar observations can be identified as for the axial-bending oscillation direction test case (SB-A). For completeness, both distributions can be seen in Appendix A.3.

The previous part of this section analyzed the results of the unsteady pressure coefficient. It could be seen that the inter-blade phase angle and the blade curvature in combination with the flow is influencing the unsteadiness around the blade. Furthermore, a strong impact of the inter-blade phase angle on the unsteady pressure coefficient phase shift was observed. The local aerodynamic work coefficient will be discussed next and is visualized in Figure 7.4. The aerodynamic work coefficient can be seen as a direct measure of the work performed on the blade. It indicates either if energy is transferred from the flow to the blade (indicated as red coloring within the plot) or areas where the pressure contributes to stabilizing the vibration. Blade vibration energy is therefore absorbed by the flow, displayed as green coloring in the figures. In order to highlight local influences, the normalization of the local work coefficients is carried out using the absolute peak value in the individual test cases.

The local aerodynamic work coefficient is calculated using the unsteady pressure coefficient amplitude and phase lag, as well as accounting for the oscillation direction of the individual test case (see Equation 2.24 for the bending oscillation direction test cases and Equation 2.25 for the torsion oscillation direction test case in Section 2.5). It can be seen from the mathematical formulations, the key parameters influencing the result of the integration over one oscillation period are the unsteady pressure coefficient phase angle and the direction in which the pressure is acting on the blade in relation to the oscillation direction.

## Time-Resolved Results and Aerodynamic Stability Analysis

---

In Figure 7.4 the local aerodynamic work coefficient is presented for each single-blade test case: at the top, test case SB-A with an axial-bending oscillation direction; in the middle, test case SB-F with a flap-bending oscillation direction; at the bottom, test case SB-T with torsion oscillation direction. Overall it can be stated that the pressure-sides for the test cases with a bending oscillation direction have a stabilizing contribution to the aerodynamic stability of the blade. In contrast, the suction-sides show varying distributions. For the test case with a torsion oscillation direction, varying distributions are present for both blade-sides. As noted perviously, these variations are mainly influenced by the unsteady pressure coefficient phase shift combined with the oscillation direction.

An influence only of the oscillation direction on the local distribution of the aerodynamic work coefficient can be observed by considering in which direction the pressure is acting on the blade surface with respect to the oscillation direction of the blade. The reason is, that any pressure fluctuations which act perpendicularly to the bending oscillation direction have no impact on the work coefficient (see Equation 2.24). For the torsion oscillation direction, this is the case when the pressure fluctuation acts in a direction so that it crosses the rotation axis of the blade and thus has no impact due to the moment-of-force (see Equation 2.25). In order to identify these areas on the blade surface, the relation between the oscillation direction and the acting pressure direction on the blade surface have to be considered. The oscillation directions are shown in Figure 4.1 and the curvature of the blade sides in Figure 3.8. For the three test-cases, the following areas having a minimum local aerodynamic work coefficient can be seen:

- Axial-bending oscillation direction SB-A: on the suction-side from  $s = -0.35$  to  $s = -0.25$  and on the pressure-side from  $s = 0.1$  to  $s = 0.2$ .
- Flap-bending oscillation direction SB-F: on the suction-side from  $s = -0.2$  to  $s = -0.05$  and none on the pressure-side.
- Torsion oscillation direction SB-T: on the suction-side from  $s = -0.6$  to  $s = -0.5$  and on the pressure-side from  $s = 0.3$  to  $s = 0.4$ .

It should be noted that these areas, as previously described for the different oscillation directions, are used in the following sections of this chapter to describe aerodynamic effects observed by cluster test cases.

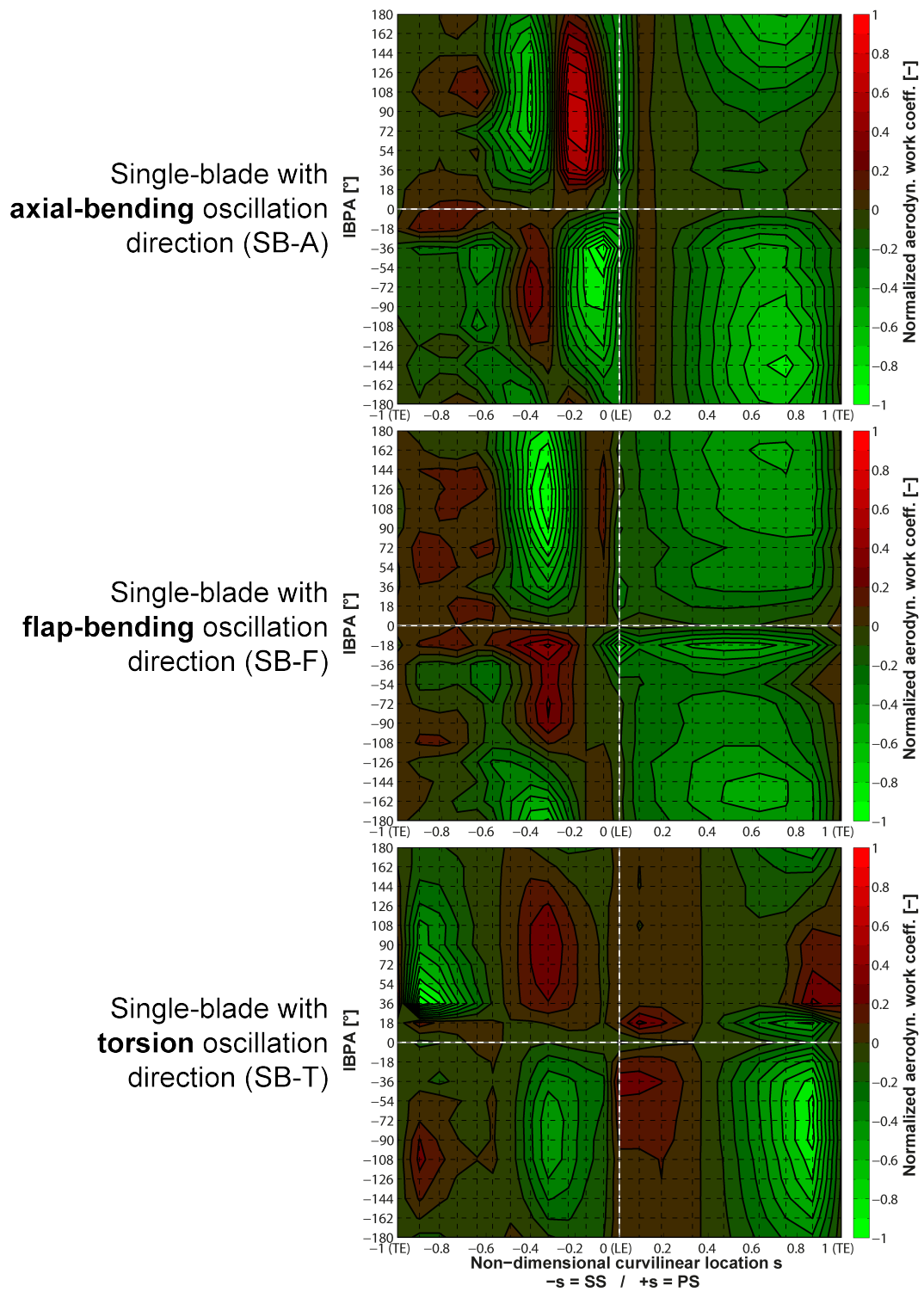


**Figure 7.4:** Normalized local aerodynamic work coefficient of the single-blade test cases. Top: SB-A (axial-bending oscillation direction), middle: SB-F (flap-bending oscillation direction) and bottom: SB-T (torsion oscillation direction).

Up to now the blade-row is observed with all blades vibrating in the traveling-wave formulation. In order to identify the influence of one blade on another, the local work coefficient is transformed into influence coefficients. This is done by first transforming the unsteady pressure coefficient from the traveling-wave formulation to the influence coefficient formulation and then calculating the local and global work coefficients. The related mathematical formulations are detailed in Section 2.3. In Figure 7.5 on the left, the local work coefficient transformed into influence coefficients is individually presented for all test cases (top: SB-A, middle: SB-F and bottom: SB-T). The bars in the right diagram represent the global aerodynamic work coefficient. In contrast to the graphs for the traveling-wave formulation, the y-axis represents the blade number instead of an inter-blade phase angle. The coloring of the local work coefficient in these distributions is identical to those of the traveling-wave formulation. The normalization is calculated by using the absolute peak value of the individual test case. Identical to the distributions in traveling-wave formulation, the local work oscillation direction axis can be identified by the zero values of the local work coefficient at the respective chord-wise coordinates as highlighted in the previous paragraph. In addition shows Figure 7.6 the influence coefficients for all test cases representing the global aerodynamic work coefficient. Within this figure the normalization of all test cases is performed using the absolute peak value of the test case with flap-bending oscillation direction (SB-F), thus enabling a comparison between the test cases. It should be noted that a negative work coefficient represents a stabilization of the blade vibrations.

Overall it can be seen that the influence of the reference blade 0 on itself is stabilizing as it is indicated by the green coloring along the blade surface. It can also be observed that the neighboring blades of the test cases with a bending oscillation direction have a significant influence on the reference blade. Previous research identified similar tendencies, for example Hanamura et al. [1980] and Crawley [1988]. Furthermore, this influence is greater for the blades in the pressure-side direction (positive blade numbering) than for those in the suction-side direction (negative blade numbering). For the test case with a torsional oscillation direction this is not the case. Here, the neighboring blades in both directions show similar influences on the reference blade. The comparison of the test cases with a bending oscillation indicate that the direct neighbors have a different influence on the reference blade. Since the flow conditions for both test cases are identical, this difference is mainly induced by the bending oscillation. The influence coefficients presented previously are compared qualitatively to those found in Panovsky and Kielb [2000]. The latter used influence coefficients to predict the impact of a varying torsion axis location on the aerodynamic stability. As a basis of this prediction, they used similar oscillation directions (flap-bending and torsion) to those in the present work, which were applied on a thin and strongly curved turbine-blade profile. Furthermore, they used similar reduced frequencies. The comparison showed similar tendencies in terms of the order of magnitude of the influence coefficients for the different test cases.

## 7.1. Single-Blade Reference Test Cases

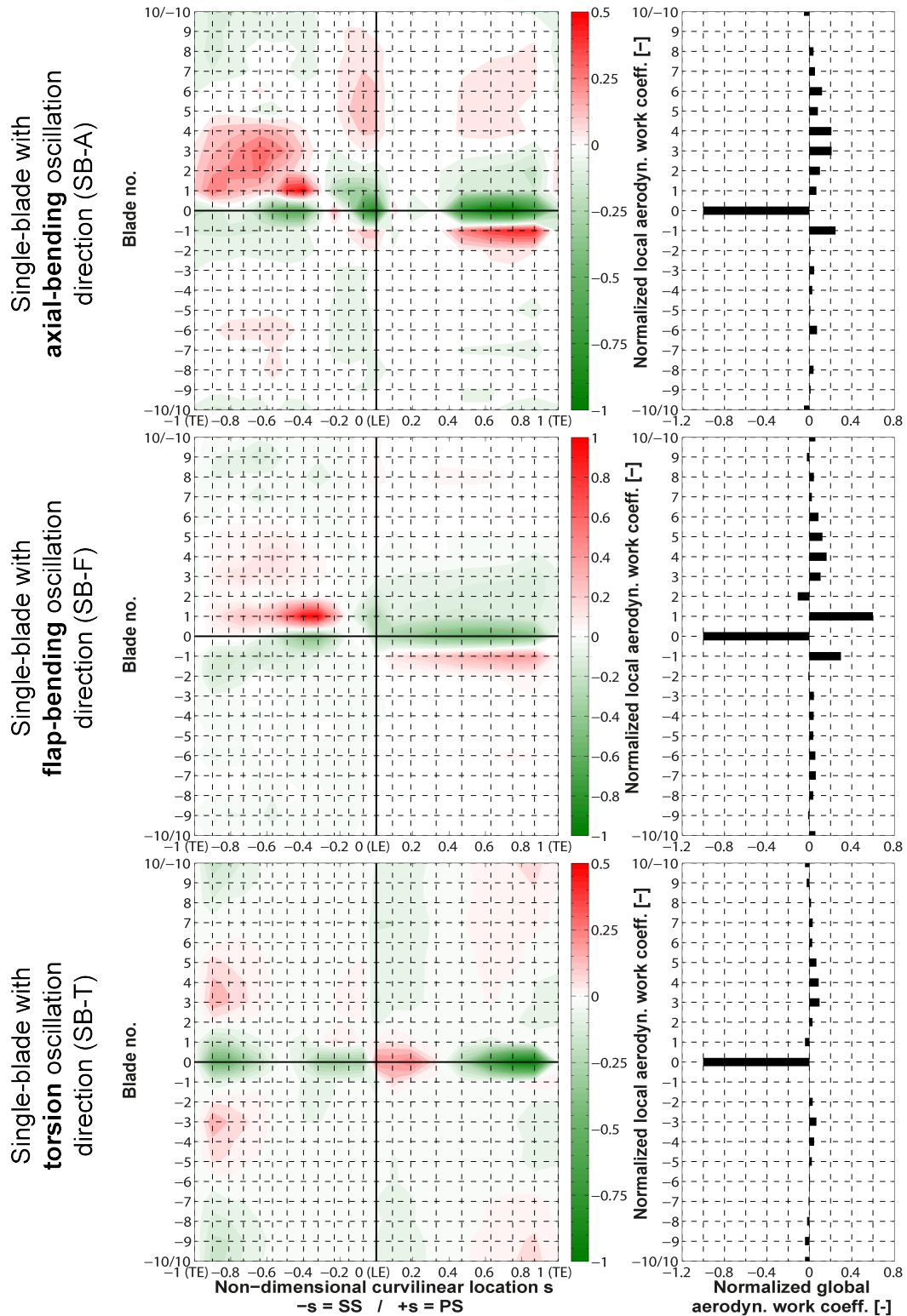


**Figure 7.5:** Influence coefficient of the normalized aerodynamic work coefficient of the single-blade test cases. Top: SB-A (axial-bending oscillation direction), middle: SB-F (flap-bending oscillation direction) and bottom: SB-T (torsion oscillation direction).

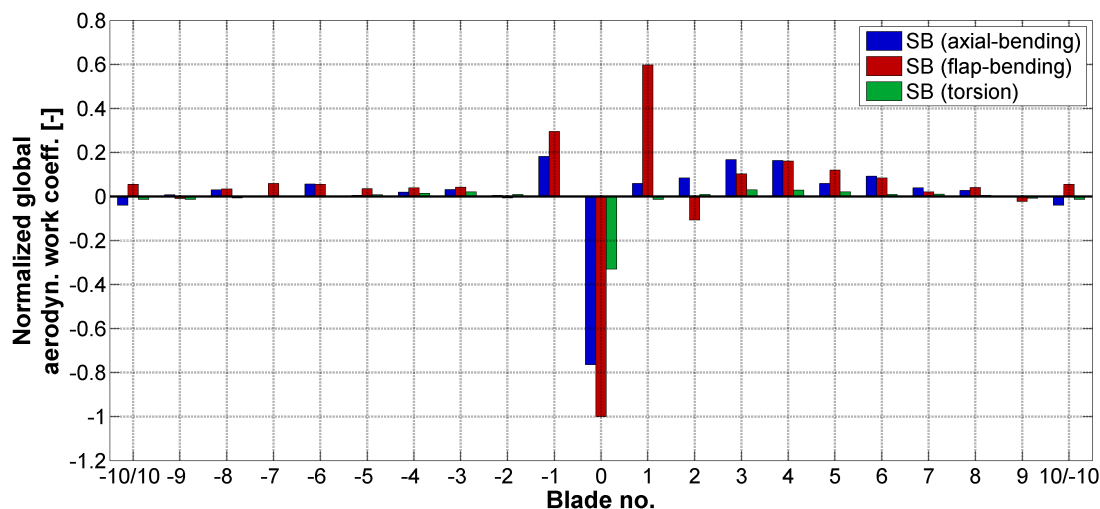


**Figure 7.6:** Influence coefficient of the normalized global aerodynamic work coefficient of the single-blade test cases, SB-A, SB-F and SB-T.

The local work coefficient, indicates the local contributions of stabilizing or destabilizing blade surface sections. Integrating these values leads to the global aerodynamic work coefficient, which is then used to determine the global aerodynamic damping coefficient as described in Section 2.5 (see Equation 2.29 and 2.30). A positive global aerodynamic damping coefficient indicates an aerodynamic stabilization. In Figure 7.7 the global aerodynamic damping coefficient is presented for all three test cases including the corresponding confidence intervals of the random error. The presented values are normalized using the highest damping value of the three test cases, which is the flap-bending oscillation direction test case (SB-F). It can be observed that all three test cases have a positive contribution for all inter-blade phase angles. Hence, it can be stated that all are aerodynamically stable. For the bending test cases the minimum can be observed for an inter-blade phase angle of  $\sigma_\lambda = 0^\circ$  and, for the torsion test case, for an inter-blade phase angle of  $\sigma_\lambda = 90^\circ$ .

In order to validate the test results, comparisons of the global aerodynamic work coefficient were performed with other researchers. Rottmeier [2003] focused his investigations on the superposition of gust response and traveling-wave measurements for a single-blade test case with a torsion oscillation direction. Next to the superimposed measurement results, only traveling-wave results were documented. As the steady-state flow conditions are similar to this work (see Appendix A.2), the comparison of the global aerodynamic damping coefficients between this work and Rottmeier [2003] showed almost identical distributions<sup>1</sup>.

Furthermore, a qualitative comparison was carried out with the work of Panovsky and Kielb [2000]. As previously noted, similarly oscillation directions were used (flap-bending and torsion) to those in the present work, and were applied on a thin turbine-blade profile. Furthermore, they used similar reduced frequencies. Although the comparison showed, in principle, similar curve progressions, different global aerodynamic damping values were observed. In

<sup>1</sup>It should be remembered that the turbine-blade profile used in this work is identical to this of Rottmeier [2003]



summary it is concluded from these comparisons, that the test results of this work show typical local aerodynamic work coefficient and global aerodynamic damping coefficient distributions as is expected for this type of turbine-blade profile and flow conditions.

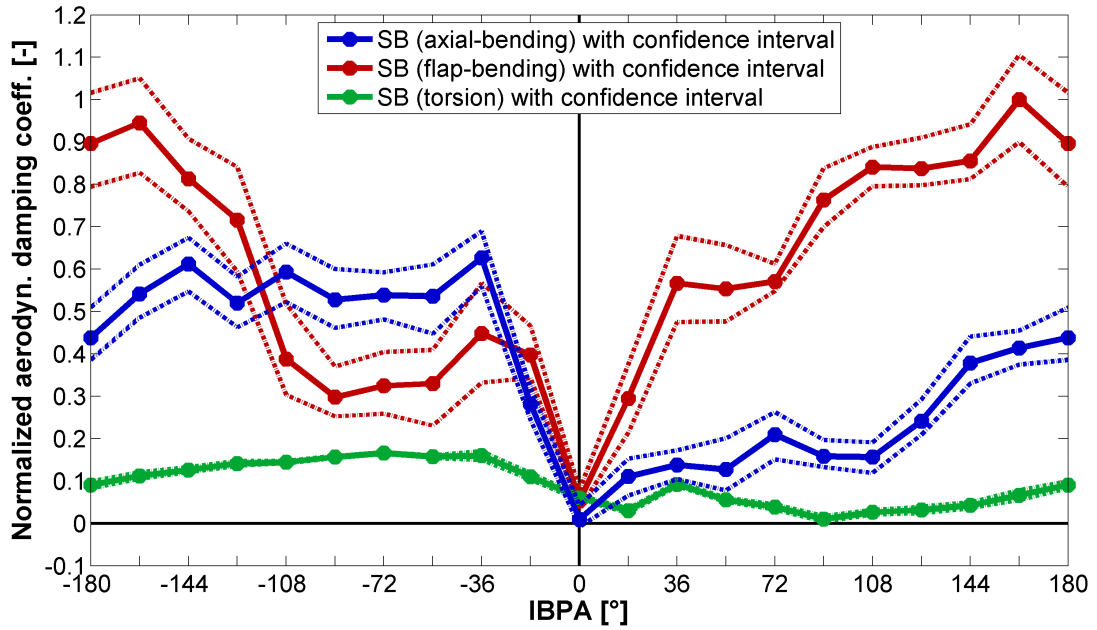


**Figure 7.7:** Normalized global aerodynamic damping coefficient of the single-blade test cases, SB-A, SB-F and SB-T. (A positive aerodynamic damping value indicates stabilization.)

### 7.1.1 Summary of Aerodynamic Stability of Single-Blade Reference Test Cases

The previous section presents the reference single-blade test cases. The main differences between the test cases are the oscillation directions of the lowest eigenmode: torsion, axial- and flap-bending. As a basis for the analysis of the cluster test cases discussed in the following sections, the characteristic aerodynamic effects related to the individual single-blade oscillation directions were highlighted and are summarized below:

- Traveling-wave formulation:
  - The parameters influencing the unsteady pressure around the blade is the inter-blade phase angle at which the blade-row is oscillating and the curvature of the blade.
  - The local distribution of the aerodynamic work is mainly influenced by the unsteady pressure coefficient phase lag and the oscillation direction.
  - Overall, the aerodynamic damping for all three test cases is positive for all inter-blade phase angles and thus aerodynamically stable operating conditions are present.
  - The test results for the flap-bending and torsion oscillation direction are qualitatively validated with other researchers (Rottmeier [2003] and Panovsky and Kielb [2000]).
- Influence coefficient formulation:
  - For the test cases with a bending oscillation direction, the immediate neighboring blades have a larger influence on the reference blade than in the torsion test case.
  - For all test cases the neighboring blades in the suction-side direction have a larger influence than those neighboring in the pressure-side direction.
  - The global distribution of the influence coefficients show similar tendencies for the test cases with flap-bending and torsion oscillation direction as known from the literature (for example see Panovsky and Kielb [2000]).

## 7.2 Cluster Test Cases

In total, four cluster test cases are presented and analyzed in this section. The difference between the individual test cases is summarized below:

- Three two-blade cluster test cases; for each cluster, both cluster-blades have identical oscillation directions. The difference between the test cases are the applied oscillation directions (torsion (C2-T), axial-bending (C2-A) and flap-bending (C2-F)).
- One four-blade cluster, which simulates a torsional movement of the cluster by individually oscillating the cluster-blades in the axial-bending oscillation direction (C4-A-S-T).

A detailed description of the different cluster test cases can be consulted in Chapter 4.

### 7.2.1 Two-Blade Cluster

This type of two-blade cluster simulates two blades which are fixed at the hub and welded together at the tip as pairs. A detailed description of this type of two-blade cluster is documented in Section 4.2. Similarly to the single-blade test cases discussed in the previous section, all three vibration directions are analyzed (axial- and flap-bending, torsion). In Figure 7.8 a schematic example is displayed showing a two-blade cluster with an axial-bending oscillation direction. The relative positions of the clusters is a snap shot for an inter-cluster phase angle of  $\Gamma_\lambda = 180^\circ$ .

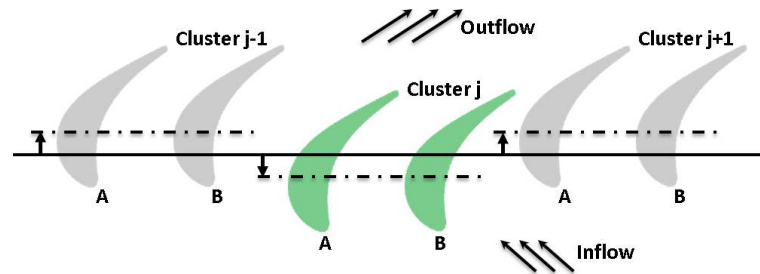


**Figure 7.8:** Example of the two-blade cluster oscillation with axial-bending direction (test case C2-A). It represents a snap shot for an inter-cluster phase angle of  $\Gamma_\lambda = 180^\circ$ . (For visualization purposes the blade displacements are exaggerated.)

## Time-Resolved Results and Aerodynamic Stability Analysis

In Table 7.2, the vibration amplitudes and the reduced frequencies are documented. Similar values as for the single-blade test cases (see Table 7.1) are aimed for and achieved in order to allow an easy comparison.

Case	Vibration frequency	Bending vibration amplitude	Torsional vibration amplitude	Reduced frequency
	f [Hz]	$\hat{a}_h * 10^{-6}$ [m]	$\hat{a}_\alpha * 10^{-3}$ [°]	k [-]
C2-A	261	67	-	0.26
C2-F	270	43	-	0.27
C2-T	259	-	75	0.25

**Table 7.2:** Unsteady measurement specifications of the two-blade cluster test cases.

In Figure 7.9, the local aerodynamic work coefficient of cluster-blade A (left) and B (right) of all three cluster test cases is presented. Below the schematic illustration of the cluster configuration, the top graphs display the results for the axial-bending vibration direction test case C2-A, the middle graphs for the flap-bending vibration direction test case C2-F and the bottom graphs for the torsional vibration direction test case C2-T. For each test case, the absolute peak value of both cluster-blades is used for normalization in order to highlight local differences.

By comparing the inner-cluster channel (between the pressure-side of cluster-blade A and the suction-side of cluster-blade B) with the outer-cluster channel (between the suction-side of cluster-blade A and the pressure-side cluster-blade B), it can be seen that less work is exchanged within the inner-cluster channel than in the outer-cluster channel. Reflecting the setup of the cluster, this effect is related to the kinematic relationship of the cluster-blades. It states that for the whole range of inter-cluster phase angles, both cluster-blades are always moving in-phase and thus the work exchanged by the flow and the blade is at a minimum in the inner-cluster channel. As shown later in this section, this can be observed in the variation of the local work coefficient impacting on the global aerodynamic stability of the individual cluster-blades.

Similar observations are made by Corral et al. [2007], who investigated the aerodynamic stability of welded-in-pair low-pressure turbine blades by solving the linearized Reynolds averaged Navier-Stokes equations on a moving grid. As in this work, the blade oscillation directions and the reduced frequency were similar, whereas a thin turbine-blade was used.

Considering only the test cases with bending oscillation direction, it can be seen that the suction-side of the individual cluster-blades is more sensitive to any blade vibration mode change than the pressure-side. This observation is based on the comparison of pressure- and suction-sides between the cluster-blades for the whole range of inter-cluster phase angles.

Furthermore it can be observed that, apart from a change in value, the local work coefficient distribution in the chord-wise direction is similar for both cluster-blades at the pressure-side. The suction-sides show contrasting behaviour. For the cluster-blades with a torsion oscillation direction, apart from the value of the local work coefficient, both blade-sides of both cluster-blades have similar distributions in the chord-wise direction.

Thus, as expected, it can be stated that the blade oscillation direction influences the interactions between the cluster-blades. This observation is in-line with the literature (see for example Corral et al. [2007]).

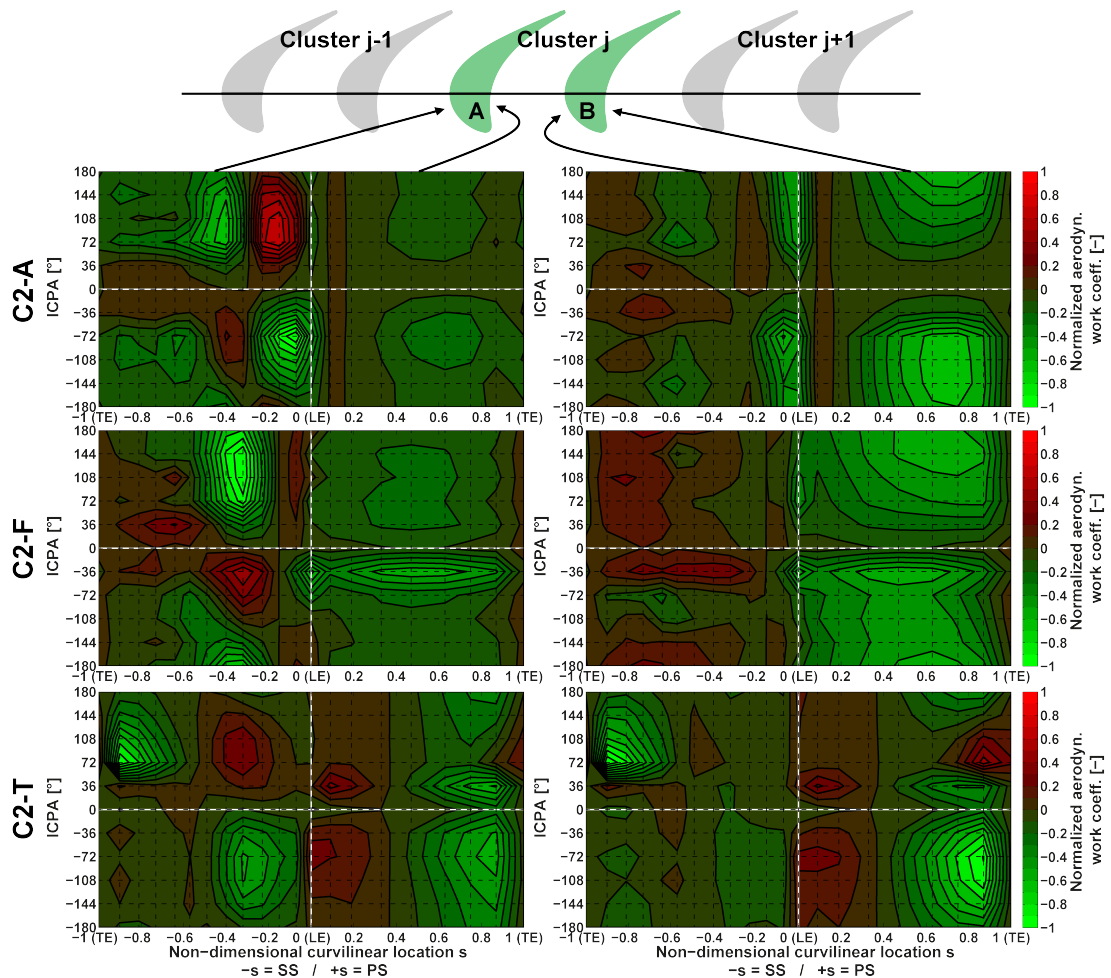


**Figure 7.9:** Normalized local aerodynamic work coefficient of cluster-blade A (left) and B (right) of the two-blade cluster cases. Top: axial-bending oscillation direction (C2-A), middle: flap-bending (C2-F) and bottom: torsion (C2-T).

## Time-Resolved Results and Aerodynamic Stability Analysis

---

As a next step, a qualitative comparison of the local aerodynamic work coefficient between the single-blade test cases (Section 7.1) and the cluster test cases of this section is performed. The results of this comparison are summarized as follows:

- high similarity between the suction-side distribution of cluster-blade A and the respective single-blade test case
- high similarity between the pressure-side distribution of cluster-blade B and the respective single-blade test case
- low similarity between the pressure-side distribution of cluster-blade A and the respective single-blade test case
- almost no similarity between the suction-side distribution of cluster-blade B and the respective single-blade test case, except for the cluster test case with torsion vibration direction, which has a low similarity to the respective single-blade test case

The previous comparison indicates that a relationship between the respective single-blade and cluster test cases exists. This can be illustrated by the following simplified example: two blade-rows are considered: blade-row X with 10 blades and blade-row Y with 20 blades. For both blade-rows a similar oscillation pattern is considered, for example the first nodal diameter. Thus, by definition of the traveling-wave formulation (see Section 2.2), blade-row X would oscillate with an inter-blade phase angle of  $\sigma_{\lambda=1} = 36^\circ$  and blade-row Y with an inter-blade phase angle of  $\sigma_{\lambda=1} = 18^\circ$ . The analogy to the present cluster test cases is made by considering that each blade in blade-row X would represent a two-blade cluster. It should be stated that only the outer-cluster channel can be qualitatively illustrated with this example. As this analogy excludes the influences of the second, third and farther distant neighboring blades, the relationship between traveling-wave and influence coefficient formulation may be used to predict the aerodynamic parameters of individual cluster-blades by using single-blade input data. Later in this chapter this attempt is presented.

The global aerodynamic damping coefficient is presented in Figure 7.10 for the three two-blade cluster test cases discussed in this section. The graphs on the left show the aerodynamic damping coefficient per cluster-blade and on the right per cluster blade-channel (inner- and outer-cluster channel). The graphs at the top represent the two-blade cluster with an axial-bending oscillation direction, in the middle with a flap-bending and at the bottom with a torsion. In each graph, the respective single-blade test case is included and used for normalization. Furthermore, the average of both cluster-blades including the confidence interval is presented.

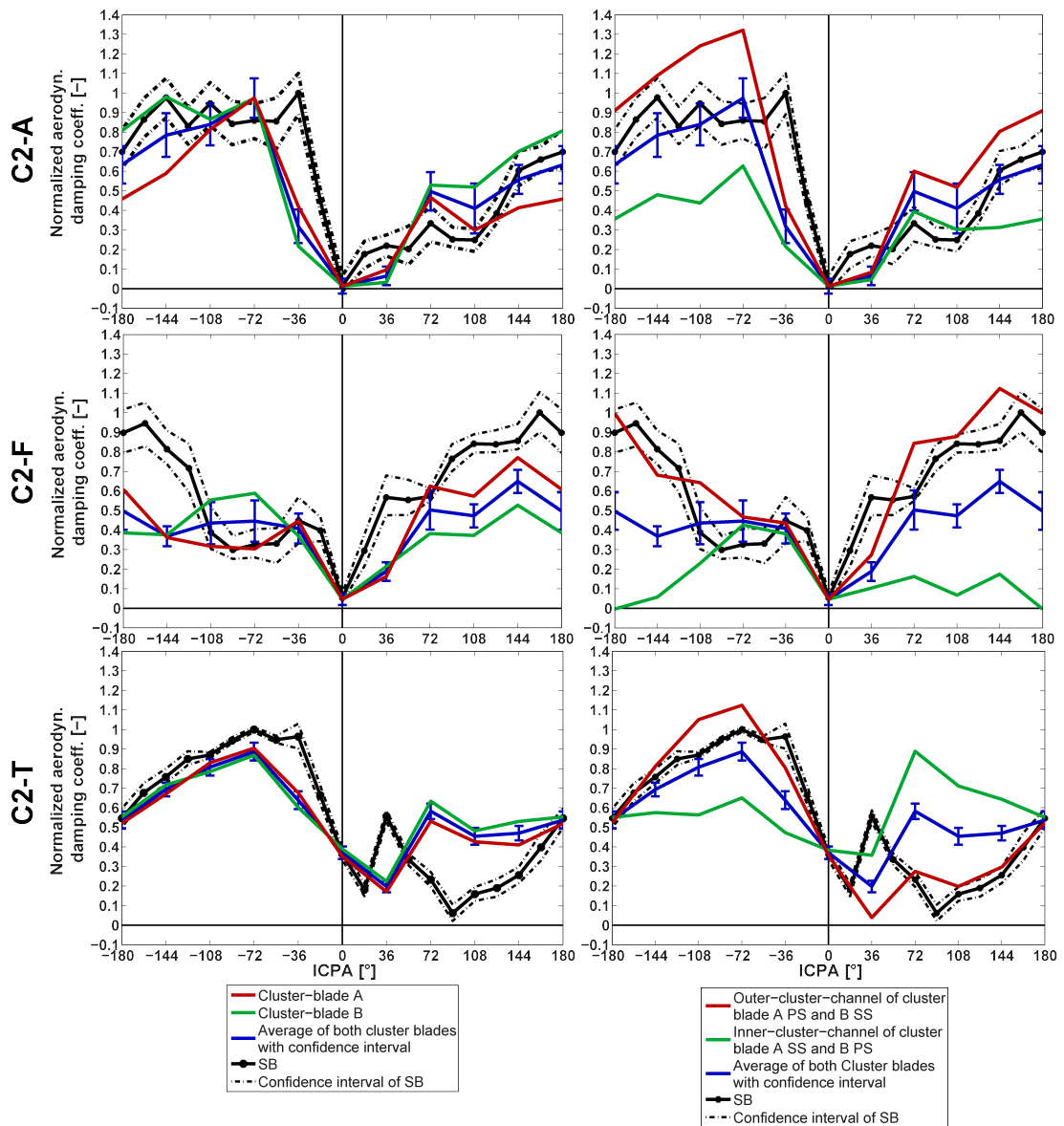


**Figure 7.10:** Normalized global aerodynamic damping coefficient of the two-blade cluster test cases. Left column: all curves represent a blade, right column: all curves represent a blade-channel. Top: axial-bending oscillation direction (C2-A); middle: flap-bending oscillation direction (C2-F); bottom: torsion oscillation direction (C2-T).

In general the positive effect of the two-blade cluster can be seen as the increase of the minimum stability over all inter-cluster phase angles. This can be observed for the test case with a torsion vibration direction. For the bending oscillation direction test cases this is not possible due to the following reasons: the minimum damping of the single-blade test case is found for an inter-blade phase angle  $\sigma_{\lambda=1} = 0^\circ$  (for the torsion vibration direction  $\sigma_{\lambda=1} = 90^\circ$ ) and the oscillation pattern of the single-blade test case is identical to the cluster for an inter-blade phase angle  $\sigma_{\lambda=1} = 0^\circ$  (also for the cluster test-case with torsion oscillation

direction). However, and as stated previously, the oscillation direction of the cluster-blades has a significant influence on the stabilizing behaviour of the cluster.

Similar observations as for the test case with a torsion oscillation direction are found in the literature (see for example Corral et al. [2007]). The numerical investigations of Corral et al. [2007] also included test cases with bending oscillation directions for which only slight improvements of the minimum aerodynamic damping were observed.

As noted before, the inner- and outer-cluster channels influence the behaviour of the cluster differently. This is due to the kinematics of the cluster oscillation. As both blades move in-phase, less unsteadiness of the flow is present in the inner-cluster channel. Thus low aerodynamic damping values are present, which can be observed as green curves in the graphs on the right in Figure 7.10. For the outer-cluster channel (present between two consecutive clusters) the unsteadiness of the flow is higher, which is a result of the relative blade oscillations defined by the inter-cluster phase angles. Thus variations of the aerodynamic damping values as a function of the inter-cluster phase angle are present and can be observed as red curves. Additionally, it can be seen that the curve profile of the outer-cluster channel has a close similarity to the respective single-blade test cases. This is in line with the previous observations for the local aerodynamic work coefficient.

For the test-case with torsional oscillation direction it can be observed that both cluster-blades have an almost an identical damping curve. Thus it can be concluded that the lower unsteadiness in the inner-cluster channel influences similarly the global aerodynamic damping of both cluster-blades. Furthermore it can be seen that differently to the bending cases the cluster increases the damping of the inner-cluster channel with respect to the outer-cluster channel for positive inter-cluster phase angles. The opposite can be observed for negative inter-cluster phase angles.





**7.2.2 Four-Blade Cluster Simulating Torsion**

This section presents the aerodynamic results of the four-blade cluster test case (C4-A-S-T). First the local work coefficient for each cluster-blade is investigated, followed by the global aerodynamic damping coefficient. As noted previously (see Section 4.3), the blades of the cluster test case vibrate in the bending oscillation direction and simulates a torsional cluster motion of a vane package composed of four blades. This is achieved by vibrating each cluster-blade in an axial-bending oscillation direction and by individually controlling the blade vibration amplitude and phase angle. The unsteady measurement specifications are displayed in Table 7.3. It should be noted that due to restrictions in the blade vibration control system, the vibration amplitudes of the inner-cluster blades do not represent exactly a third of the outer-cluster blades. As they are smaller than the nominal value, it is assumed that the unsteady pressure level is lower than as it would be in the nominal case. In the following analysis of the four-blade cluster, this difference in the blade vibration amplitude is assumed to be negligible.

Case	Vibration frequency	Bending vibration amplitude	Reduced frequency
	f [Hz]	$\hat{a}_h * 10^{-6}$ [m]	k [-]
C4-A-S-T	259	Outer: 71 Inner: 17	0.26

**Table 7.3:** Unsteady measurement specifications of the four-blade cluster test case.

Preliminary to the aerodynamic stability analysis, the kinematics between neighboring cluster-blades in the cluster are summarized. In the case of a four-blade cluster, there are four combinations of neighboring cluster-blades. It should be noted that the documented cluster-blades and -channels can be inspected in Figure 7.11.

- 1.) cluster-blade D of cluster  $j - 1$  and suction cluster-blade A of cluster  $j$ :
  - The inter-blade channel created by the pressure-side of cluster-blade D and by the suction-side of cluster-blade A is further referred to as the outer-cluster channel.
  - The phase-angle variation depends on the inter-cluster phase-angle, since these adjacent blades are related to different clusters.
  - Both blades have an identical vibration amplitude.
  
- 2.) cluster-blade A and cluster-blade B, both of cluster  $j$ :
  - The inter-blade channel created by the pressure-side of cluster-blade A and by the suction-side of cluster-blade B is further referred to as inner-cluster channel.

- Both blades are always moving in the same direction, thus they have an inter-blade phase-angle of  $\sigma_\lambda = 0^\circ$ .
  - Both blades have different vibration amplitudes (cluster-blade A > cluster-blade B, proportion  $\hat{a}_h$  vs.  $\hat{a}_h/3$ ).
- 3.) cluster-blade B and cluster-blade C, both of cluster  $j$  (inner-cluster channel):
- The inter-blade channel created by the pressure-side of cluster-blade B and by the suction-side of cluster-blade C is further referred to as the inner-cluster channel.
  - Both blades are always moving in the opposite direction, thus they have an inter-blade phase-angle of  $\sigma_\lambda = 180^\circ$ .
  - Both blades have identical vibration amplitudes.
- 4.) cluster-blade C and cluster-blade D, both of cluster  $j$  (inner-cluster channel):
- The inter-blade channel created by the pressure-side of cluster-blade C and by the suction-side of cluster-blade D is further referred to as the inner-cluster channel.
  - Both blades are always moving in the same direction, thus they have an inter-blade phase-angle of  $\sigma_\lambda = 0^\circ$ .
  - Both blades have different vibration amplitudes (cluster-blade C < cluster-blade D, proportion  $\hat{a}_h/3$  vs.  $\hat{a}_h$ ).

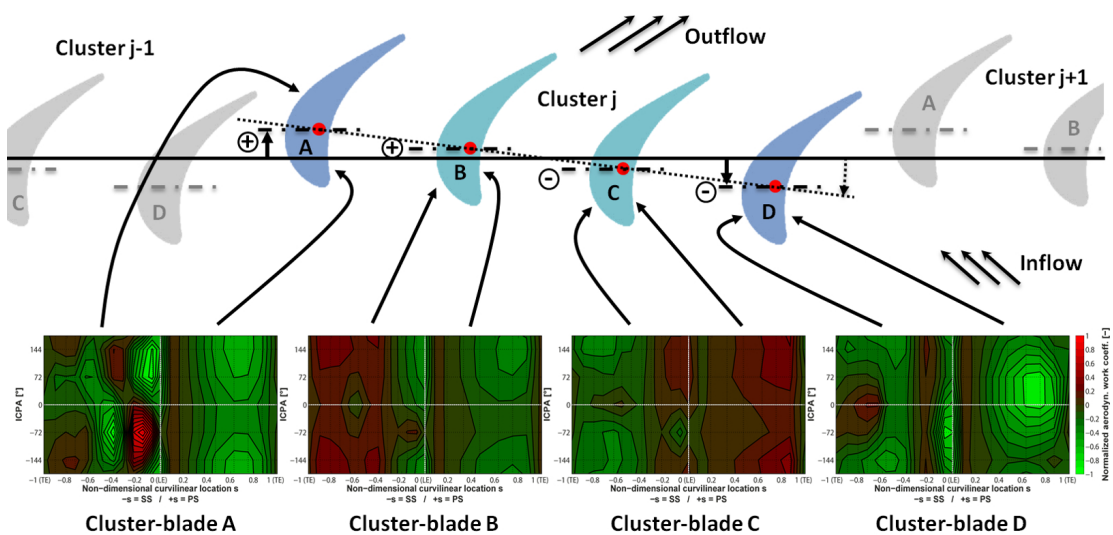


**Figure 7.11:** Overview of the four-blade cluster displaying the normalized local aerodynamic work coefficient next to the schematically displayed cluster-blades. (It should be noted that Figures 7.12 to 7.15 show identical local work coefficient distributions more in detail).

In the following, the local aerodynamic work coefficient is presented in two steps. First, an overview is displayed of all four cluster-blades in Figure 7.11. Second, the local aerodynamic work coefficient distribution is presented as a pair of cluster-blades showing the individual

inter-blade channel of the cluster (Figures 7.12 to 7.15). The local aerodynamic work coefficient (see Equation 2.24) is calculated by using the individual cluster-blade vibration amplitudes and is then normalized using the absolute peak value of the four cluster-blades. The absolute peak value can be observed at the suction-side of cluster-blade A as the positive value for an inter-cluster phase angle of  $\Gamma_\lambda = -72^\circ$ .

In the following analysis, cluster-specific aerodynamic effects are detailed. Additionally to refer them to the respective local aerodynamic work coefficient, they are also referred to the global aerodynamic damping coefficient, presented in Figure 7.16. This figure consists out of two graphs. One displays each cluster-blade surface distribution and the other each cluster-blade channel distribution, as described in the text above detailing the kinematics of the cluster. Additionally to the cluster results, the result of the single-blade test case with axial-bending (SB-A) is plotted in both graphs.

In order to determine the global aerodynamic damping coefficient of the cluster, it has to be accounted for the amplitude relationship between the inner- and the outer-cluster blades. This is based on the assumption that the global aerodynamic damping coefficient of the cluster can be determined by summing up the global aerodynamic work of the individual cluster-blades. In Appendix A.4, the derivation of the global aerodynamic damping coefficient for the cluster and the individual cluster-blades is presented by taking into account the aforementioned assumption. The global aerodynamic damping coefficient for the individual cluster-blade in the four-blade cluster is defined as:

$$\Xi_{C,I} = \frac{|\hat{a}_I| W_{EI}}{|\hat{a}|^2 \pi} \quad (7.1)$$

The global aerodynamic damping coefficient for the four-blade cluster is noted as:

$$\Xi_C = \frac{1}{I_C} \sum_{I=1}^{I_C} \Xi_{C,I} = \frac{1}{I_C} \sum_{I=1}^{I_C} \frac{|\hat{a}_I| W_{EI}}{|\hat{a}|^2 \pi} = - \frac{W_C}{|\hat{a}| \pi} \quad (7.2)$$

where  $I_C$  describes the total number of cluster-blades in the cluster,  $|\hat{a}|$  the blade vibration amplitude of the outer-cluster blades, and  $|\hat{a}_I|$  the blade vibration amplitude of the individual cluster-blades, and  $W_{EI}$  the global aerodynamic work coefficient of the individual cluster-blade as described before (see Equation 2.26).

It should be noted that the global aerodynamic damping coefficients presented in Figure 7.16 are normalized using the absolute peak value of the single-blade test case. This is done in order to be consistent with similar figures presented in the previous sections.

By taking into account the kinematics of the cluster-blades, specifically the vibration amplitudes, it can be deduced that a larger amount of aerodynamic work is exchanged in the outer-cluster channel between the neighboring cluster-blades (D and A) than within the inner-cluster channels. This assumption is confirmed when comparing qualitatively the overall value of the local aerodynamic work coefficient between the inner- and outer-cluster channels (see Figures 7.11 to 7.15). From the kinematics, as referred to in the inner-cluster channels

of item 2.) and 4.), it can be deduced that the individual cluster-blade vibration amplitudes as well as the non-symmetric curvatures of the pressure- and the suction-side are the main influencing parameters. The inner-cluster channel of item 2.) is presented in Figure 7.13 and that of item 4.) in Figure 7.15.

For the inner-cluster channel of item 2.), it can be observed that the aerodynamic work on the pressure-side of cluster-blade A is stabilizing and on the suction-side for cluster-blade B it is exciting. In sum, both blade-sides of this inner-cluster channel result in a low aerodynamic work coefficient. It should be noted that cluster-blade A has a higher blade vibration amplitude than cluster-blade B.

For the inner-cluster channel of item 4.) the sum of both blade-sides of this inner-cluster channel also result in a low aerodynamic work coefficient. The contributions of the blade-sides in this inner-cluster channel, however, differ to those in item 2.). It can be observed that the aerodynamic work on the pressure-side of cluster-blade C is exciting whereas on the suction-side for cluster-blade D it is stabilizing. Another difference to item 2.) is that this inner-cluster channel for cluster-blade D has a bigger amplitude than for cluster-blade C.

In this paragraph, the focus is aimed at the outer-cluster channel. It can be observed that the suction-side of cluster-blade A has local stabilizing as well as a exciting aerodynamic work coefficients, whereas the pressure-side of cluster-blade D is overall solely stabilizing as the negative aerodynamic work coefficient indicates. By comparing the aforementioned blade-sides to the respective single-blade test case SB-A (see Figure 7.4 at the top), similar distributions can be identified. In order to obtain this similarity, one distribution has to be phase shifted by  $180^\circ$  along the inter-blade phase angle direction. This is due to the kinematic definition of the cluster, as between the outer cluster-blades (cluster-blade A and D) a phase shift of  $180^\circ$  is defined, which is due to the simulated torsional movement of the cluster.

Apart from the local aerodynamic work coefficient distributions, this similarity can also be observed in the global aerodynamic damping coefficient distribution (lower graph of Figure 7.16). Here the global aerodynamic damping coefficient per cluster-channel, as well as the one for the single-blade test case, can be observed. When comparing the outer-cluster channel with the single-blade test case which, as already stated, has to be overall phase shifted by  $180^\circ$ , the aforementioned similarity can be seen. Thus, it is concluded that the flow of the outer-cluster channel underlies similar blade-to-blade influences as for the respective single-blade test case with respect to the relating traveling-waves. Furthermore, this is an indicator that the superposition principle between the traveling-wave and the influence coefficient formulation may be applied to predict the aerodynamic work of cluster-blades using single-blade data as input. Such a similarity between the inner-cluster channels and the single-blade test case cannot be observed from this comparison. Later in this chapter it will be shown that the relationship between the traveling-wave and influence coefficient formulation can be applied for all cluster-blades.

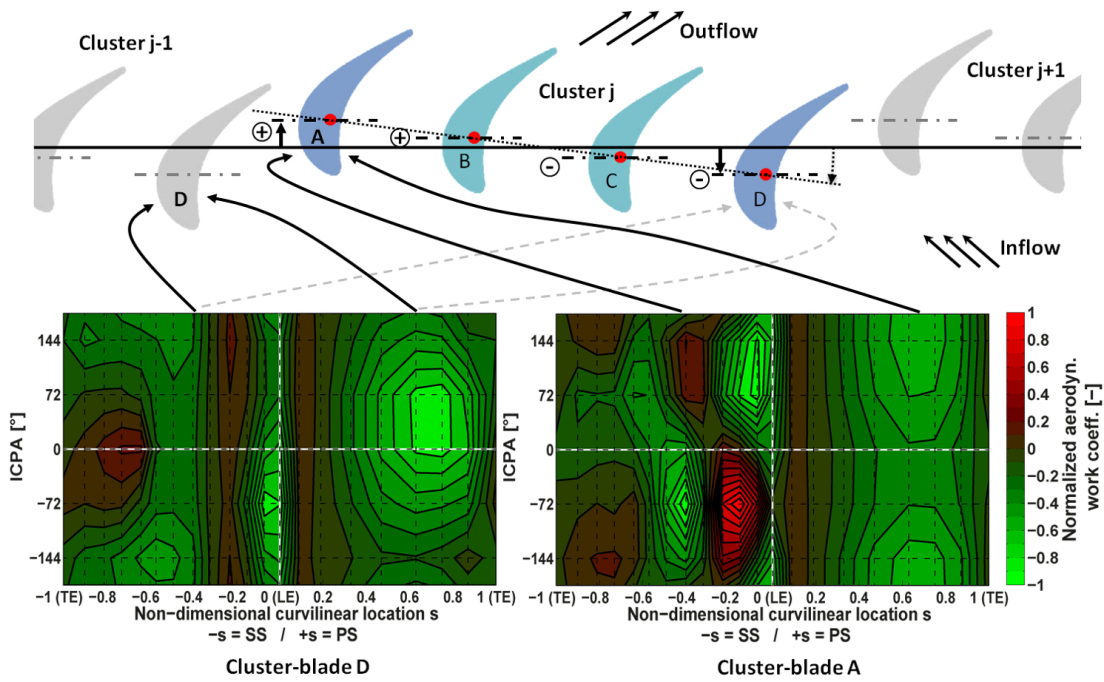


**Figure 7.12:** Detailed normalized local aerodynamic work coefficient of cluster-blades D and A of the four-blade cluster, simulating a torsional movement of the cluster (axial-bending oscillation direction per cluster-blade).

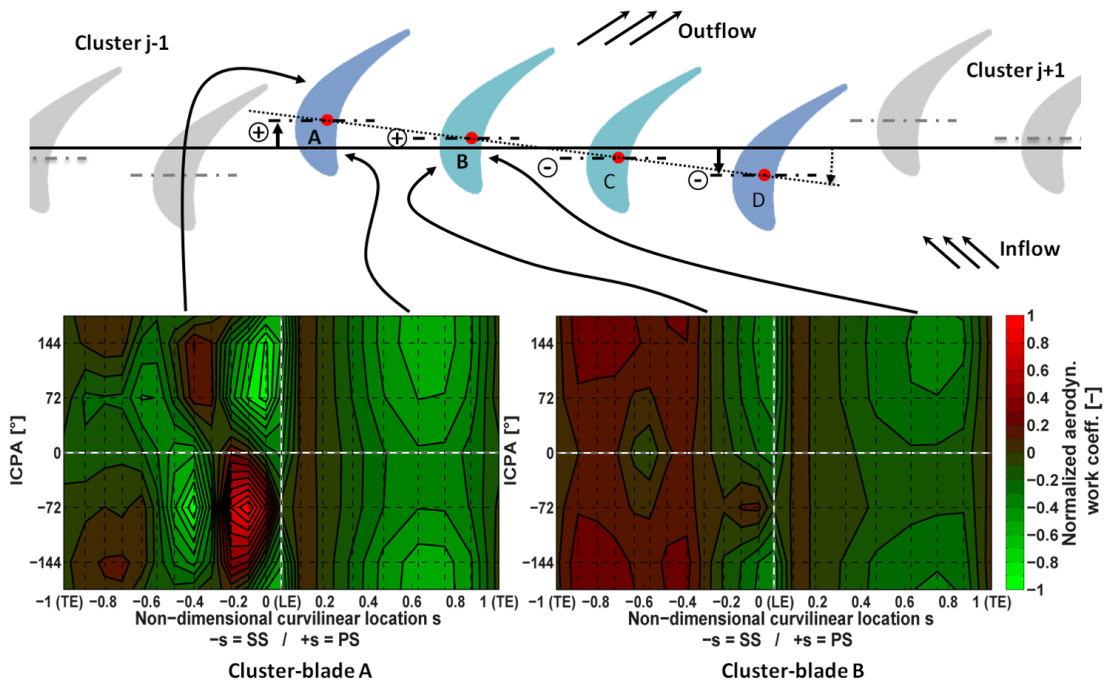


**Figure 7.13:** Detailed normalized local aerodynamic work coefficient of cluster-blades A and B of the four-blade cluster, simulating a torsional movement of the cluster (axial-bending oscillation direction per cluster-blade).

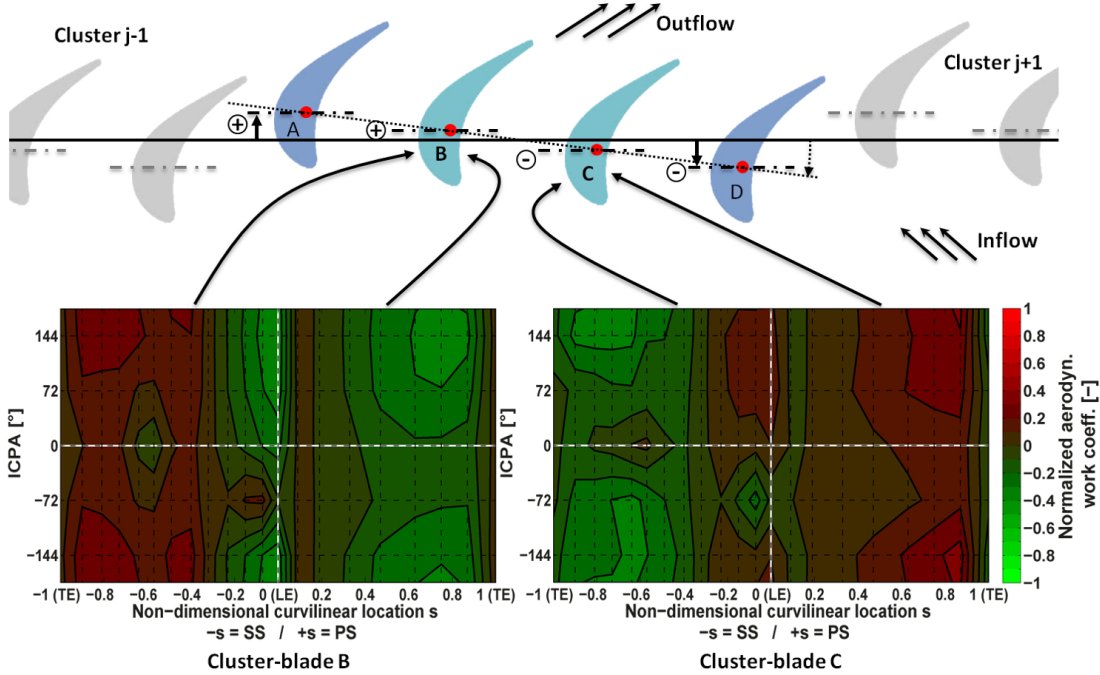


**Figure 7.14:** Detailed normalized local aerodynamic work coefficient of cluster-blades B and C of the four-blade cluster, simulating a torsional movement of the cluster (axial-bending oscillation direction per cluster-blade).

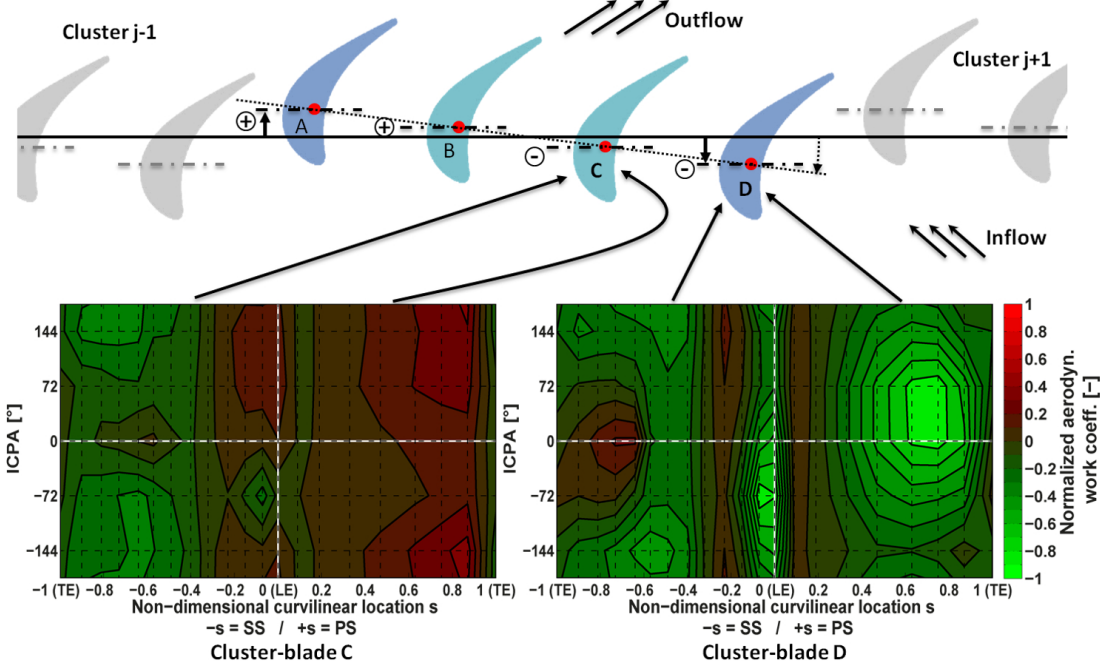


**Figure 7.15:** Detailed normalized local aerodynamic work coefficient of cluster-blades C and D of the four-blade cluster, simulating a torsional movement of the cluster (axial-bending oscillation direction per cluster-blade).

In Section 7.1 it was claimed that the vibration axis for the individual oscillation directions of the single-blade test cases can be identified in the local aerodynamic work distributions. This vibration axis can also be identified in the results of all cluster-blades and on both blade-sides (see Figures 7.12 to 7.15), for example on cluster-blade A (see Figure 7.12) on the suction-side between the non-dimensional curvilinear coordinates  $s = -0.35$  to  $s = -0.25$  as local aerodynamic work coefficient equal to zero. In this context it should be noted that the curvature of the blade profile influences the unsteadiness around the blades and thus the local aerodynamic work coefficient. The influences of the curvature can be observed when comparing the suction- to the pressure-side for all cluster-blades. Overall, the pressure-sides present much less chord-wise variations of the aerodynamic work coefficient over all traveling-waves than the suction-sides.

In contrast to the outer-cluster channel, less chord-wise variations of the local aerodynamic work coefficient for varying inter-cluster phase angles are observed for the inner-cluster channels (see Figures 7.13 to 7.15). This is related to the blade vibration phase-angles between the cluster-blades, which are all constant for the inner-cluster channels, as indicated by the cluster kinematics. For varying inter-cluster phase angles, small chord-wise variations of the local work coefficient can be observed. These variations are due to the influences from the neighboring cluster-channels. Thus, it can be concluded that these influences are related mainly to the outer-cluster channel, as the local aerodynamic work coefficient varies for inter-cluster phase angles. This consideration implies that the inner-cluster channel between cluster-blades B and C (see Figure 7.14) is less influenced by the outer-cluster channel, as this inner-cluster channel is at a larger distance than the inner-cluster channels between cluster-blades A and B (see Figure 7.13); and cluster-blades C and D (see Figure 7.15). This assumption cannot be directly confirmed in the results presenting the local aerodynamic work coefficient, as all inner-cluster channels show chord-wise variations for varying inter-cluster phase angles. In contrast, by observing the results of the global aerodynamic damping coefficient, which is presented for individual cluster-channels in the lower graph of Figure 7.16, it can be seen that the inner-cluster channel between cluster-blades B and C (green line) varies less for different inter-cluster phases angles than the other two inner-cluster channels (between cluster-blades A and B, red line and C and D, blue line). Thus it can be concluded that the influence of the outer- on the inner-cluster channel is larger than the influences between inner-cluster channels only. Furthermore, it can be stated that all inner-cluster channels have less chord-wise variations for varying inter-cluster phase angles than the outer-cluster channel.

Figure 7.16 shows the global aerodynamic damping coefficient of the four-blade cluster (lines with dots) in comparison to the related single-blade test case SB-A (black line with triangles). The global aerodynamic damping coefficients for the individual cluster-blades, as well as for the average, are determined using Equations 7.1 and 7.2. Furthermore, the confidence intervals are noted for the single-blade test case and the weighted average. In the top graph in Figure 7.16, the global aerodynamic damping coefficient is presented per cluster-blade and, at the bottom, per blade-channel between neighboring cluster-blades.



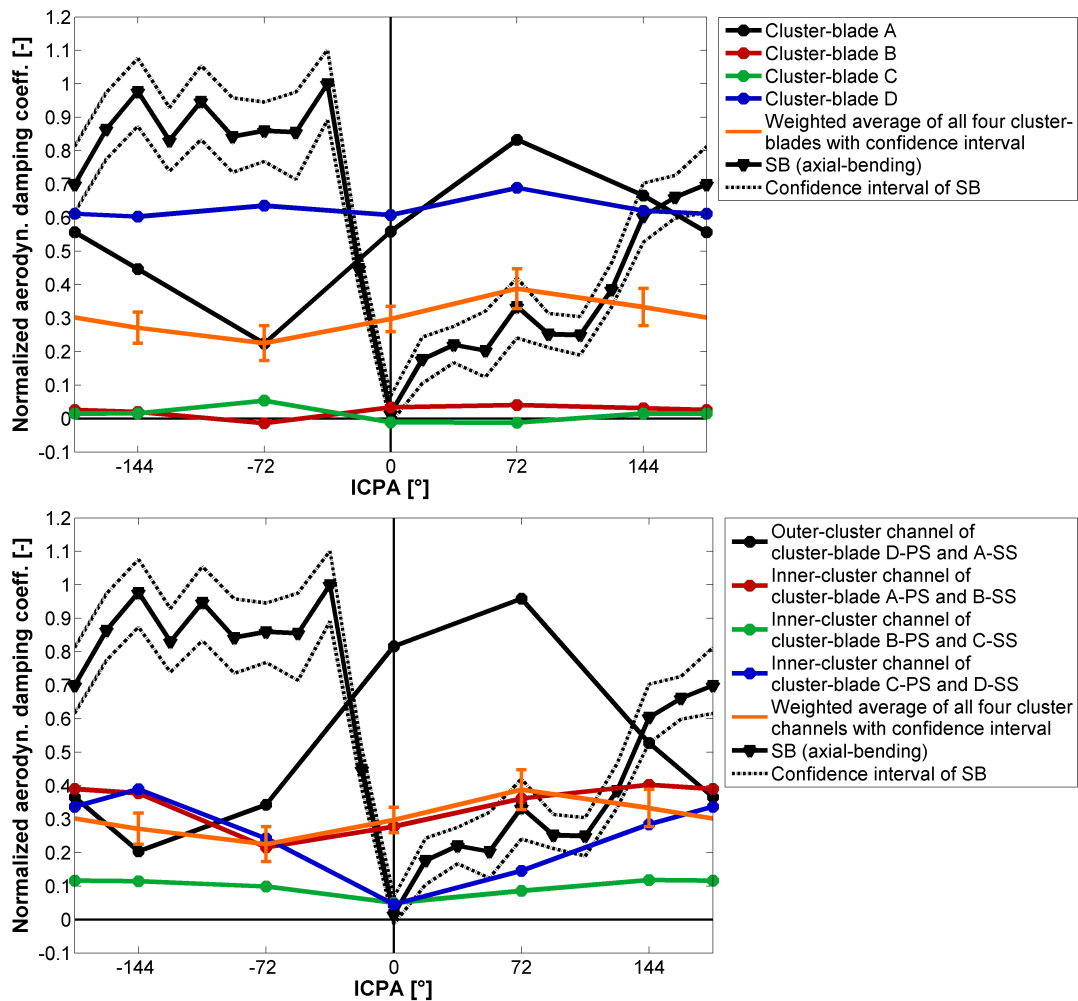


**Figure 7.16:** Normalized global aerodynamic damping of the four-blade cluster C4-A-S-T (axial-bending oscillation direction per cluster-blade), top: shown per cluster-blade, bottom: shown per cluster-channel. Both include the corresponding single-blade test case SB-A.

As indicated by the local aerodynamic work coefficient distributions, it can be observed that the outer cluster-blades (A and D) have a positive damping, whereas the inner cluster-blades (B and C) have a damping which is close to neutral. The orange line represents the average of the four cluster-blades, which has a nearly constant positive aerodynamic damping coefficient for the whole range of inter-cluster phase angles. This is in contrast to the single-blade test case, which shows a significant variation in the aerodynamic damping for the whole range of inter-blade phase-angles. Thus, it is concluded that the four-blade cluster is advantageous, since it increases the minimum aerodynamic stability level of a blade-row compared to single-blades. This increase in the minimum aerodynamic stability is achieved due to the small flow-interactions in the inner-cluster channels of the cluster.

### 7.2.3 Summary of Aerodynamic Stability of Cluster Test Cases

Four different types of cluster were investigated in the previous section, all with the same steady-state flow conditions as described in Chapter 6. The analyzed clusters differ in the type of oscillation direction used for the individual cluster-blades and in the number of blades per cluster. The investigated cluster types and the individual test cases are summarized below:

1. Three two-blade clusters with each cluster-blade having the same oscillation direction. Three vibration directions were investigated (axial- and flap-bending, torsion)
2. One four-blade cluster with each cluster-blade oscillating in the axial-bending direction, while having the blade vibration amplitudes and phase angles of the individual cluster-blades adjusted so that a torsional movement of the cluster as a whole is simulated.

The measurements of the two-blade cluster test cases lead to the following findings:

- For all three oscillation directions, the local aerodynamic work transferred between the blades and the flow is larger for the blade channel between two consecutive clusters (outer-cluster channel) than for the blade channel within the cluster (inner-cluster channel).
- The test cases with a bending oscillation direction are more sensitive to blade vibrations on the suction-side than on the pressure-side. For the test cases with a torsion oscillation direction, no difference between both blade-sides is observed.
- When comparing both cluster-blades with each other, similar local aerodynamic work distributions are observed for the pressure-side but not for the suction-side. This can be seen, apart from the level of the distribution and only for the bending oscillation cases. For the test case with a torsion oscillation both blade-sides show similar local aerodynamic work distributions, apart from the level.
- As expected the comparison of the three cluster test cases showed that the oscillation direction is influencing the interactions between the cluster-blades. This experimental observation is in-line with the literature describing numerical simulations, see for example Corral et al. [2007].
- For all test cases, the local aerodynamic work coefficient distributions of the outer-cluster channel demonstrate a high similarity to the respective single-blade test cases.
- For the test cases with bending oscillation a similarity to the respective single-blade test cases is observed only for the pressure-side of the inner-cluster channel. For the test cases with a torsion oscillation direction, it is detected for the entire inner-cluster channel. It should be noted that for the reported observations of the inner-cluster channel, apart from the similar distributions, different average value levels are observed.

- The positive effect of increasing the minimum damping is observed for the torsion oscillation test case. For the bending oscillation test cases this is not observed.

The measurements of the four-blade cluster test case lead to the following findings:

- The exchange of the aerodynamic work between the flow and the cluster-blades is higher for the blades between neighboring clusters (outer-cluster channel) than for the inner-cluster channels, as to be expected.
- The interaction between the flow and the blades in the outer-cluster channel is similar to the interactions of the respective single-blade test case SB-A.
- The influence of the outer-cluster channel on the inner-cluster channel is higher than the influences between inner-cluster channels only.
- For the inner-cluster channels less chord-wise variations of the local aerodynamic work coefficient can be seen. This is a result of the cluster kinematics, which state that for varying inter-cluster phase angles the phase angle between neighboring cluster-blades in a cluster is constant.
- Next to the blade motion, the curvature of the blade is identified as an influencing factor of the unsteadiness around the blade and thus to the aerodynamic damping.
- Overall, both outer cluster-blades have a positive global aerodynamic damping, whereas the inner cluster-blades have almost no contribution to the global aerodynamic damping.
- All cluster-blades are averaged in a way to represent the cluster and are compared to the respective single-blade test case SB-A. The comparison shows that the cluster has an increased minimum damping which is a positive result with respect to the aeroelastic stability.



### 7.3 Prediction of the Aerodynamic Values of Cluster-Blades by Using Single-Blade Test Results

This chapter presents the applicability of the traveling-wave and influence coefficient formulation to predict the aerodynamic stability parameters of cluster-blades by using single-blade measurements as input. The related mathematical formulation of this method was introduced in Section 2.4. The principal steps to predict an individual cluster-blade are displayed in Figure 7.17.

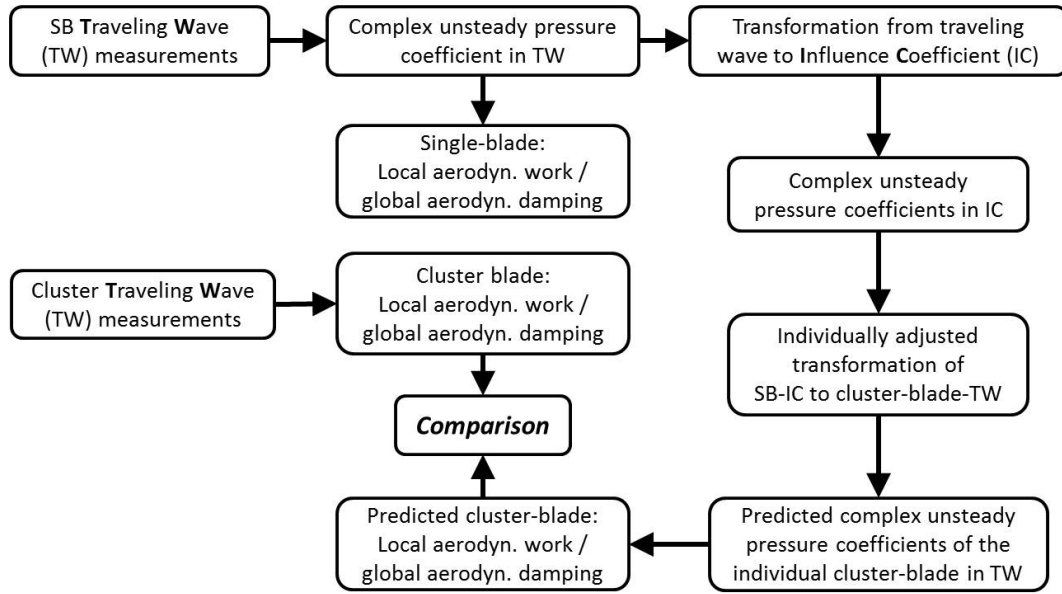


**Figure 7.17:** Procedure to predict the aerodynamic values of individual cluster-blades by using single-blade measurement data as input.

In the next two sections, the previously-introduced method (see Figure 7.17 in Section 2.4) is applied and the predicted results are compared to the measured cluster results. First, this is done for the two-blade cluster (see Section 7.2.1) and second, for the four-blade cluster (see Section 7.2.2). The transformation of the complex unsteady pressure coefficient from single-blade influence coefficients to the individual cluster-blade traveling-wave formulation is described as:

$$\tilde{c}_{C,I,TW} = \sum_{n=0}^{N-1} \tilde{c}_{SB,IC}^{n,0} a_{C,I}^{n,0} e^{-i\sigma_{C,I}^{n,0}} \quad (7.3)$$

In order to solve Equation 7.3, the following input parameters are necessary:

- The cluster-specific blade-vibration amplitude  $a_{C,I}^{n,0}$ , based on the kinematics of the individual cluster-blades in the cluster configuration
- The cluster-specific blade-vibration phase lag  $\sigma_{C,I}^{n,0}$ , based on the kinematics of the

individual cluster-blades in the cluster configuration

- The complex unsteady pressure coefficients for the single-blade test case  $\tilde{c}_{SB,IC}^{n,0}$  expressed in the influence coefficient formulation

It should be noted that Equation 7.3 was introduced in Section 2.4 and is displayed again for the sake of completeness. A detailed description of the individual terms in Equation 7.3 can be found in the aforementioned section.

### 7.3.1 Two-Blade Cluster

The two-blade cluster oscillating with an axial-bending oscillation direction (C2-A) is used in this section to show the applicability of the aforementioned method. Thus, as a basis for the prediction of the cluster-blades, the single-blade test case SB-A is employed (see Section 7.1). In the following, the predicted cluster-blade results are compared to the measured results of the cluster test case C2-A (see Section 7.2.1).

As previously noted, next to influence coefficients of the unsteady pressure coefficient, two principal parameters have to be defined as input for Equation 7.3. These are the cluster-related blade vibration amplitude and phase lag kinematics (for details regarding the cluster kinematics refer to Section 4.2). Since both cluster-blades have the same blade vibration amplitudes, the parameter describing the relation between the individual cluster-blade vibration amplitudes is set to  $a_{C,I}^{n,0} = 1$  for  $n = 0, \dots, N - 1$ . Furthermore, the values which define the phase-lag kinematics of the cluster-blades  $\sigma_{C,I}^{n,0}$  are described in Table 7.4. These phase-lag values are based on the inter-cluster phase angle definition and the fact that both cluster-blades oscillate in-phase. The values in the table describes the phase lag between the regarded cluster-blade ( $\sigma_{C,A}^{n,0}$  or  $\sigma_{C,B}^{n,0}$ ) and the blade  $n$  for the chosen influence coefficient.

<b>SB IC index:</b>	<b>Cluster blade A:</b>	<b>Cluster blade B:</b>
$n$	$\sigma_{C,A}^{n,0}$	$\sigma_{C,B}^{n,0}$
0	0	0
1	0	$\Gamma_1$
2	$\Gamma_{\lambda=1}$	$\Gamma_1$
3	$\Gamma_{\lambda=1}$	$\Gamma_2$
$\vdots$	$\vdots$	$\vdots$
N-3	$\Gamma_{J-2}$	$\Gamma_{J-1}$
N-2	$\Gamma_{J-1}$	$\Gamma_{J-1}$
N-1	$\Gamma_{J-1}$	0

**Table 7.4:** Kinematic relation between single-blade influence coefficients and cluster traveling-wave coefficients of the two-blade cluster test cases.

### 7.3. Prediction of the Aerodynamic Values of Cluster-Blades by Using Single-Blade Test Results

In Figure 7.18 at the top, the results of the individually-predicted cluster-blades are presented as local work coefficient distributions. In order to compare the measured test results of the individual cluster-blades with the predicted results, the measured test results are shown in the middle of Figure 7.18 and the absolute difference between both (predicted and measured) is shown at the bottom. All distributions are normalized using the absolute peak value of the measured cluster test case. It should be stressed that the absolute differences between the measured and the predicted results were determined before the normalization was carried out.

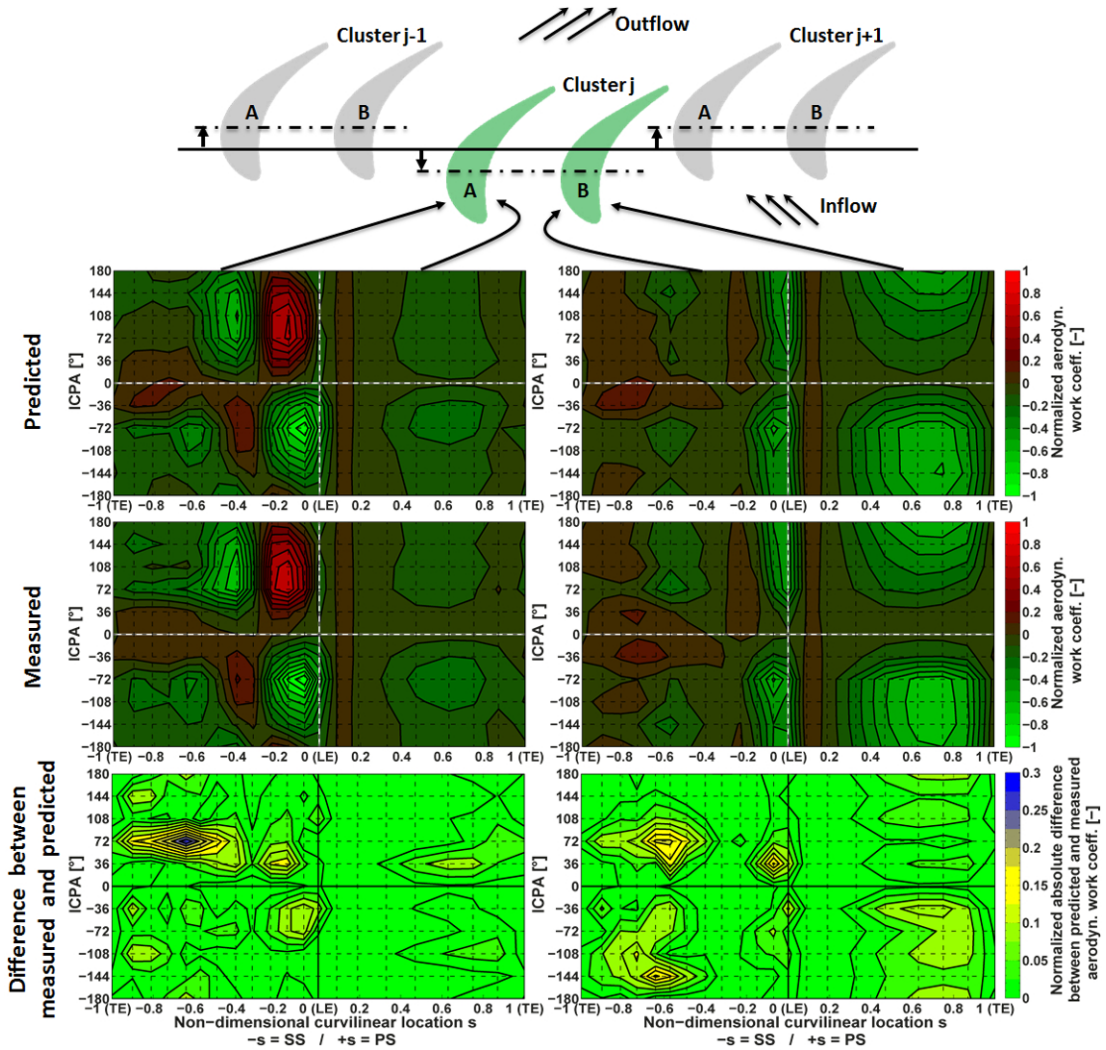


**Figure 7.18:** Normalized local aerodynamic work coefficient of cluster-blades A (left) and B (right) of the two-blade cluster test case C2-A (axial-bending oscillation direction). Top: predicted results; middle: measured results; bottom: absolute difference between predicted and measured results.

## Time-Resolved Results and Aerodynamic Stability Analysis

---

In addition to the local aerodynamic work coefficient, the global aerodynamic damping coefficient of the simulated and the measured cluster-blades is presented in Figure 7.19. Here the normalization is performed using the absolute peak value of the single-blade test case. It should be noted that this normalization is chosen in order to be in-line with those applied in the previous sections.

Before analyzing the comparison, it should be noted that this procedure is applied accordingly for the two-blade cluster test cases with flap-bending (C2-F) and torsion oscillation direction (C2-T) (detailed in Section 7.2.1). The predicted distributions of the respective local aerodynamic work coefficient and global aerodynamic damping coefficient are displayed in Appendix A.5.

Overall, it can be observed from the local comparisons (Figure 7.18) that a good local agreement between the measured and the predicted cluster test case is achieved for all inter-cluster phase angles. For each inter-cluster phase angle, a good agreement along the chord-wise direction can be seen for both cluster-blades. Furthermore, the characteristic of the two-blade cluster having lower local aerodynamic work coefficient values for the inner-cluster channel than for the outer-cluster channel also shows a good agreement. A similar conclusion can be drawn in the two-blade cluster test cases with different oscillation directions presented in Appendix A.5 (for flap-bending see Figure A.6, and for torsion see Figure A.8).

The current test case (C2-A) shows a local anomaly for both cluster-blades on the rear part of the suction-side mainly for an inter-cluster phase angle of  $\Gamma_\lambda = 72^\circ$ . It is assumed that this is a result of slight measuring variations. For both blades very low local aerodynamic work coefficients are observed in this region. Thus small variations of the flow between the results used for the prediction (single-blade test case) and the measured results (cluster case) can result in large differences. This can also be observed in the results presented in Appendix A.5, which show also differences in the same region on the rear part of the suction side, but for different inter-cluster phase angles and different locations.



### 7.3. Prediction of the Aerodynamic Values of Cluster-Blades by Using Single-Blade Test Results

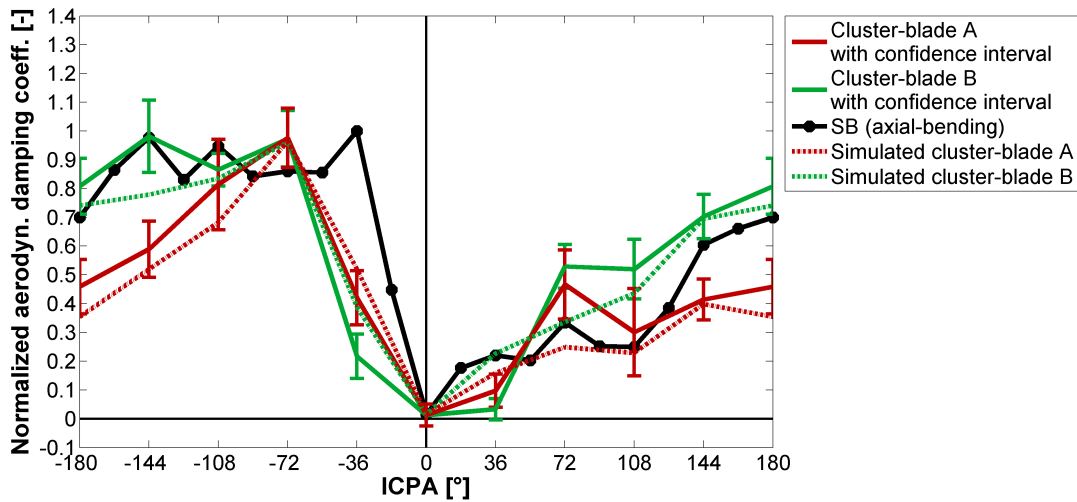


**Figure 7.19:** Normalized global aerodynamic damping coefficient of the predicted two-blade-cluster test case C2-A (axial-bending oscillation direction).

The comparison of the global aerodynamic damping results is presented for both cluster-blades in Figure 7.19. Similar to the comparison between the predicted and measured results of the local aerodynamic work coefficient, a good agreement of the results for the global aerodynamic damping coefficient can be seen. In addition to the predicted and measured results, the figure shows the confidence interval representing the estimated random error of the measured cluster-blades (for details regarding the random error refer to Section 5.4.1). It can be observed that the differences between the prediction and the measured results are situated within the confidence interval of the measured cluster-blade results, which confirms the previously made assumption of small flow variations influencing the results. Hence, it can be concluded that the method is able to predict the aerodynamic values of individual blades in the two-blade cluster within the limits of the experimental measurement accuracy.

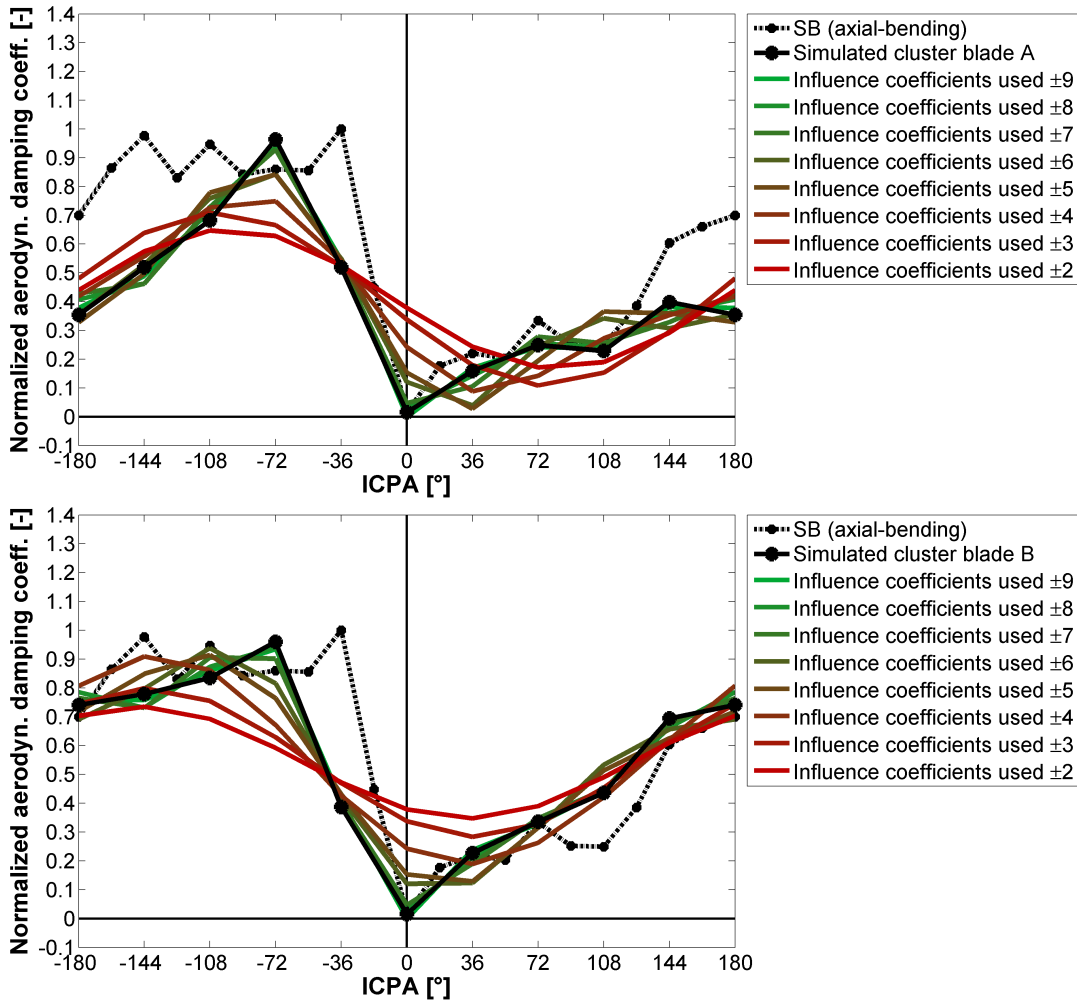


**Figure 7.20:** Impact of the number of applied influence coefficients to simulate the aerodynamic damping coefficient of cluster-blade A (top) and B (bottom) of the two-blade cluster case C2-A.

On the basis of the normalized global aerodynamic damping coefficient, Figure 7.20 displays the impact of the number of influence coefficients applied to simulate cluster-blade A (top) and B (bottom) of the two-blade cluster test case C2-A. All graphs within the figure are normalized using the absolute peak value of the single-blade test case SB-A. The coloring from red to green indicates an increasing number of influence coefficients used additionally to the zeroth (reference) influence coefficient. It can be seen that, next to the impact of the blade itself, the influence of the neighboring six blades (in both directions) have to be considered in order to achieve an error of less than 10%. Including one more neighboring blade in both directions (in total  $\pm 7$  influence coefficients) lowers the error to less than 5%. As the transformation between the traveling-wave and influence coefficient formulation is based on the harmonic superposition relation, it can be stated that the closer the predicted curvature is to a sine curve the smaller becomes the number of necessary influence coefficients.

### **7.3.2 Four-Blade Cluster Simulating Torsion**

In the previous section it was shown that the aerodynamic parameters of the individual cluster-blades of a two-blade cluster can be predicted using single-blade test results as input data. This section is dedicated to analyzing the applicability of this procedure to predict the aerodynamic parameters of the individual cluster-blades of a four-blade cluster. In order to validate the predicted results, they are compared to those of the test case C4-A-S-T presented in Section 7.2.2. This cluster test case simulates a four-blade segment oscillating in the torsion direction by vibrating each cluster-blade in the axial-bending direction and by adjusting the blade-vibration amplitude and phase lag accordingly (for details refer to Section 4.3 and Section 7.2.2). In order to apply the procedure previously introduced, the input parameters of Equation 7.3 have to be defined for this test case.

The cluster-specific kinematics relating to the blade-vibration amplitude and the phase lag have been presented in Section 2.4 and are listed in Table 2.1. Briefly summarized, the relationship between the inner- and outer-blade vibration amplitudes has to be account for as noted in Table 7.3. Furthermore, the phase-lag has to be adjusted so that the first two cluster-blades are always in the opposite phase to the last two in the cluster. In addition to the individual cluster-blade phase-shift relations, the respective inter-cluster phase angles have to be accounted for, too.

The local aerodynamic work coefficient distributions of the individually-predicted cluster-blades are presented in Figures 7.21 and 7.22 at the top. For the purpose of comparison, the measured test-results of the individual cluster-blades are displayed in the middle and the absolute difference between the measured and the predicted results of the cluster-blade is shown at the bottom. All distributions are normalized using the absolute peak value of the measured cluster test case. It should be stressed that the absolute differences between the measured and the predicted results are calculated before the normalization was performed.

In addition to the local aerodynamic work coefficient, the global aerodynamic damping coefficient of both, the simulated and the measured cluster-blades, are presented in Figure 7.23. In this case, the normalization is performed using the absolute peak value of the single-blade test case.

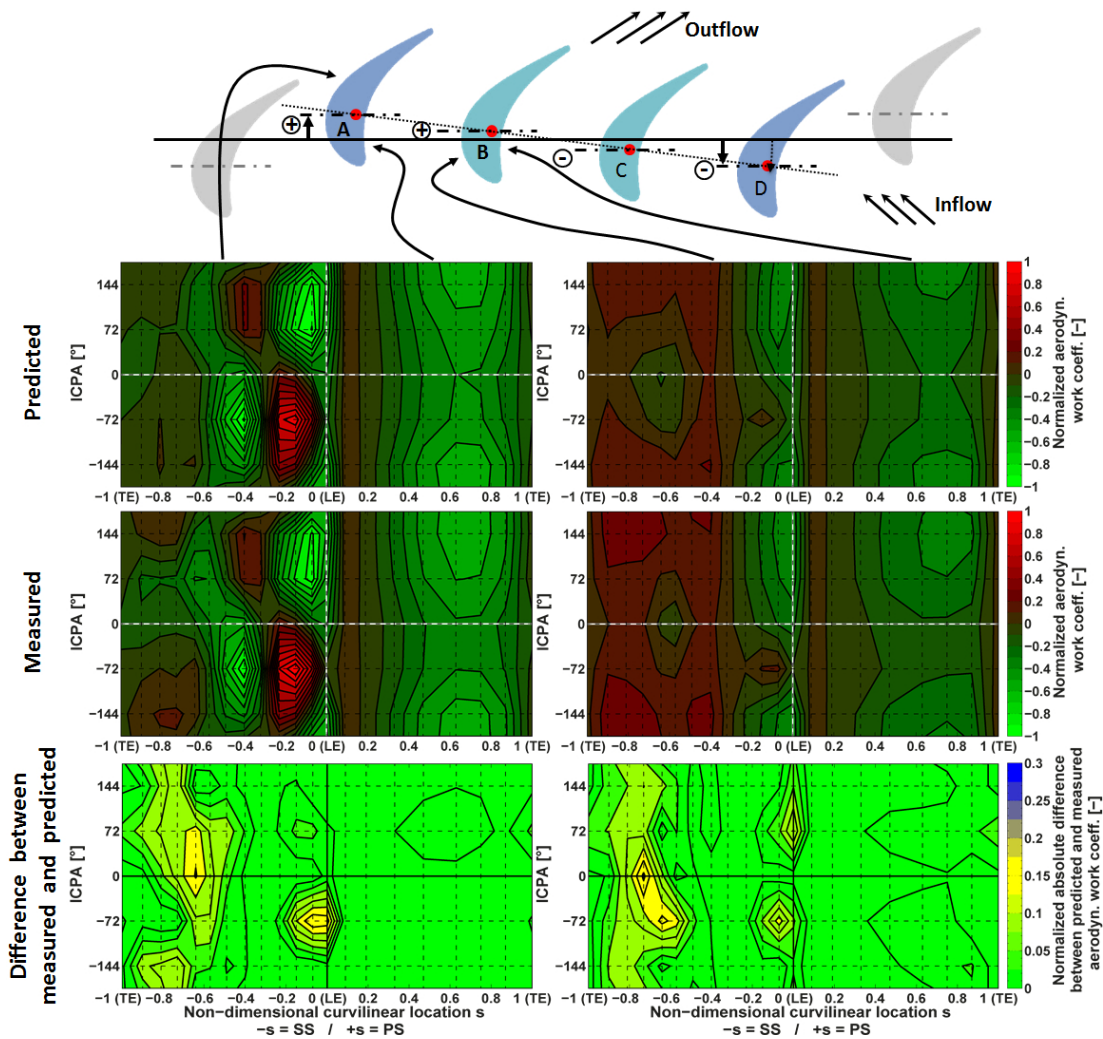


**Figure 7.21:** Normalized local aerodynamic work coefficient of cluster-blades A (left) and B (right) of the four-blade cluster test case C4-A-S-T (axial-bending oscillation direction per cluster-blade, representing a torsional movement of the cluster). Top: predicted results; middle: measured results; bottom: absolute difference between predicted and measured results.

Overall, it can be observed that the predicted results of the local aerodynamic work coefficient (see Figures 7.21 and 7.22) are almost identical to the measured results of the individual cluster-blades. Details show that the suction-sides of the individual cluster-blades are less well predicted than the pressure-sides. In specific it can be observed that the second part in chord-wise direction of the cluster-blade is less well predicted than the first part. A similar observation was made in the previous section describing the prediction of the two-blade cluster configurations. As noted before it is assumed that the differences between the predicted and measured results in this region of the blade are related to small variations in the flow. In order to estimate the influence of the minor flow variations the confidence interval of the

### 7.3. Prediction of the Aerodynamic Values of Cluster-Blades by Using Single-Blade Test Results

random error is calculated for the measured cluster-blades, and included in the next figure presenting the comparison of the predicted and measured results for the global aerodynamic damping coefficient. (For details of the confidence interval refer to Section 5.9.)

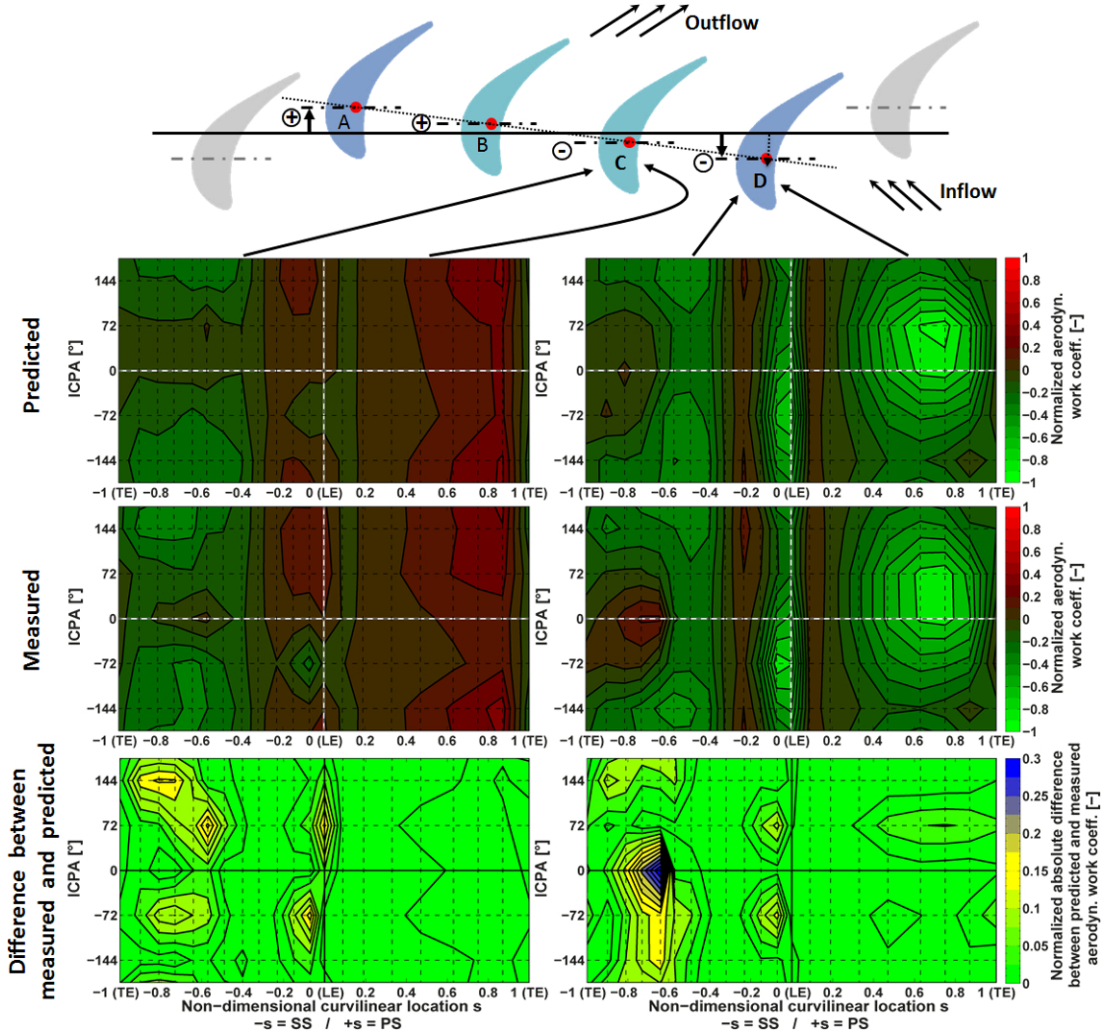


**Figure 7.22:** Normalized local aerodynamic work coefficient of cluster-blades C (left) and D (right) of the four-blade cluster test case C4-A-S-T (axial-bending oscillation direction per cluster-blade, representing a torsional movement of the cluster). Top: predicted results; middle: measured results; bottom: absolute difference between predicted and measured results.

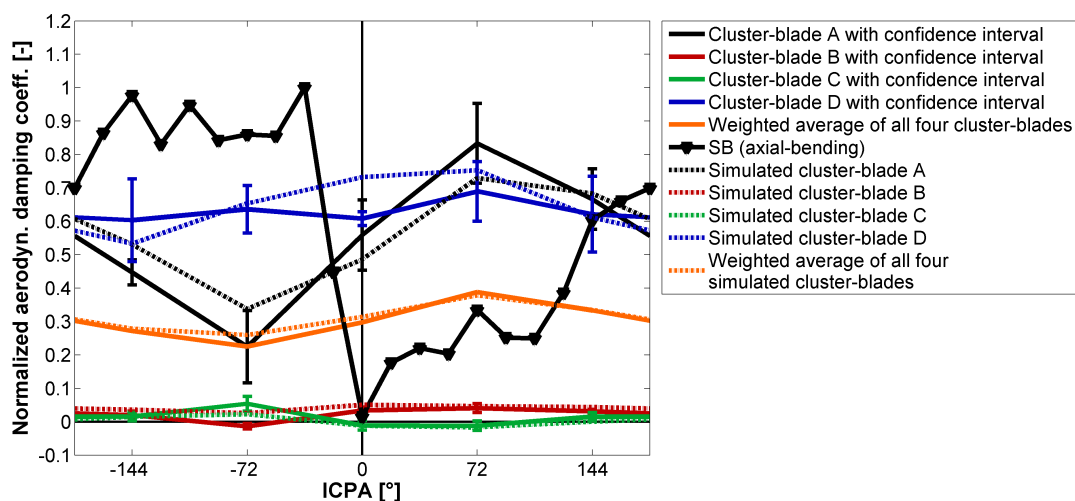


**Figure 7.23:** Normalized global aerodynamic damping coefficient of the predicted two-blade-cluster test case C4-A-S-T (axial-bending oscillation direction per cluster-blade, representing a torsional movement of the cluster).

In Figure 7.23 the predicted and measured results of the global aerodynamic work coefficient are presented. Similar to the analysis of the local aerodynamic work coefficient an overall good agreement between the predicted and measured results is observed. Furthermore, it can be seen that the method is capable to reproduce the individual cluster-blade distributions for varying inter-cluster phase angles.

As previously noted small differences can be identified between the predicted and the measured results of the individual cluster-blades, which are caused by small variations of the flow. Taking into account the confidence intervals of the measured signals it can be observed that almost all are in the margin of the confidence intervals. Furthermore, it can be observed that for inner cluster-blades the difference between predicted and measured results is smaller than for the cluster-blades at the corner of the cluster.

As shown for the two-blade cluster test case in Figure 7.20, the same number of neighboring blades (six) additionally to the to the zeroth (reference) blade itself are necessary in order to achieve an error of less than 10%. Including one more neighboring blade in both directions (in total  $\pm 7$  influence coefficients) lowers the error to less than 5%. In the Appendix A.5.3 the impact of the number of applied influence coefficients to simulate the aerodynamic values of the cluster-blades is shown Figures A.10 and A.11.

### 7.3.3 Summary and Conclusion of Predicting the Aerodynamic Values of Cluster-Blades by Using Single-Blade Test Results

The procedure introduced at the beginning of Section 7.3 was successfully applied to the two-blade cluster test cases with identical oscillation directions for both cluster-blades. Furthermore, it was successfully applied for the four-blade cluster test case simulating a torsional

### 7.3. Prediction of the Aerodynamic Values of Cluster-Blades by Using Single-Blade Test Results

---

movement of the whole cluster by individually adjusting the blade vibration amplitudes. For all oscillation directions of the two-blade cluster a good agreement between the predicted and measured results could be observed. This for comparison of the local values, representing the chord-wise distribution along the blade surface and also for the global comparison, representing the entire blade. For the four-blade cluster also a good agreement between the predicted and measured results could be observed. This as for the two-blade cluster locally and globally.

For all cluster cases the suction side was less well predicted than the pressure side as the local work coefficient distributions showed. The differences between predicted and measured results of both blade-sides were attributed to small variations in the flow, which occurred for the compared cases (single-blade case used for prediction and cluster case). The confidence interval of the random error estimating variances in the flow field confirmed this.

On the basis of the prior results it is concluded that the prediction method is experimentally validated within the limits of the measurement accuracy. In addition, it can be noted that this validation serves as a basis for numerical simulations using a similar method to perform parameter studies for cluster configurations under similar flow conditions, see for example Chernysheva [2004].

In order to apply this procedure, it is important to know the kinematics of the individual cluster-blades. These kinematics have to be defined by means of the oscillation direction of the individual cluster-blades, as well as the individual cluster-blade vibration amplitude and phase relationships. Furthermore, the assumptions on which this method is based have to be considered, as stated in Sections 2.3 and 2.4.

It should be noted that this procedure is based on the linearized unsteady aerodynamic theory as described by Verdon [1987]. The linearization implies that small blade vibration amplitudes are a prerequisite for the applicability of this theory. As limitation for a maximum blade vibration amplitude it is assumed that for the test cases described in this work, values up to about fifteen times higher are representative. Furthermore it has to be considered that with an increasing vibration amplitude the incidence angle changes and thus different flow conditions have to be considered. This effect is of more significance for torsion oscillation directions than for bending.

With respect to the applicability for varying flow conditions, it is assumed to be valid for subsonic flow conditions. As only one flow condition is investigated in this work this assumption is based on the experimental investigations for single-blade test cases found in the literature. For example Nowinski and Panovsky [2000] used the superposition principle for a parameter study on thin, highly-curved low-pressure turbine blades oscillating in torsion mode-shape with reduced frequencies in the range of 0.16 to 0.31 and inlet Mach-numbers in the range of 0.36 to 0.5. Schläfli [1989] reported similar flow conditions as found in Nowinski and Panovsky [2000], but has shown that the superposition principle can be applied also for flat profiles in case of single-blade configurations.





## 8 Summary, Conclusions and Outlook

**I**N this chapter the key findings are summarized and conclusions supporting the design procedure of cluster configurations are highlighted.

### 8.1 Summary and Conclusions

The main objective of the present work was to validate experimentally the applicability of the superposition principle to predict the aerodynamic parameters of the individual cluster-blades in a cluster by using single-blade data acquired during traveling-wave mode measurements. Furthermore, this thesis analyzed experimentally the aerodynamic stability of a two-blade cluster, which has different oscillation directions (torsion, axial- and flap-bending) and a four-blade cluster, which oscillates in a torsional motion.

The applied approach consisted of establishing a data base of experimental traveling-wave measurements under identical steady-state flow conditions. In order to achieve this, two cluster test-cases simulating blade-row configurations applied in low-pressure turbines were selected and investigated. The first consisted of two blades simulating a welded-in-pair configuration and the second of four blades representing a cast vane-segment. For the two-blade cluster case, three oscillation directions were investigated, the first torsion, axial- and flap-bending mode. The torsional oscillation of the four-blade cluster was simulated by oscillating each cluster-blade with an axial-bending vibration direction and by individually adjusting the cluster-blade vibration amplitudes and phase angles according to the cluster kinematics. As a basis for the prediction of the cluster-blades in a cluster, single-blade tests were carried out with the vibration conditions of the individual cluster-blades.

All measurements were performed in a non-rotating test facility under subsonic flow conditions on a turbine cascade composed of 20 blades. For each test case, all possible oscillation patterns of the single-blade (inter-blade phase angles) and cluster configurations (inter-cluster phase angles) were performed in the traveling-wave mode. During these tests the steady-state flow conditions were measured using pressure taps along the blade-chord at three different blade heights (25%, 50% and 90%), 5-hole L-shaped probes upstream and downstream of

## Summary, Conclusions and Outlook

---

the test section, as well as pressure taps on the shroud wall along the test section. The time-resolved measurements were acquired by unsteady pressure taps along the blade surface at 50% blade height and by displacement sensors measuring the corresponding position of the blades.

The analysis of the steady-state flow measurements, which was used for all time-resolved test cases showed the following main findings:

- Close to identical flow conditions are achieved for all investigated test cases, allowing a comparison of the different test cases.
- The average Mach-numbers of all test cases (single-blade and cluster) were  $M_1 = 0.34$  at the inlet and  $M_2 = 0.69$  at the outlet.
- The average flow angles of all test cases (single-blade and cluster) were  $\beta_1 = 46^\circ$  at the inlet and  $\beta_2 = -57.9^\circ$  at the outlet.
- The blade surface was exposed to subsonic flow conditions typical for a turbine-blade loading at mid-channel (50% blade height).
- Along the hub and the shroud region, secondary flows were observed but did not influence the flow at mid-channel height. Therefore the flow could be considered as quasi two-dimensional in this region.

Single-blade test cases were performed in order to predict the aerodynamic parameters of the individual cluster-blades using the superposition principle, and as a reference to the cluster test cases. The blade vibration directions were chosen to be identical to the vibration directions of the individual cluster-blades. All measurements were performed with the same reduced frequency ( $k = 0.26$ ). Overall, for both cluster test cases, three vibration-directions were investigated: torsion, axial-bending and flap-bending. The analysis of the corresponding single-blade test results revealed the following aerodynamic effects:

- In the traveling-wave formulation:
  - The parameters influencing the unsteady pressure around the blade was the inter-blade phase angle which the blade-row was oscillated and the curvature of the blade.
  - The local distribution of the aerodynamic work was mainly influenced by the unsteady pressure coefficient phase-lag and the oscillation direction.
  - Overall, the aerodynamic damping for all three test cases was positive for all inter-blade phase angles and thus aerodynamically stable operating conditions were present.

- In the influence coefficient formulation:
  - For both test cases with a bending oscillation, the immediate neighboring blades had a larger influence on the reference blade than in the torsion case.
  - For all test cases, the neighboring blades in the suction-side direction had a larger influence than those in the pressure-side direction.
  - The global distribution of the influence coefficients showed similar tendencies for the test cases with a flap-bending and torsion oscillation as observed in the literature (for example see Panovsky and Kielb [2000]).

The analysis of the measurement results obtained for the two-blade cluster test cases revealed the following findings:

- For all three oscillation directions, the local aerodynamic work transferred between the blades and the flow was larger for the blade channel between two consecutive clusters (outer-cluster channel) than for the blade channel within the cluster (inner-cluster channel).
- When comparing both cluster-blades with each other, similar local aerodynamic work distributions could be observed for the pressure-side but not for the suction-side. This could be seen, apart from the level of the distribution and only for the bending oscillation cases. For the test case with a torsion oscillation both blade-sides showed similar local aerodynamic work distributions, apart from the level.
- As expected by the comparison between the three cluster test cases, the blade oscillation direction influenced the interactions between the cluster-blades. This experimental observation was comparable to the literature, see for example Corral et al. [2007].
- For all vibration modes, the local aerodynamic work distributions of the outer-cluster channel demonstrated a high similarity to the respective single-blade test cases.
- For the test cases with bending oscillation a similarity to the respective single-blade test cases was observed only for the pressure-side of the inner-cluster channel. For the test cases with a torsion oscillation direction, it was detected for the entire inner-cluster channel.
- The positive effect of increasing the minimum damping was observed for the torsion oscillation test case. For the bending oscillation test cases this was not observed.

The measurements of the four-blade cluster test case lead to the following findings:

- The exchange of the aerodynamic work between the flow and the cluster-blades was higher for the blades between neighboring clusters (outer-cluster channel) than for the inner-cluster channels, as to be expected.

## Summary, Conclusions and Outlook

---

- The interaction between the flow and the blades in the outer-cluster channel was similar to the interactions of the respective single-blade test case SB-A.
- The influence of the outer-cluster channel on the inner-cluster channel was higher than the influences between inner-cluster channels only.
- For the inner-cluster channels less chord-wise variations of the local aerodynamic work could be seen. This was a result of the cluster kinematics, which state that for varying inter-cluster phase angles, the phase angle between neighboring cluster-blades in a cluster is constant.
- Next to the blade motion, the curvature of the blade was identified as being an influencing factor of the unsteadiness around the blade and thus to the aerodynamic damping of the blade.
- Overall, both outer cluster-blades had a positive global aerodynamic damping, whereas the inner cluster-blades had almost no contribution to the global aerodynamic damping.
- All cluster-blades were averaged in a way to represent the cluster and were compared to the respective single-blade test case SB-A. The comparison showed that the cluster had an increased minimum damping which is a positive result with respect to the aeroelastic stability.

From an aerodynamic point of view, it can be summarized that fixing blades together as clusters is, in principle, advantageous. This is because it minimizes the aerodynamic work within the inner-cluster channels and thus enables a possible increase in the minimum aerodynamic damping compared to a single-blade test case with a similar blade vibration direction. This could be shown for the two-blade cluster in the torsional vibration direction, as well as for the four-blade cluster test case simulating a torsional oscillation (for a blade-row of 20 blades). For the two-blade clusters oscillating in bending direction, no increase in the minimum damping could be observed for the flow conditions investigated in this work. These observations for the two-blade cluster test cases are in agreement with the findings of Corral et al. [2007]. His numerical parameter study showed in addition that the minimum aerodynamic damping of the two-blade cluster with bending direction increases for lower reduced frequencies. Thus, it is assumed that for lower reduced frequencies the two-blade cluster with bending oscillation can also be of advantage, since an increase of the minimum aerodynamic damping can be observed with respect to the single-blade case.

At this point, a data base of single-blade and cluster test cases was established. It was used to investigate the applicability of the superposition principle to predict the aerodynamic parameters of individual cluster-blades by using experimental aerodynamic single-blade data as input. To apply this procedure, it was important that the single-blade test cases had an identical vibration-direction and -frequency as the individual predicted cluster-blades. In the first step of the procedure, the single-blade results in the traveling-wave formulation

were converted to influence coefficients. In the next step, these single-blade influence coefficients were transformed back into the traveling-wave formulation, including the cluster kinematics of the individual cluster-blades (instead of single-blades). Thus, the resulting aerodynamic parameters in the traveling-wave formulation represent those of the individual cluster-blade.

This procedure was used to predict the aerodynamic stability of the individual cluster-blades for the two- and four-blade cluster cases described earlier. The experimentally acquired aerodynamic parameters of the single-blade cases were used as input data for this procedure, taking into account the corresponding oscillation direction. In order to validate the predicted results of the procedure, they were compared to the measurements of the respective cluster cases. The comparison of both results lead to the following findings:

- A good agreement, within the limits of the experimental accuracy, exists between the predicted and the measured results of the global aerodynamic damping distributions. These were determined, by accounting for small flow variations between the compared results in terms of confidence intervals of the measured cluster-blade signal.
- Overall, a good agreement of the local (chord-wise) aerodynamic work distributions were observed. This shows that the prediction is capable to reproduce the aerodynamic effects occurring within the inner- and outer-cluster channels.
- The local (chord-wise) aerodynamic work distributions also showed that the suction-sides were less well predicted than the pressure-sides. This was attributed to small flow variations occurring between the measured single-blade case used for the prediction, and the measured individual cluster-blade to which it was compared to.
- The observations of the three aforementioned bullet-points were identified for both cluster cases and for all corresponding oscillation directions investigated in this work.

This comparison leads to the conclusion that the aforementioned procedure was successfully validated experimentally within the limits of the experimental accuracy.

Therefore it can be stated that aerodynamic parameters acquired for single-blade cases can be used to predict the aerodynamic stability of individual cluster-blades, and thus of the whole cluster, this experimentally and thus also numerically. Furthermore, this validated procedure now serves as a basis for numerical simulations, which are using a similar approach to perform parameter studies for cluster configurations under similar flow conditions.

### 8.2 Recommendations for Future Work

For future investigations, the following points could extend the accuracy of the results and enhance their interpretation:

- A simplification of the blade vibration system and cascade assembly could minimize the time necessary to change the blade oscillation direction, thus enabling the investigation of an increased number of oscillation directions.
- Introducing a coupled oscillation direction, as for example bending and torsion combined in one vibration system. The benefit would be an increased similarity to the real motion of a four-blade cluster oscillating in the first torsion mode-shape, although additional validation procedures might be necessary in order to ensure the foreseen oscillation pattern of the cluster, respectively of the individual cluster-blades.
- An increase of the blade vibration amplitudes could be achieved by tuning the cascade. This would result in higher unsteady pressure signals in regions along the blade surface with low signal strength, as observed on the second half of the suction-side. But it should be noted that achieving controlled vibrations for all necessary traveling-wave patterns will become more difficult.
- Further analysis of the applicability-boundaries of the superposition principle as to predict the aerodynamic parameters of the cluster-blades. The following possibilities could be considered:
  - Combine cluster measurements with forced response (i.e. wakes, shocks from upstream blade rows) in order to identify any influence on the aerodynamic stability of the blade.
  - Introduce a vibration pattern mistuning on the blade-row by defining clusters with an arbitrary number of blades per cluster.
  - Consider supersonic flow conditions in order to identify the influence of shocks.
  - Consider a large variation of the inflow angle in order to identify the influence of flow separation. Furthermore, consider in combination supersonic flow conditions.
  - Consider a variation of the reduced frequency parameters in order to identify the influence of the blade vibration frequency and flow velocity.
- Use of a blade-row with a different blade staggering in order to enable the simulation of more combinations of blades clustered together. Furthermore, additional vibration patterns of the blade-row could be investigated. For example a cascade with 24 blades would allow the following combinations of cluster-blades in a cluster: 2, 3, 4 and 6 (instead of 2 and 4 with a blade-row of 20 blades).

# Bibliography

**Armstrong, E.K.**, 1967:

“Recent Blade Vibration Techniques”, *ASME Journal of Engineering for Power*, Vol. 89(3), pp. 437 to 444

**Bendant, J.S.; Piersol, A.G.**, 2009:

“Random Data Analysis and Measurement Procedures”, in *John Wiley & Sons Inc.*, 4<sup>th</sup> edition, USA, ISBN 978-0-470-24877-5

**Bendiksen, O.O.; Friedmann, P.P.**, 1982:

“The Effect of Bending-Torsion Coupling on Fan and Compressor Blade Flutter”, in *ASME Journal of Engineering and Power*, Vol. 104, pp. 614 to 623

**Beretta, A.**, 2006:

“Influence of Mechanical Mistuning on the Forced Response of a Turbine Cascade”, *Thèse EPFL No. 41*, Switzerland

**Bölcs, A.**, 1983:

“A Test Facility for the Investigation of Steady and Unsteady Transonic Flows in Annular Cascades”, in *Proceedings of ASME*, 83-GT-34

**Bölcs, A.; Fransson, T.H.**, 1986:

“Aeroelasticity in Turbomachines – Comparison of Theoretical and Experimental Cascade Results”, in *tech. rep. 13*, École Polytechnique Fédérale de Lausanne – Laboratoire de Thermique Appliquée et de Turbomachines, Switzerland

**Bölcs, A.; Fransson, T.H.; Schläfli, D.**, 1989:

“Aerodynamic Superposition Principle in Vibrating Turbine Cascade”, in *Proceedings of AGARD Conference No. 468, Unsteady Phenomena in Turbomachines*, AGARD-CP-468, pp. 5-1 to 5-20

**Capone, C.**, 2000:

“Programme et Coefficients D’étalonnage pour Sondes Aérodynamiques à 5 Trous”, *Internal Report*, LTT-2000-06, Switzerland

## Bibliography

---

**Capone, C.**, 2001:

“Modification du Programme de Dépouillement pour Sondes Aérodynamiques à 5 Trous”, *Internal Report*, LTT-2001-01, Switzerland

**Carta, F.O.**, 1967:

“Coupled Blade-Disk-Shroud Flutter Instabilities in Turbojet Engine Rotors”, *Journal of Engineering for Power*, Vol. 89(3), pp. 419 to 426

**Chernysheva, O.**, 2004: “Flutter in sectorized turbine vanes” in *Doctoral Thesis*, ISBN 91-7283-716-0, Sweden

**Collar, A.R.**, 1946:

“The Expanding Domain of Aeroelasticity”, in *Journal Royal Aeronautical Society Vol. L*, pp. 613 to 636

**Corral, R.; Gallardo, J.M.; Vasco, C.**, 2004:

“Linear Stability of LPT Rotor Packets - Part II: Three Dimensional Results and Mistuning Effects”, in *Proceedings of ASME*, GT2004-54120, Austria

**Corral, R.; Gallardo, J.M.; Vasco, C.**, 2007:

“Aeroelastic Stability of Welded-in-Pair Low Pressure Turbine Rotor Blades: A Comparative Study using Linear Methods”, in *Trans. ASME Journal of Turbomachinery*, Vol. 129, pp. 72 to 83

**Corral, R.; Gallardo, J.M.; Vasco, C.**, 2009:

“A Conceptual Flutter Analysis of a Packet of Vanes using a Mass-Spring Model”, in *Trans. ASME Journal of Turbomachinery*, Vol. 131, pp. 021016-1 to 021016-7

**Crawley, E.F.**, 1988:

“Aeroelastic Formulation for Tuned and Mistuned Rotors”, in *Platzer, M.F., Carta, F.O., (eds.): AGARD Manual on Aeroelasticity in Axial-Flow Turbomachines Vol. 2, Structural Dynamics and Aeroelasticity*, AGARD-AG-298, pp. 19-1 to 19-24

**Ewins, D.J.**, 1988:

“Basic Structural Dynamics”, in *Platzer, M.F., Carta, F.O., (eds.): AGARD Manual on Aeroelasticity in Axial-Flow Turbomachines, Vol. 2, Structural Dynamics and Aeroelasticity*, AGARD-AG-298, pp. 13-1 to 13-14

**Ewins, D.J.**, 1988:

“Structural Dynamic Characteristics of Individual Blades”, in *Platzer, M.F., Carta, F.O., (eds.): AGARD Manual on Aeroelasticity in Axial-Flow Turbomachines, Vol. 2, Structural Dynamics and Aeroelasticity*, AGARD-AG-298, pp. 14-1 to 14-27

**Ewins, D.J.**, 1988:

“Structural Dynamic Characteristics of Bladed Assemblies”, in *Platzer, M.F., Carta, F.O., (eds.): AGARD Manual on Aeroelasticity in Axial-Flow Turbomachines, Vol. 2, Structural Dynamics and Aeroelasticity*, AGARD-AG-298, pp. 15-1 to 15-37



**Försching, H.**, 1994:

“Aeroelastic Stability of Cascades in Turbomachinery”, in *Progress in Aerospace Sciences*, Vol.30, pp. 213 to 216

**Grieb, H.**, 2009:

“Verdichter für Turbo-Flugtriebwerke”, in *Springer Verlag*, ISBN 978-3-540-34373-8

**Hanamura, Y.; Tanaka, H.; Yamaguchi, K.**, 1980:

“A Simplified Method to Measure Unsteady Forces Acting on the Vibrating Blades in Cascade”, in *Bulletin of the JSME (The Japan Society of Mechanical Engineers)* Vol. 23, No. 180, pp. 880 to 887

**Kahl, G.**, 1995:

“Applicaton of the Time Linerized Euler Method to Flutter and Forced Response Calculations”, in *Proceedings of the ASME Gas Turbine and Aeroengine Congress and Exposition*, 95-GT-123, USA

**Kahl, G.**, 2002:

“Aeroelastic Effects of Mistuning and Coupling in Turbomachinery Bladings”, *Thèse EPFL No. 2629*, Switzerland

**Körbächer, H.**, 1996:

“Experimental Investigation of the Unsteady Flow in an Oscillating Annular Compressor Cascade”, *Thèse EPFL No. 1512*, Switzerland

**Lane, E.**, 1956:

“System Mode Shapes in the Flutter of Compressor Blade Rows”, in *Journal of Aeronautical Sciences* 23, pp. 54 to 66

**Listvinskaya, L. Kh.**, 1975:

“Computing the Vibration Characteristics of a packet of Twisted Blades”, in *Problemy Prochnosti*, No. 11, pp. 7 to 12, UDC 534.11:62-253.5

**May, M.**, 2012:

“Linerazied Flutter Investigations of Mistuned Turbomachinery Blading”, *Doctoral Thesis*, ISSN 1434-8454, Germany

**Nagarajan, P.; Alwar, R.S.**, 1985:

“A Three Dimensional Approach to Blade Packet Vibrations”, in *Journal of Sound and Vibration*, Vol. 95, No. 3, pp. 295 to 303

**Nowinski, M.; Panovsky, J.**, 2000:

“Flutter Mechanisms in Low Pressure Turbine Blades”, in *ASME Journal of Engineering for Gas Turbines and Power*, Vol. 122, pp. 82 to 88

**Panovsky, J.; Kielb, R.E.**, 2000:

“A Design Method to Prevent LPT Blade Flutter”, in *Journal of Engineering for Gas Turbines and Power*, Vol. 122, pp. 89 to 98

## Bibliography

---

**Rolls Royce plc.**, 1996 / 2005:

“The Jet Engine”, 5<sup>th</sup> edition, 1996, and 6<sup>th</sup> edition, 2005, ISBN 0-902121-2-35, Great Britain

**Rottmeier, F.**, 2003:

“Experimental Investigation of a Vibrating Axial Turbine Cascade in the Presence of Upstream Generated Aerodynamic Gusts”, *Thèse EPFL No. 39*, Switzerland

**Schläfli, D.**, 1986:

“Etalonnage de la Sonde LP2.5-1: Analyse des Données D’étalonnage et Méthode de Déouille-ment”, *Internal Report*, LTT-86-04, Switzerland

**Schläfli, D.**, 1989:

“Experimentelle Untersuchung der Instationären Strömung in Oszillierenden Ringgittern”, *Thèse EPFL No. 800*, Switzerland

**Srinivasan, A.V.**, 1997:

“Flutter and Resonant Vibration Characteristics of Engine Blades”, in *Trans. ASME Journal of Engineering for Gas Turbines and Power*, Vol. 119, pp. 742 to 775

**Vega, A.; Corral, R.**, 2013:

“Physics of Vibrating Low Pressure Turbine Airfoils”, in *Proceedings of the 10<sup>th</sup> European Conference on Turbomachinery (ETC)*, edited by J. Bakman, G. Bois, O. Leonard, pp. 248 to 260, ETC10-2013-A224, Finland

**Verdon, J.M.**, 1987:

“Linearized Unsteady Aerodynamic Theory”, in *Platzer, M.F., Carta, F.O., (eds.): AGARD Manual on Aeroelasticity in Axial-Flow Turbomachines Vol. 1, Unsteady Turbomachinery Aerodynamics*, AGARD-AG-298, Vol. 1, pp. 2-1 to 2-31

**Vogt, D.M.**, 2005:

“Experimental Investigation of Three-Dimensional Mechanisms in Low-Pressure Turbine Flutter”, *Doctoral Thesis*, ISBN 91-7178-034-3, Sweden

**Website of the project FUTURE**, 2008:

URL: <http://www.future-project.eu>

**Whitehead, D.S.; Evans, D.H.**, 1992:

“Flutter of Grouped Turbine Blades”, in *Proceedings ASME Gas Turbine and Aeroengine Congress*, 92-GT-227

**Zanker, A.; Ott, P.; Calza P.**, 2013:

“Experimental Aeroelastic Investigation of Vibrating Turbine Blade Clusters”, in *Proceedings of the 10<sup>th</sup> European Conference on Turbomachinery (ETC)*, edited by J. Bakman, G. Bois, O. Leonard, pp. 210 to 221, ETC10-2013-A090, Finland

# A Appendix

## A.1 Blade Surface Isentropic Mach-Number at 25% and 90% Blade Height

Non-dimensional curvilinear location on PS	Isentropic Mach-number on PS	
	Average of all test cases	Standard deviation
s [-]	M <sub>is</sub> [-]	[%]
0.00	0.14	1.1
0.09	0.19	1.0
0.19	0.19	0.8
0.33	0.22	0.8
0.47	0.27	0.6
0.63	0.36	0.6
0.75	0.47	0.6
0.87	0.58	0.7
1.00	0.75	0.8

**Table A.1:** Blade surface isentropic Mach-number on PS at 25% blade-height.

Non-dimensional curvilinear location on SS	Isentropic Mach-number on SS	
	Average of all test cases	Standard deviation
s [-]	M <sub>is</sub> [-]	[%]
0.00	0.15	3.3
0.07	0.50	0.2
0.15	0.60	0.3
0.23	0.66	0.5
0.32	0.70	0.5
0.40	0.74	0.5
0.49	0.72	1.0
0.57	0.81	0.7
0.64	0.81	0.9
0.73	0.80	0.9
0.81	0.78	0.8
0.90	0.76	0.8

**Table A.2:** Blade surface isentropic Mach-number on SS at 25% blade-height.

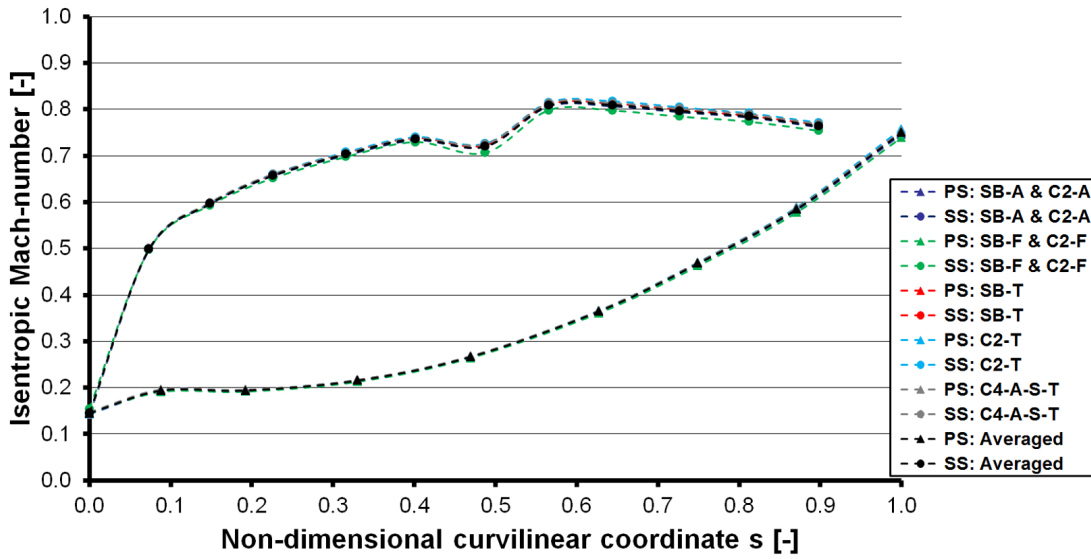


**Figure A.1:** Isentropic Mach-number distribution along the blade surface at 25% blade-height of all test cases.

Non-dimensional curvilinear location on PS s [-]	Isentropic Mach-number on PS	
	Average of all test cases M <sub>is</sub> [-]	Standard deviation [%]
0.00	0.12	4.5
0.09	0.22	6.1
0.19	0.21	6.3
0.33	0.22	5.8
0.47	0.25	3.8
0.63	0.31	1.5
0.75	0.39	0.7
0.87	0.49	0.5
1.00	0.69	0.8

**Table A.3:** Blade surface isentropic Mach-number on PS at 90% blade-height.

Non-dimensional curvilinear location on SS s [-]	Isentropic Mach-number on SS	
	Average of all test cases M <sub>is</sub> [-]	Standard deviation [%]
0.00	0.12	7.8
0.07	0.46	1.0
0.15	0.58	0.9
0.23	0.68	0.8
0.32	0.74	0.9
0.40	0.83	1.2
0.49	0.88	1.5
0.57	0.88	1.4
0.64	0.84	1.6
0.73	0.79	0.5
0.81	0.75	0.8
0.90	0.71	0.9

**Table A.4:** Blade surface isentropic Mach-number on SS at 90% blade-height.

**A.1. Blade Surface Isentropic Mach-Number at 25% and 90% Blade Height**

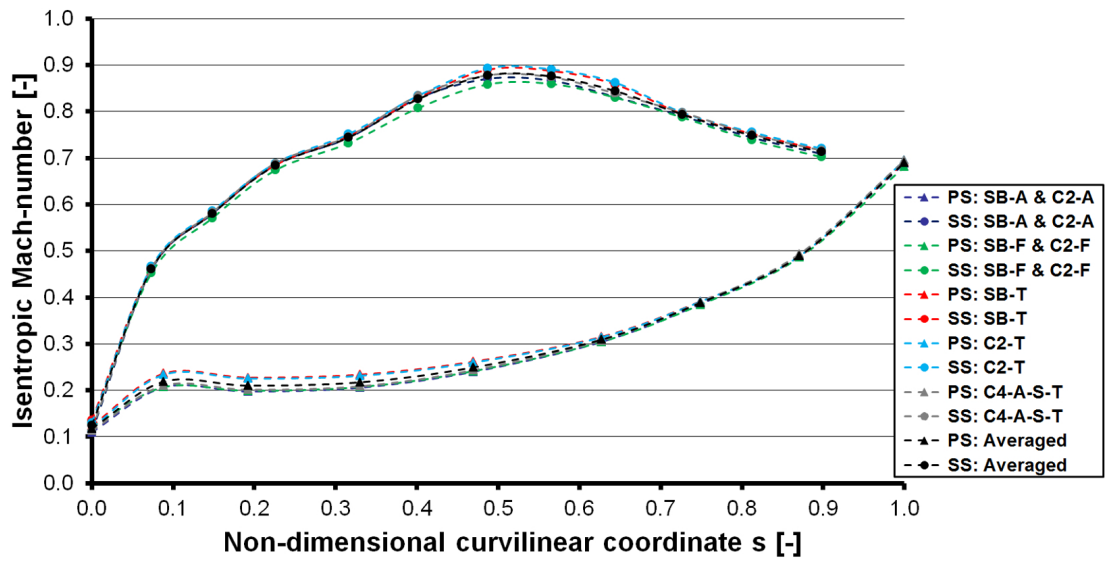


**Figure A.2:** Isentropic Mach-number distribution along the blade surface at 90% blade-height of all test cases.

## A.2 Steady-State Flow Conditions Compared to Rottmeier [2003] and Beretta [2006]

The turbine test model used for this investigation was used in previous experimental investigations performed by Rottmeier [2003] and Beretta [2006]. Rottmeier [2003] focused his work on the investigation into how upstream gusts influence the vibrational behaviour of turbine-blades. Beretta [2006] dedicated his work to investigating the influence of mechanically mistuned blade vibration systems (in mode-shape and frequency) on the forced response of turbine-blades. Certain findings of both authors are of use for this investigation. To show the applicability, this chapter documents the comparison of the steady-state flow conditions of both authors and this work. The comparison includes the measurements of the 5-hole L-shaped probes (upstream and downstream) and of the blade surface isentropic Mach-number. In Table A.5 the results of the 5-hole L-shaped probes are noted. Figure A.3 displays the blade isentropic Mach-number for the blade heights 25% (top), 50% (middle) and 90% (bottom). In Figure 5.1 on the right the locations of the 5-hole L-shaped probes relative to the blade leading-edge are documented. Beretta [2006] has measured upstream at the almost identical position, downstream measurements were 5% of the chord further downstream. In Rottmeier [2003], no information of the exact 5-hole L-shaped probe locations are documented. It is assumed the measurements of Rottmeier [2003] took place in close vicinity to those of Beretta [2006].

A comparison of the 5-hole L-shaped probe results (Table A.5) indicates almost identical Mach-numbers for inlet  $M_1$  and outlet  $M_2$  between the three test campaigns, whereas the flow angle at inlet  $\beta_1$  and outlet  $\beta_2$  varies slightly. Figure A.3 shows for all three blade heights (25%, 50% and 90%) an overall similar distribution of the blade surface isentropic Mach-number. Small changes can be identified at the stagnation point and along the first half of the pressure-side. This can be attributed to the slight variation of the inlet flow angles  $\beta_1$ . The leakage flows described in Figures 6.3 and 6.4 relate to the flow effects indicated in Figure A.3 for 25% (top) and 90% (bottom) in the mid-chord vicinity of the suction-side. For all three investigations, identical flow effects are present. Thus the considerations of Rottmeier [2003] concerning the secondary flows as well as the conclusions are applicable in this work.

## A.2. Steady-State Flow Conditions Compared to Rottmeier [2003] and Beretta [2006]

Configuration		Mach-number	Flow angle	Total pressure	Static pressure	Total temperature
		M [-]	$\beta$ [°]	$p_t$ [hPa]	$p_{stat}$ [hPa]	T [K]
Arithm. average of all test cases	US:	0.34	46.0	1343	1239	300.9
	DS:	0.69	-57.9	1302	946	-
Rottmeier [2003]	US:	0.35	46.7	1238	1139	296
	DS:	0.67	-56.9	-	890	-
Beretta [2006]	US:	0.35	46.1	1278	1174	305.7
	DS:	0.65	-57.7 <sup>a</sup>	1234	974	-

**Table A.5:** Comparison of steady-state mean flow quantities vs. Rottmeier [2003] and Beretta [2006].

<sup>a</sup> In Beretta [2006] this value is noted as -67.7°. The high discrepancy with the other two values indicated the presence of a typing error, which was confirmed by the author. This is also in agreement with the blade surface isentropic Mach-numbers (Figure A.3), since in the case of a flow angle deviation of this magnitude it would indicate a different blade surface Mach-number distribution.

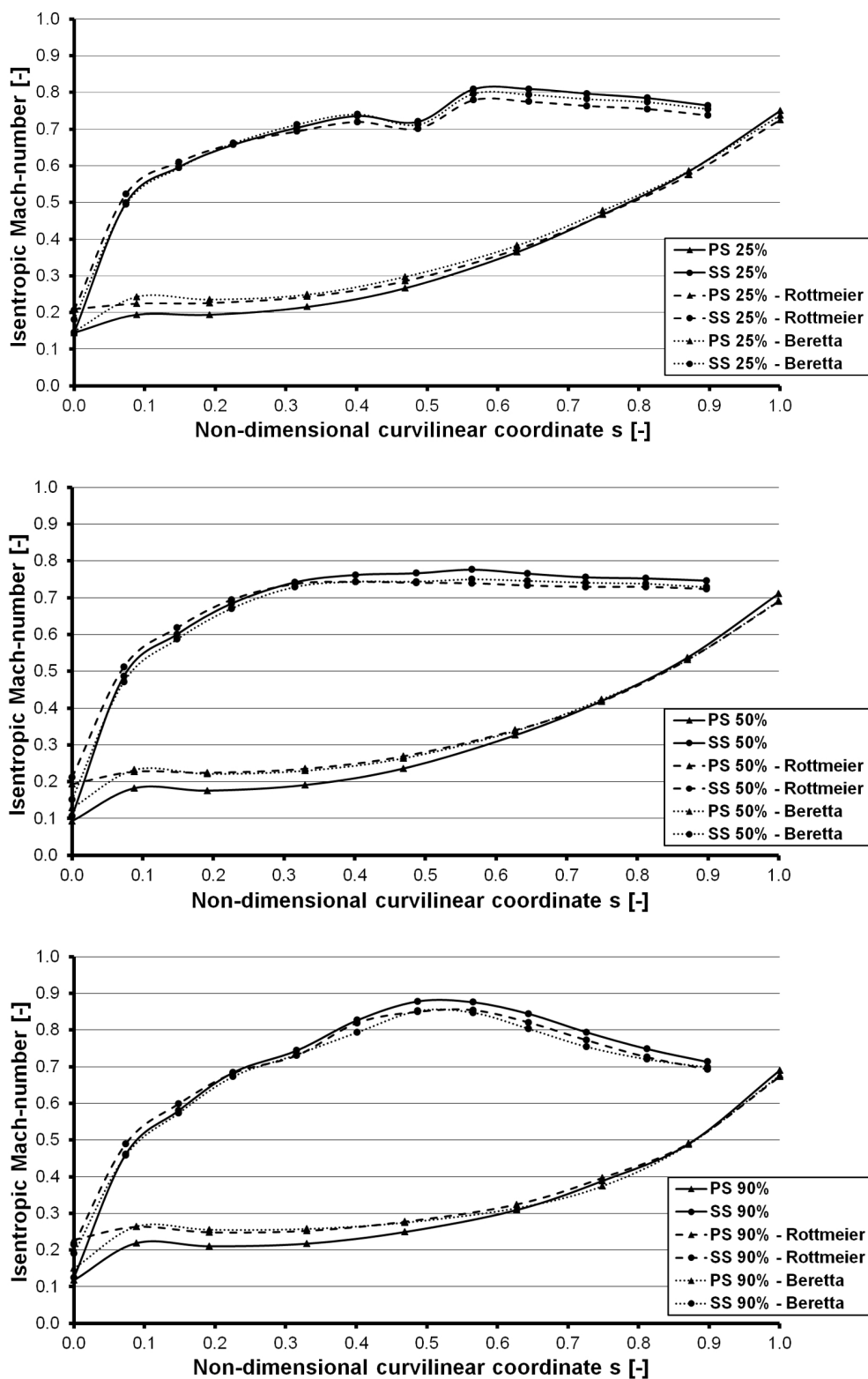


**Figure A.3:** Comparison of the isentropic Mach-number distribution along the blade surface for 25% (top), 50% (middle) and 90% (bottom) channel height to Rottmeier [2003] and Beretta [2006].



### A.3 Additional Graphs of the Single-Blade Test Case with Flap-Bending Oscillation Direction

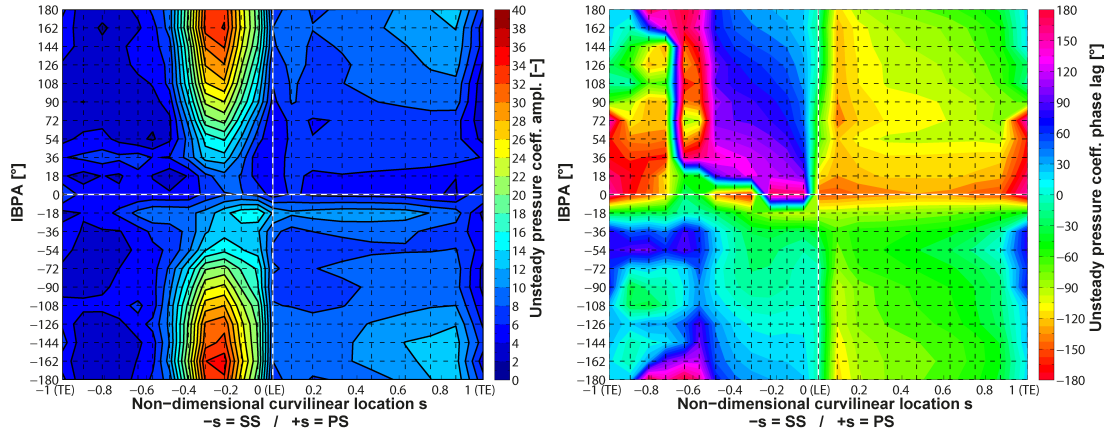


**Figure A.4:** Unsteady pressure coefficient amplitude (left) and phase lag (right) for the single-blade test case SB-F (flap-bending oscillation direction).

## A.4 Determination of the Global Aerodynamic Damping of the Four-Blade Cluster Test Case

In this section a description is given of how the global aerodynamic damping coefficient is determined for a cluster consisting of  $I_C$  blades, where each individual cluster-blade can have a different blade vibration amplitude. As a basis for the following derivation, the formulations introduced in Section 2.5 are used. The aerodynamic work performed on blade I during a period of time can be written as:

$$\Upsilon_I = \int_0^T \vec{F}_I(t) \dot{\vec{a}}_I(t) dt \quad (\text{A.1})$$

where  $\vec{F}_I(t)$  describes the aerodynamic force acting on the individual cluster-blade, as described by Equation 2.19, and  $\dot{\vec{a}}_I(t)$  the velocity of the individual cluster-blade. Thus the global aerodynamic work can be formulated as:

$$\Upsilon_I = b (p_{tI} - p_{statI}) |\hat{\vec{a}}_I| W_{FI} \quad (\text{A.2})$$

with  $W_{FI}$  describing the global aerodynamic work coefficient, as noted in Equation 2.26 for the individual cluster-blade. The global aerodynamic work of the four-blade cluster can be defined as the average of the individual cluster-blade aerodynamic work contributions and can be noted as:

$$\Upsilon_C = \frac{1}{I_C} \sum_{I=1}^{I_C} \Upsilon_I \quad (\text{A.3})$$

with  $I_C$  describing the total number of cluster-blades in a cluster. By normalizing the global aerodynamic work of Equation A.3 with the blade span width  $b$ , the difference between the total pressure  $p_{tI}$  and the static pressure  $p_{statI}$  and the blade vibration amplitude  $|\hat{\vec{a}}|$  of the cluster, it can be noted as:

$$W_C = \frac{\Upsilon_C}{b (p_{tI} - p_{statI}) |\hat{\vec{a}}|} \quad (\text{A.4})$$

By taking into account the individual cluster-blade contributions of the global aerodynamic work, as noted in Equation A.2, and substituting them in Equation A.3, Equation A.4 can be rewritten as:

$$W_C = \frac{1}{I_C} \sum_{I=1}^{I_C} \frac{|\hat{\vec{a}}_I|}{|\hat{\vec{a}}|} W_{FI} \quad (\text{A.5})$$

Equation 2.28 describes the global aerodynamic damping coefficient based on the global aerodynamic work coefficient. Thus, by using Equation A.5, the global aerodynamic damping

#### A.4. Determination of the Global Aerodynamic Damping of the Four-Blade Cluster Test Case

of the cluster can be noted as:

$$\Xi_C = -\frac{W_C}{|\hat{a}| \pi} = \frac{1}{I_C} \sum_{I=1}^{I_C} \frac{|\hat{a}_I| W_{EI}}{|\hat{a}|^2 \pi} \quad (\text{A.6})$$

It can be seen that in the case of different blade vibration amplitudes, the global aerodynamic work contribution of the individual cluster-blades are weighted by their amplitude in relation to the whole cluster movement. Thus, it can be deduced that the global aerodynamic damping coefficient for each cluster-blade related to the torsional cluster movement can be determined using:

$$\Xi_{C,I} = \frac{|\hat{a}_I| W_{EI}}{|\hat{a}|^2 \pi} \quad (\text{A.7})$$

As the theorem on intersecting lines describes (see Figure A.5), the following relation between the torsional cluster vibration amplitude and the individual cluster-blade vibration amplitude can be defined for the first two cluster-blades assuming small angles:

$$\frac{h_{ax,A}}{\frac{3L}{2}} = \frac{h_{ax,B}}{\frac{L}{2}} = \alpha_C \quad (\text{A.8})$$

with  $h_{ax,A}$  and  $h_{ax,B}$  the blade vibration amplitudes of cluster-blades A and B, and  $L$  the circumferential distance (pitch) between two neighboring blades. Due to the similarity of the cluster related to the cluster-motion, this relationship can be applied accordingly to cluster-blades C and D.

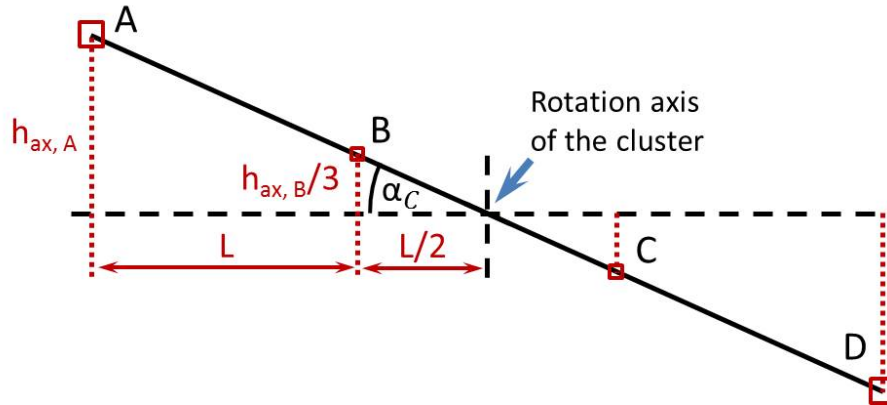


**Figure A.5:** Theorem on intersecting lines of the four-blade cluster case.

## A.5 Additional Graphs of Predicting the Aerodynamic Values of Cluster-Blades by Using Single-Blade Test Results

### A.5.1 Two-Blade-Cluster with Flap-Bending Oscillation Direction

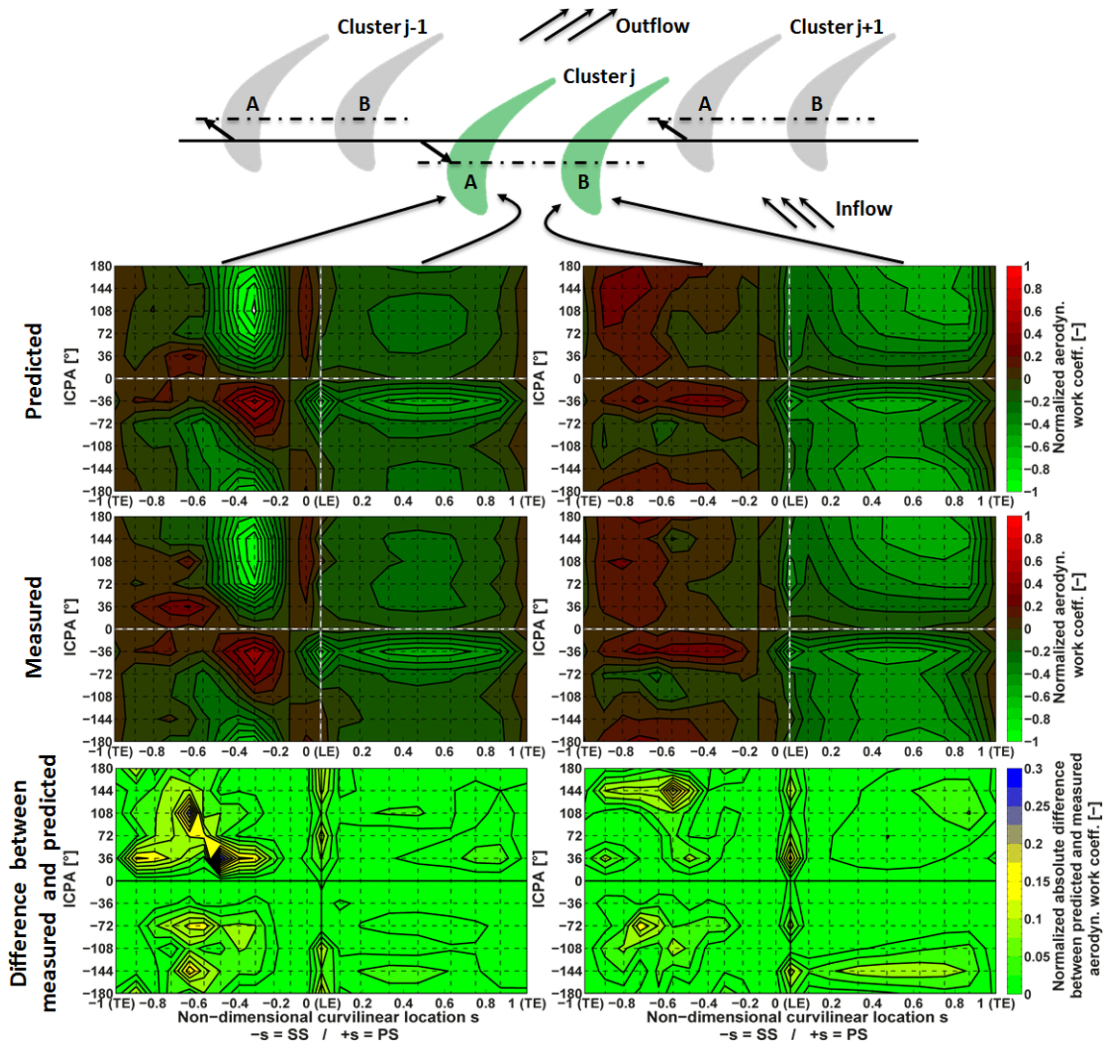


**Figure A.6:** Normalized local aerodynamic work coefficient of cluster-blades A (left) and B (right) of the two-blade cluster test case C2-F (flap-bending oscillation direction). Top: predicted results; middle: measured results; bottom: difference between predicted and measured results.

### A.5. Additional Graphs of Predicting the Aerodynamic Values of Cluster-Blades by Using Single-Blade Test Results

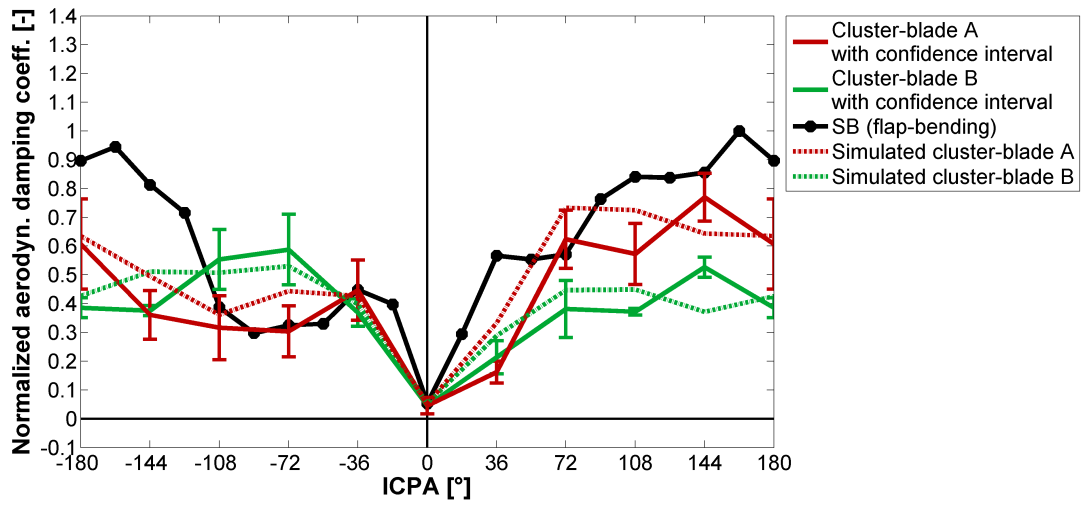
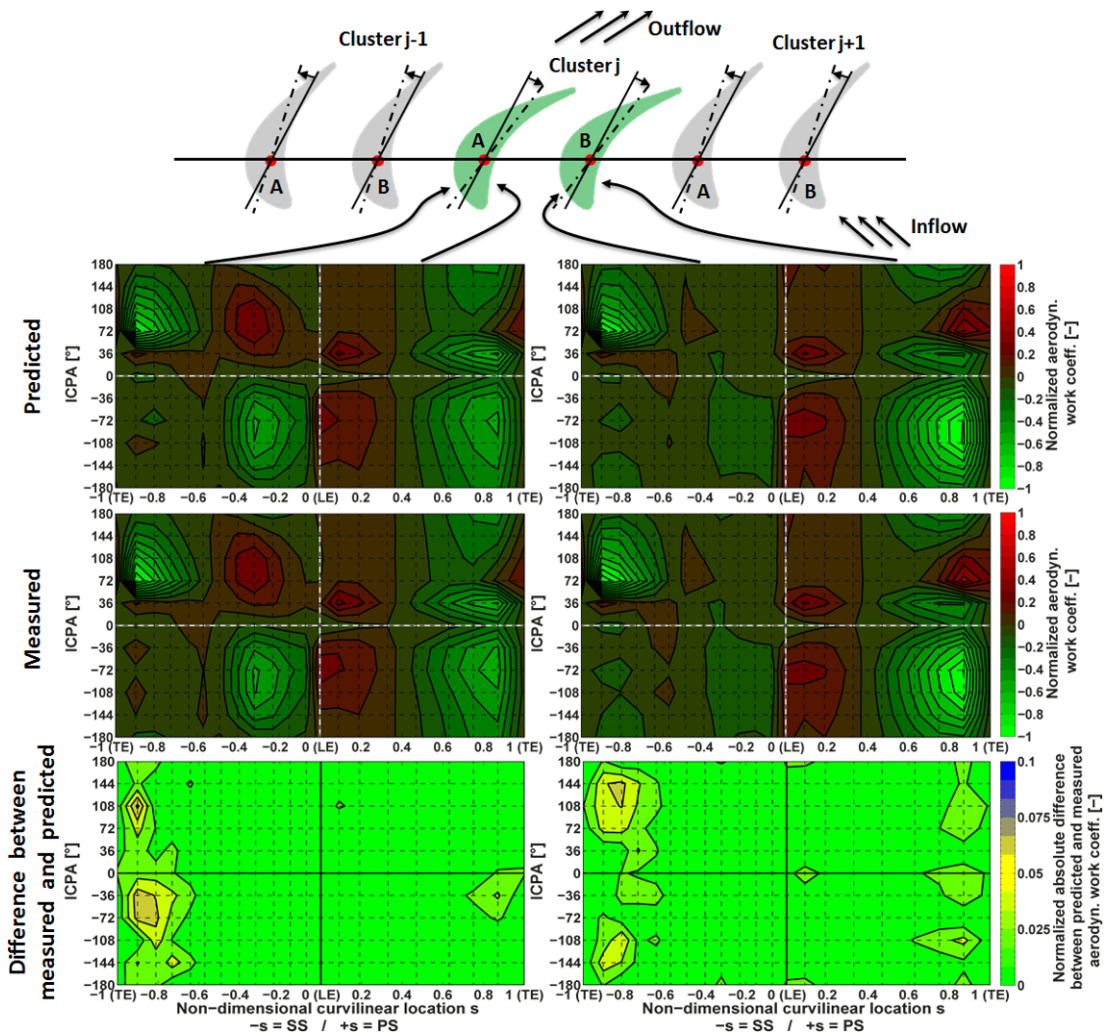


Figure A.7: Normalized global aerodynamic damping coefficient of the predicted two-blade cluster test case C2-F (flap-bending oscillation direction).

A.5.2 Two-Blade-Cluster with Torsion Oscillation Direction



**Figure A.8:** Normalized local aerodynamic work coefficient of cluster-blades A (left) and B (right) of the two-blade cluster test case C2-T (torsion oscillation direction). Top: predicted results; middle: measured results; bottom: difference between predicted and measured results.

### A.5. Additional Graphs of Predicting the Aerodynamic Values of Cluster-Blades by Using Single-Blade Test Results

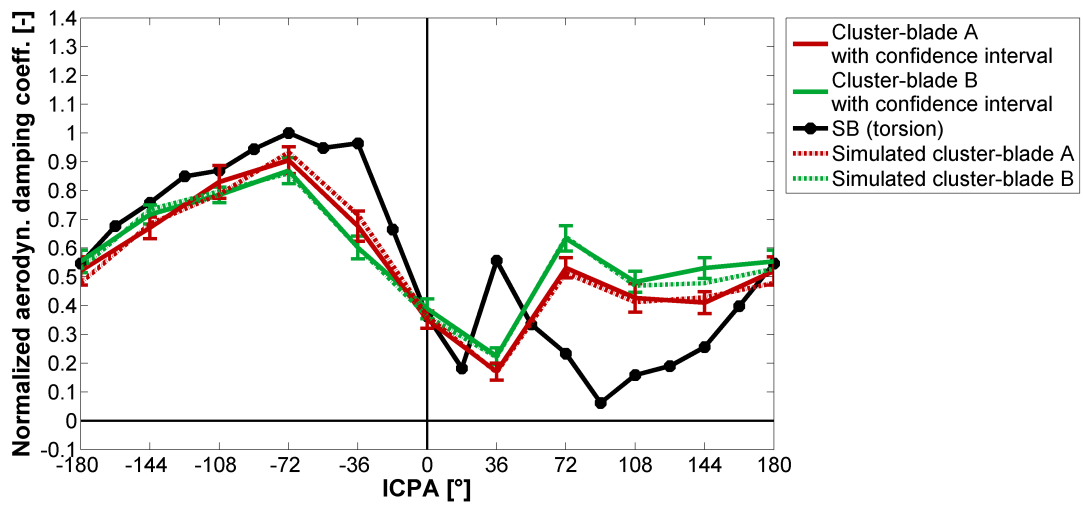


**Figure A.9:** Normalized global aerodynamic damping coefficient of the predicted two-blade cluster test case C2-T (torsion oscillation direction).

### A.5.3 Impact of the Number of Applied Influence Coefficients of the Four-Blade Cluster Test Case

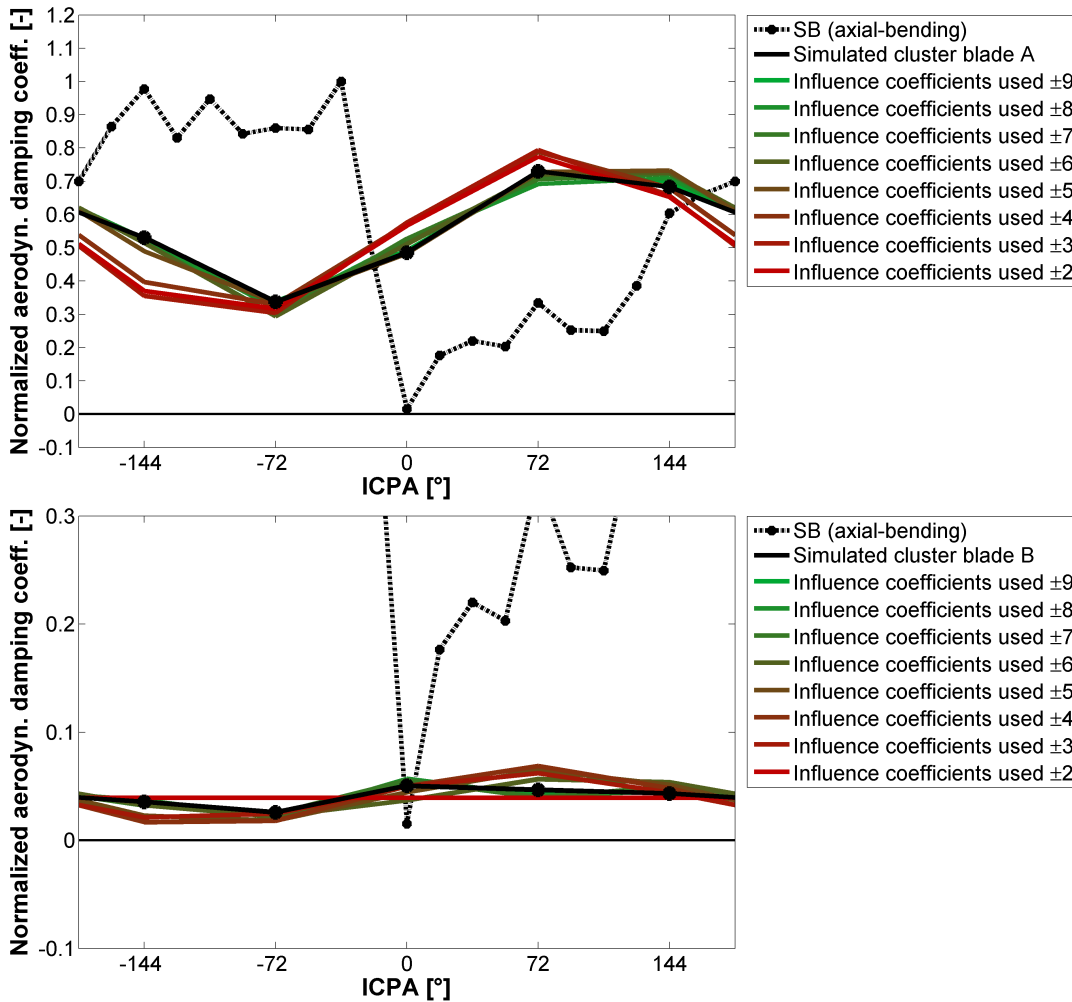


**Figure A.10:** Impact of the number of applied influence coefficients to simulate the aerodynamic damping coefficient of cluster-blades A (top) and B (bottom) of the four-blade cluster test case C4-A-S-T.



### A.5. Additional Graphs of Predicting the Aerodynamic Values of Cluster-Blades by Using Single-Blade Test Results

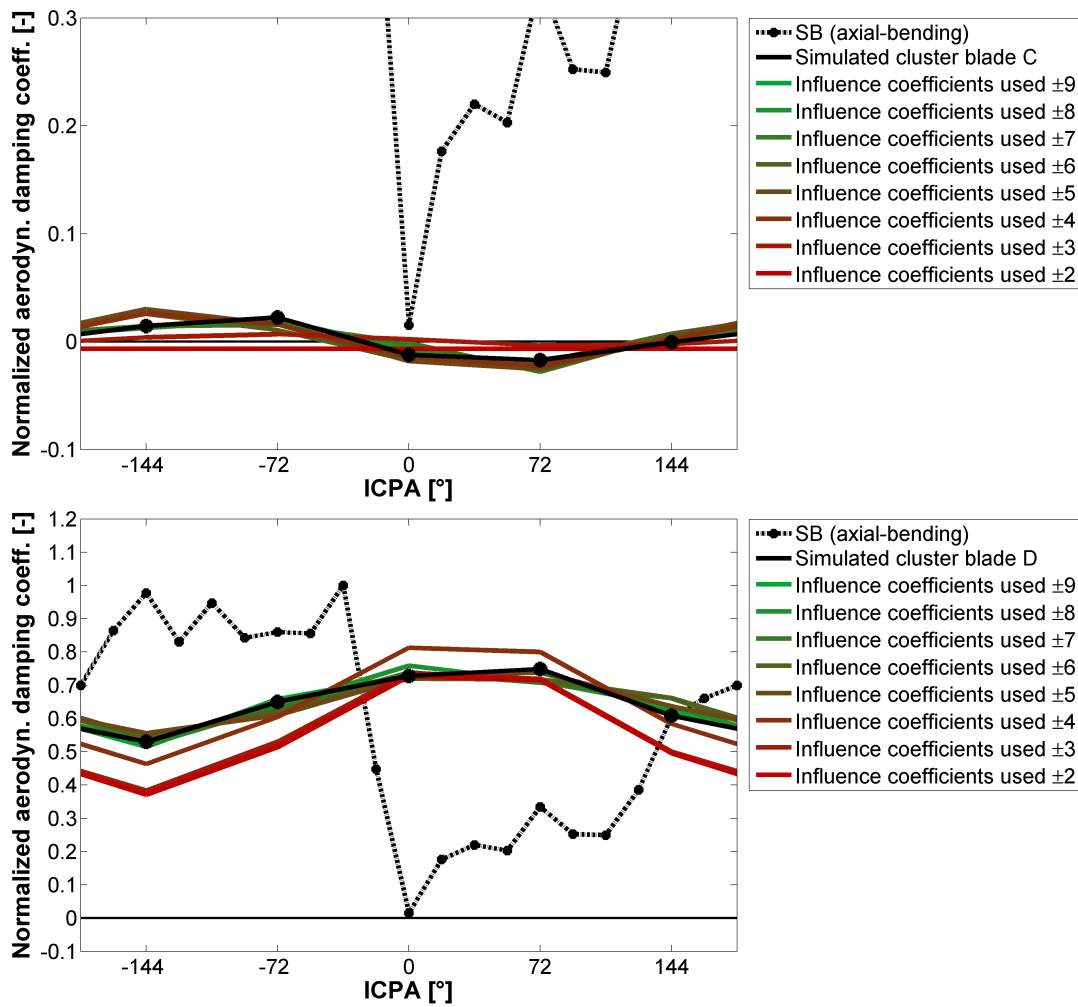


**Figure A.11:** Impact of the number of applied influence coefficients to simulate the aerodynamic damping coefficient of cluster-blades C (top) and D (bottom) of the four-blade cluster test case C4-A-S-T.



# Curriculum Vitae

Name: Achim Zanker  
Date of Birth: 12<sup>th</sup> November 1980 in Mühlacker, Germany  
Nationality: German  
E-mail: achim.zanker@a3.epfl.ch

## Education

2008 – 2014 Scientific assistant at EPFL, Lausanne, Switzerland  
Group of Thermal Turbomachinery  
2001 – 2008 Diploma in Aerospace Engineering  
University of Stuttgart, Stuttgart, Germany  
1997 – 2000 Abitur (German general qualification for university entrance)  
Heinrich-Wieland-Schule, Pforzheim, Germany

## Work Experience

2008 – 2014 EPFL, Lausanne, Switzerland, Group of Thermal Turbomachinery  
Project engineer  
Research activities: FUTURE EU-Project, in collaboration  
with European industrial and academical partners  
Students assistance

## Civil Service

2000 – 2001 German Red Cross, Pforzheim, Germany